

PROCEEDINGS

10TH INTERNATIONAL CONFERENCE ON COMMUNICATIONS, ELECTROMAGNETICS AND MEDICAL APPLICATIONS (CEMA'15)

Organized by:



FACULTY OF TELECOMMUNICATIONS
TECHNICAL UNIVERSITY OF SOFIA, BULGARIA



NATIONAL TECHNICAL UNIVERSITY OF ATHENS, GREECE,
SCHOOL OF ELECTRICAL AND COMPUTER ENGINEERING

NATIONAL TECHNICAL
UNIVERSITY OF ATHENS,
GREECE



SCHOOL OF ELECTRICAL
AND COMPUTER
ENGINEERING

Sofia, Bulgaria
15th – 17th October, 2015

KING

Edited by Prof. Dr. Eng. **Dimiter Tz. Dimitrov**

All rights reserved. This book, or parts there of, may not be reproduced in any form or by any means, electronic or mechanical, including photocopying or any information storage and the retrieval system now known or to be invented without written permission from the Publisher.

ISSN: 1314-2100

Printed in Bulgaria
KING 2001, Sofia



D. Dimitrov

Dear Colleagues,

It's my privilege to thanks to all of you for your contributions submitted at 10th regular International Conference on 'Communication, Electromagnetic and Medical Applications' CEMA'15. This is one conference which should help future collaboration between engineering, especially communication technologies and medicine. This is an important scientific event not only in Balkan region, but in Europe, also. The International Conference on Communication, Electromagnetism and Medical Application CEMA'15 is dedicated to all essential aspects of the development of global information and communication technologies and their impact for medicine. The objective of Conference is to bring together lecturers, researchers and practitioners from different countries, working on the field of communication, electromagnetism and medical applications, computer simulation of electromagnetic field, in order to exchange information and bring new contribution to this important field of engineering design and application in medicine. The Conference will bring you the latest ideas and development of the tools for the above mentioned scientific areas directly from their inventors. The objective of the Conference is also to bring together the academic community, researchers and practitioners working in the field of Communication, Electromagnetic and Medical Applications, not only from all over Europe, but also from America and Asia, in order to exchange information and present new scientific and technical contributions. Many well known scientists took part in conference preparation as members of International Scientific Committee or/and as reviewers of submitted paper. I would like to thanks to all of them for their efforts, for their suggestions and advices.

On behalf of the International Scientific Committee, I would like to wish you successful presentations of your papers, successful discussions and new collaborations for your future scientific investigations. Engineering and medicine should provide high level of live for all people.

Dimiter Tz. Dimitrov
Conference Chairman

INTERNATIONAL SCIENTIFIC COMMITTEE

Chairman:

Prof. D. TZ. DIMITROV, Technical University of Sofia, Bulgaria

Vice Chairman:

Prof. P. FRANGOS, National Technical University of Athens, Greece

Members:

Prof. N. AMPILOVA,	University of Perersburg, Russia
Prof. A. BEKJARSKY,	Technical University of Sofia, Bulgaria
Prof. B. DEKERIS,	Kaunas University of Technology, Lithuania
Prof. V. DEMIREV,	Technical University of Sofia, Bulgaria
Prof. N. DIB,	Jordan University of Science and Technology, Jordan
Prof. K. DIMITROV,	Technical University of Sofia, Bulgaria
Prof. M. DONTSCHEWA,	University of Applied Sciences, Dornbirn, Austria
Prof. V. DUMBRAVA,	Kaunas University of Technology, Lithuania
Prof. D. EIDUKAS,	Kaunas University of Technology, Lithuania
Prof. N. ESCUDEIRO,	ISEP, Porto, Portugal
Prof. E. GAGO-RIBAS,	University of Oviedo, Spain
Prof. G. GOUSSETIS,	Heriot - Watt University, United Kingdom
Prof. A. GRIGORIEV,	St. Petersburg University, Russia
Prof. S. Ver HOEYE,	University of Oviedo, Spain
Prof. M. HOFMANN,	University of Ulm, Germany
Prof. I. ILIEV,	Technical University of Sofia, Bulgaria
Prof. L. JORDANOVA,	Technical University of Sofia, Bulgaria
Prof. R. KRIVICKAS,	Kaunas University of Technology, Lithuania
Prof. V. KUKENSKA,	Technical University of Gabrovo, Bulgaria
Prof. G. MALLET,	University "Sophia Antipolis", Nice, France
Prof. G. MATSOPOULOS,	National Technical University of Athens, Greece
Prof. V. MARINKEV,	Medical University of Plovdiv, Bulgaria
Prof. M. MARTINS,	Instituto Superior Técnico, Lisboa, Portugal
Prof. M. MORALES-GONZALES,	University of Valladolid, Spain
Prof. K. NIKITA,	National Technical University of Athens, Greece
Prof. M. NIKOLOVA,	High Naval School, Varna, Bulgaria
Prof. J. PETROVSKA,	Medical University of Sofia, Bulgaria
Prof. F. PRATO,	University of Western Ontario, Canada
Prof. H. ROTH,	University of Siegen, Germany
Prof. S. SAUTBEKOV,	Euroasian University, Astana, Kazakhstan
Prof. A. SAVOV,	Medical University of Sofia, Bulgaria
Prof. S. SAVOV,	Technical University of Varna, Bulgaria
Prof. H-P. SCHADE,	Technical University of Ilmenau, Germany
Prof. L. SONG,	Technical University of Harbin, China
Prof. A. USHEVA,	University of Boston, USA

REVIEWERS

Q. BALZANO,	University of Maryland, USA
H. BERG,	Technical University of Jena, Germany
E. BOEMO,	Technical University of Madrid, Spain
M. DONTSCHEWA,	University of Applied Sciences, Dornbirn, Austria
D. DIMITROV,	Technical University of Sofia, Bulgaria
M. HOFMANN,	University of Ulm, Germany
F. KLETT,	Franhofer Institute, Ilmenau, Germany
G. MALLET,	University "Sophia Antipolis", Nice, France
M. MARINKEV,	Medical University of Plovdiv, Bulgaria
M. MARTINS,	Instituto Superior Técnico, Lisboa, Portugal
M. MORALES-GONZALES,	University of Valladolid, Spain
J. PETROVSKA,	Medical University of Sofia, Bulgaria
H. ROTH,	University of Siegen, Germany
A. SAVOV,	Medical University of Sofia, Bulgaria
H-P. SCHADE,	Technical University of Ilmenau, Germany
L. SONG,	Technical University of Harbin, China
A. USHEVA,	University of Boston, USA

Sponsors:

INTRACOM - Bulgaria
ТЕК ЕКСПЕРТС - ЕООД

REGISTRATION

October, 15th, 09h - 16h

Conference registration desk:

International Meeting Centre of Technical University - Sofia

CONFERENCE PROGRAM

15th October

Technical University of Sofia International Meetings Center "Helmut Boehme"

OPENING CEREMONY

09h 30 – 10h

FIRST SESSION

10h – 12h

Chairman: Prof. P. Frangos, NTUA, Athens, Greece

- 1. ANALYSIS OF METHOD FOR IMPROVING INPUT MATCHING OF SINGLE STAGE LOW NOISE AMPLIFIER BY USING NON-UNILATERAL CHARACTERISTICS OF TRANSISTORS,**
Mihail Plamenov Tonev, Faculty of Telecommunication, Technical University of Sofia, Bulgaria
- 2. ANALYSIS OF TWO-STAGE LOW NOISE AMPLIFIER WITH IMPROVED INPUT MATCHING BY USING NON-UNILATERAL CHARACTERISTICS OF TRANSISTORS,**
Mihail Plamenov Tonev, Faculty of Telecommunication, Technical University of Sofia, Bulgaria
- 3. QoS -BASED ROUTE SELECTION IN HEALTH CARE CLOUD A STEP TOWARDS AUTONOMOUS CONTROL FOR HEALTHCARE AS A SERVICE,**
Lina Narbutaitė, Tomas Adomkus, Rasa Brūzgienė, Department of Telecommunications, Faculty of Electrical and Electronics Engineering, Kaunas University of Technology, Lithuania
- 4. ON DIGITAL IMAGES SEGMENTATION BASED ON FRACTAL AND MULTIFRACTAL METHODS,**
N. Ampilova, I. Soloviev, St. Petersburg State University, Math. & Mech. Faculty, St. Petersburg, Russia
- 5. ON A VISUALIZATION OF LOW FREQUENCY MAGNETIC FIELDS BY USING PARAVIEW PACKAGE,**
B. Kudrin, V. Nikolov**, St. Petersburg State University, Math. & Mech. Faculty, St. Petersburg, Russia*, Faculty of Telecommunications, Technical University of Sofia, Bulgaria***

LUNCH

12h – 13h

SECOND SESSION

13h – 14h30

Chairman: Prof. Kalin Dimitrov, Technical University of Sofia, Bulgaria

- 1. PERSONAL DATA PROTECTION FOR MEDICAL ASSISTIVE SYSTEM USED BY MOTOR DISABLED PATIENTS BASED ON MPEG-21 SCHEMAS,**
Ivo Draganov, Ognian Bumbarov*, Darko Brodic**, Faculty of Telecommunications, Technical University of Sofia, Bulgaria*, University of Belgrade, Technical Faculty in Bor, Serbia***

2. **AN APPROACH TO ESTABLISHING MODELS FOR THE EMF EMISSION OF THE LAPTOPS BY ANN,**
Darko Brodić, Dejan Tanikić*, Milena Jevtić*, Ivo Draganov**, University of Belgrade, Technical Faculty in Bor, Serbia*, Faculty of Telecommunications, Technical University of Sofia, Bulgaria***
3. **DESPECKLING OF MEDICAL ULTRASOUND IMAGES BASED ON WAVELET DECOMPOSITION,**
Veska M. Georgieva, Stephan G. Vassilev**, Faculty of Telecommunications, Technical University of Sofia, Bulgaria*, Faculty of German Engineering Education and Industrial Management, Technical University of Sofia, Bulgaria***
4. **MODELING THE FLUID FLOW IN HUMAN INNER EAR,**
Svetlin Antonov, Faculty of Automatics, Technical University of Sofia, Bulgaria
5. **LOCATING THE AREAS OF ARISING OF NEW OUTBREAKS IN SPREADING FOREST FIRE THROUGH COMPUTER SIMULATION ALGORITHM,**
Svetlin Antonov, Faculty of Automatics, Technical University of Sofia, Bulgaria

BREAK
14h 30 – 15h

THIRD SESSION

15h – 16h 30

Chairman: Prof. Rasa Brūzgienė, *Kaunas University of Technology, Lithuania*

1. **COMPOSITE LASER SPOT USE FOR HARD TISSUE PROBLEMS TREATMENT IN THE DENTAL MEDICINE-NEW TECHNOLOGY, ANALYSIS , APPARATUS AND TEST,**
Margarita Deneva, Stanislava Rabadgiiska*, Nadejda Kaimakanova***, Valko Kazakov, Pepa Uzunova**, Marin Nenchev*, Technical University of Sofia, Plovdiv, Branch and R&D Department QOEL Laboratory*, Faculty of Stomatology – Medical University, Sofia**, Plovdiv University "Paissii Hilendarski", Plovdiv***
2. **DEMODULATOR FOR SATELLITE TV SIGNALS,**
Lyubomir Laskov, Faculty of Telecommunications, Technical University of Sofia, Bulgaria
3. **INFRARED INVESTIGATION ON THE THERMAL FIELD IN THE CASE OF INFLUENCE OF ULTRA HIGH FREQUENCY SIGNALS ON THE HUMAN BODY,**
Desislava Chocheva, Viktor Mihaylov, Kalin Dimitrov, Faculty of Telecommunications, Technical University of Sofia, Bulgaria
4. **MULTIPLE SCLEROSIS DIAGNOSTICS BASED ON SIMULTANEOUS USE OF EEG AND INFRARED THERMOGRAPHY,**
Viktor Mihaylov, Kalin Dimitrov, Faculty of Telecommunications, Technical University of Sofia, Bulgaria

16th October

Technical University of Sofia, International Meetings Center "Helmut Boehme"

FOURTH SESSION

09h – 10h30

Chairman: Prof. N. Ampilova, St. Petersburg University, St. Petersburg, Russia

1. EVALUATION OF EXPERIMENTAL RESULTS FOR DIFFERENT CENTRIFUGES AND PURPOSES FOR OPTIMIZATION,

Tsvetan Kachamachkov, V. Manoev**, Faculty of Mechanical engineering, Technical University of Sofia, Bulgaria*, Faculty of Electronics, Technical University of Sofia, Bulgaria***

2. MATHEMATICAL ANALYSIS OF HOW SPINNING UNDER AN ANGLE AFFECTS THE VESTIBULAR SYSTEM OF PILOTS,

Tsvetan Kachamachkov, Faculty of Mechanical engineering, Technical University of Sofia, Bulgaria

3. EXPERIMENTAL STUDY OF EXISTING CENTROFUGES IN REAL HOSPITAL CONDITIONS,

Tsvetan Kachamachkov, V. Manoev**, D.Dimitrov***, Faculty of Mechanical engineering, Technical University of Sofia, Bulgaria*, Faculty of Electronics, Technical University of Sofia, Bulgaria**, Faculty of Telecommunication, , Technical University of Sofia, Bulgaria****

4. IMPLEMENTATION FOR MEMS IN THE VESTIBULAR SYSTEM,

V. Manoev, Tsvetan Kachamachkov**, Faculty of Electronics, Technical University of Sofia, Bulgaria*, Faculty of Mechanical engineering, Technical University of Sofia, Bulgaria***

5. NEW RESEARCH FOR MEMS IN THE VESTIBULAR SYSTEM AND BASIC OVERVIEW OF MEMS USED TILL NOW,

V. Manoev, Tsvetan Kachamachkov**, Faculty of Electronics, Technical University of Sofia, Bulgaria*, Faculty of Mechanical engineering, Technical University of Sofia, Bulgaria***

6. CLINICAL RESULTS IN THE TREATMENT OF PATIENTS WITH DIABETIC POLY-NEUROPATHY WITH SIMULTANEOUS APPLICATION OF LOW-FREQUENCY MAGNETIC FIELD AND MINERAL WATER,

Vladimir Petrov, Dimitar Dimitrov**, Specialized Hospital for Rehabilitation "St. Mina", Varshets, Bulgaria*, Faculty of telecommunication, Technical University of Sofia, Bulgaria***

BREAK

10h30 – 11h

FIFTH SESSION

11h – 12h30

Chairman: Prof. Dimitar Dimitrov, Technical University of Sofia, Bulgaria

1. 3D MODEL OF PLATFORM FOR SPINNING PILOTS UNDER AN ANGLE AND OTHER MEDICAL USES,

Tsvetan Kachamachkov, Faculty of Mechanical engineering, Technical University of Sofia, Bulgaria

2. **FUNDAMENTAL STUDY ON MEASUREMENT OF DIELECTRIC CONSTANTS OF HUMAN ABDOMENBY WAVEGUIDE-PENETRATION METHOD,**
Takahiro Aoyagi, Department of Human System Science, Graduate School of Decision Science and Technology, Tokyo Institute of Technology, Japan
3. **PORTABLE 3-CHANNEL REAL-TIME EMG ACQUISITION DEVICE FOR USE WITH MYOELECTRIC PROSTHESES,**
Viktor A. Nedialkov, Faculty of telecommunication, Technical University of Sofia, Bulgaria
4. **SOFTWARE FOR ANALYZING EMG SIGNALS EMG LAB,**
Viktor A. Nedialkov, Dimitar Dimitrov, Kalin Dimitrov, Faculty of telecommunication, Technical University of Sofia, Bulgaria
5. **LOWER LIMB EMG SIGNALS STUDY FROM DIFFERENT MUSCLES FOR POTENTIAL MYOELECTRIC PROSTHESES CONTROL,**
Viktor A. Nedialkov, Faculty of telecommunication, Technical University of Sofia, Bulgaria

CLOSING SESSIONS

12h30– 13h

LUNCH

13h – 14h

SOCIAL PROGRAM

Banquet

October, 15th, 19h30

Trip

October 17th

CONTACT US:

GENERAL INFORMATION AND SUBMISSION OF CONTRIBUTIONS

Prof. Dr. D. Dimitrov

Faculty of Telecommunications
Technical University of Sofia
8, Kliment Ohridsky str.
1756 Sofia, Bulgaria
Phone/Fax: ++359 2 9652278
E-mail: dcd@tu-sofia.bg

Prof. Dr. P. Frangos

National Technical University of Athens
School of Electrical and Computer Engineering
9, Iroon Polytechniou Str.,
157 73 Zografou, Athens, Greece
Phone: 00 30 210 772 3694
Fax: 00 30 210 772 2281
E-mail: pfrangos@central.ntua.gr

TABLE OF CONTENTS

1. ANALYSIS OF METHOD FOR IMPROVING INPUT MATCHING OF SINGLE STAGE LOW NOISE AMPLIFIER BY USING NON-UNILATERAL CHARACTERISTICS OF TRANSISTORS.....	1
<i>Mihail Tonev</i>	
2. ANALYSIS OF TWO-STAGE LOW NOISE AMPLIFIER WITH IMPROVED INPUT MATCHING BY USING NON-UNILATERAL CHARACTERISTICS OF TRANSISTORS.....	5
<i>Mihail Tonev</i>	
3. QoS -BASED ROUTE SELECTION IN HEALTH CARE CLOUD A STEP TOWARDS AUTONOMOUS CONTROL FOR HEALTHCARE AS A SERVICE	9
<i>Lina Narbutaitė, Tomas Adomkus, Rasa Brūzgienė</i>	
4. ON DIGITAL IMAGES SEGMENTATION BASED ON FRACTAL AND MULTIFRACTAL METHODS	14
<i>N. Ampilova, I. Soloviev</i>	
5. ON A VISUALIZATION OF LOW FREQUENCY MAGNETIC FIELDS BY USING PARAVIEW PACKAGE.....	18
<i>B. Kudrin, V. Nikolov</i>	
6. PERSONAL DATA PROTECTION FOR MEDICAL ASSISTIVE SYSTEM USED BY MOTOR DISABLED PATIENTS BASED ON MPEG-21 SCHEMAS	22
<i>Ivo Draganov, Ognian Bumbarov , Darko Brodic</i>	
7. AN APPROACH TO ESTABLISHING MODELS FOR THE EMF EMISSION OF THE LAPTOPS BY ANN.....	27
<i>Darko Brodić, Dejan Tanikić, Milena Jevtić, Ivo Draganov</i>	
8. DESPECKLING OF MEDICAL ULTRASOUND IMAGES BASED ON WAVELET DECOMPOSITION.....	31
<i>Veska M. Georgieva, Stephan G. Vassilev</i>	
9. MODELING THE FLUID FLOW IN HUMAN INNER EAR	35
<i>Svetlin Antonov</i>	
10. LOCATING THE AREAS OF ARISING OF NEW OUTBREAKS IN SPREADING FOREST FIRE THROUGH COMPUTER SIMULATION ALGORITHM.....	39
<i>Svetlin Antonov</i>	
11. COMPOSITE LASER SPOT USE FOR HARD TISSUE PROBLEMS TREATMENT IN THE DENTAL MEDICINE-NEW TECHNOLOGY, ANALYSIS , APPARATUS AND TEST	42
<i>Margarita Deneva, Stanislava Rabadgiiska, Nadejda Kaimakanova, Valko Kazakov, Pepa Uzunova, Marin Nenchev</i>	
12. DEMODULATOR FOR SATELLITE TV SIGNALS	47
<i>Lyubomir Laskov</i>	

13. INFRARED INVESTIGATION ON THE THERMAL FIELD IN THE CASE OF INFLUENCE OF ULTRA HIGH FREQUENCY SIGNALS ON THE HUMAN BODY	52
<i>Desislava Chocheva, Viktor Mihaylov, Kalin Dimitrov</i>	
14. MULTIPLE SCLEROSIS DIAGNOSTICS BASED ON SIMULTANEOUS USE OF EEG AND INFRARED THERMOGRAPHY	54
<i>Viktor Mihaylov, Kalin Dimitrov</i>	
15. EVALUATION OF EXPERIMENTAL RESULTS FOR DIFFERENT CENTRIFUGES AND PURPOSES FOR OPTIMIZATION	57
<i>Tsvetan Kachamachkov, V. Manoev</i>	
16. EXPERIMENTAL STUDY OF EXISTING CENTROFUGES IN REAL HOSPITAL CONDITIONS	61
<i>Tsvetan Kachamachkov, V. Manoev, D. Dimitrov</i>	
17. MATHEMATICAL ANALYSIS OF HOW SPINNING UNDER AN ANGLE AFFECTS THE VESTIBULAR SYSTEM OF PILOTS.....	65
<i>Tsvetan Kachamachkov</i>	
18. IMPLEMENTATION FOR MEMS IN THE VESTIBULAR SYSTEM	69
<i>V. Manoev, Tsvetan Kachamachkov</i>	
19. NEW RESEARCH FOR MEMS IN THE VESTIBULAR SYSTEM AND BASIC OVERVIEW OF MEMS USED TILL NOW	73
<i>V. Manoev, Tsvetan Kachamachkov</i>	
20. CLINICAL RESULTS IN THE TREATMENT OF PATIENTS WITH DIABETIC POLYNEUROPATHY WITH SIMULTANEOUS APPLICATION OF LOW-FREQUENCY MAGNETIC FIELD AND MINERAL WATER.....	77
<i>Vladimir Petrov, Dimitar Dimitrov</i>	
21. 3D MODEL OF PLATFORM FOR SPINNING PILOTS UNDER AN ANGLE AND OTHER MEDICAL USES	81
<i>Tsvetan Kachamachkov</i>	
22. PORTABLE 3-CHANNEL REAL-TIME EMG ACQUISITION DEVICE FOR USE WITH MYOELECTRIC PROSTHESES	85
<i>Viktor A. Nedialkov</i>	
23. SOFTWARE FOR ANALYZING EMG SIGNALS EMG LAB	91
<i>Viktor A. Nedialkov, Dimitar Dimitrov, Kalin Dimitrov</i>	
24. FUNDAMENTAL STUDY ON MEASUREMENT OF DIELECTRIC CONSTANTS OF HUMAN ABDOMENBY WAVEGUIDE-PENETRATION METHOD	95
<i>Takahiro Aoyagi</i>	
25. LOWER LIMB EMG SIGNALS STUDY FROM DIFFERENT MUSCLES FOR POTENTIAL MYOELECTRIC PROSTHESES CONTROL	99
<i>Viktor A. Nedialkov</i>	

AUTHOR INDEX

ADOMKUS, T.	9
AMPILOVA, N.....	14
ANTONOV, S.....	35, 39
AOYAGI, T.	95
BOUMBAROV, O.	22
BRODIĆ, D.	22,27
BRŪZGIENĖ, R.	9
CHOCHEVA, D.	52
DENEVA, M.	42
DIMITROV, D.	61, 77, 91
DIMITROV, K.	52, 54, 91
DRAGANOV, I.	22, 27
GEORGIEVA, V.	31
JEVTIĆ, M.	27
KACHAMACHKOV, TS.	57, 61, 65, 69, 73, 81
KAIMAKANOVA, N.	42
KAZAKOV, V.	42
KUDRIN, B.	18
LASKOV, L.	47
MANOEV, V.....	57, 61, 69, 73
MIHAYLOV, V.	52, 54
NARBUTAITĖ, L.	9
NEDIALKOV, V.	85, 91, 99
NENCHEV, M.....	42
NIKOLOV, V.	18
PETROV, V.	77
RABADGIISKA, S.....	42
SOLOVIEV, I.	14
TANIKIĆ, D.....	27
TONEV, M.	1, 5
UZUNOVA, P.	42
VASSILEV, S.....	31

ANALYSIS OF METHOD FOR IMPROVING INPUT MATCHING OF SINGLE STAGE LOW NOISE AMPLIFIER BY USING NON-UNILATERAL CHARACTERISTICS OF TRANSISTORS A DESED ENHANCED

Mihail Plamenov Tonev

Technical University of Sofia, Bulgaria
Faculty of Telecommunication, TU-Sofia, "Kl. Ohridsky" str. 8, 1000 Sofia, Bulgaria
E-mail: mihail_tonev@abv.bg

Abstract

For low noise amplifiers the most common design is input matching network to reflect in optimum reflection coefficient of transistor for obtaining the lowest possible noise figure. The optimum reflection coefficient is different from conjugate matching and this makes low noise amplifiers to have poor input matching. This problem is challenge for microwave engineers and most popular decisions are discussed in [1]. In this paper was presented also one novel method for solving this problem by using non-unilateral characteristics of transistors. It is shown practically that can be achieved simultaneously good input matching and low noise figure. For evaluating influence of such matching to all parameters of amplifier is necessary to have proper mathematical model. In following paper is presented detailed analysis of low noise amplifier with improved input matching by using non-unilateral nature of transistors.

1. INTRODUCTION

In general every microwave single stage amplifier can be presented as cascade connection of input matching network, active component and output matching network. For theoretical analysis influence of DC feeding network is neglected. Generalized block diagram of single stage amplifier with all reflection coefficients is shown in fig1. Impedances Z_1 and Z_2 present source and load impedance. In general they are equal to characteristic impedance $Z_0=50\Omega$. Parameters of designed amplifier depend on choosing reflection coefficients of input and output matching network (Γ_S and Γ_L). For low noise amplifier required reflections are:

$$(1) \quad \Gamma_S = \Gamma_{opt}$$

$$(2) \quad \Gamma_L = \overline{\Gamma_{out}}$$

Where Γ_{opt} is optimal reflection coefficient of transistor and Γ_{out} is output reflection coefficient of transistor with matched input. Transistor is presented as two port network which have specific input and output reflection coefficients. In fig.1 they are shown as Γ_{in} and Γ_{out} .

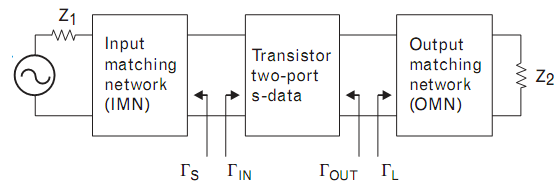


Fig. 1. Block diagram of single stage low-noise amplifier

They depend on each other but optimal reflection coefficient doesn't depend on them. This dependence is due to non-unilateral characteristics of transistors. If transistor is presented with its S-parameters, the relationship between Γ_{in} and Γ_{out} is:

$$(3) \quad \Gamma_{in} = S_{11} + \frac{S_{12}S_{21}\Gamma_L}{1 - S_{22}\Gamma_L}$$

Theoretically for obtaining simultaneous conjugate matching and noise figure matching is necessary to be satisfied equation (1) and:

$$(4) \quad \Gamma_{in} = \overline{\Gamma_{opt}}$$

The input matching network is designed in order to satisfy equation (1). The output matching network will be used for satisfaction of equation (4). This means that we neglect equation (2) and output will not be conjugate matched. In general this output mismatch will lead to loss in amplifier's insertion gain but input will be conjugate matched which makes amplifier usable in applications where this is required. In this case is necessary to make tradeoff

between input and output matching while noise figure remain constant.

2. SINGLE STAGE AMPLIFIER WITH IMPROVED INPUT MATCHING

In following chapter will be analysed single stage low noise amplifier with improved input matching. The NE3210 transistor manufactured by NEC Corporation will be used. The input and output matching networks will be designed using ideal components in order to obtain lowest possible noise figure and perfect input matching of amplifier at 12GHz. Theoretically designed amplifier will be simulated and optimized with "Ansoft Serenade" circuit simulator. The S matrix and noise parameters of transistor are given below.

$$\begin{bmatrix} S_{11} & S_{12} \\ S_{21} & S_{22} \end{bmatrix} = \begin{bmatrix} 0.44\angle-166.2^\circ & 0.10\angle2.1^\circ \\ 3.91\angle23.5^\circ & 0.21\angle-123.1^\circ \end{bmatrix}$$

$$\Gamma_{opt} = 0.29\angle133^\circ$$

$$R_n = 4.5$$

$$F_{min} = 1.08$$

The R_n and F_{min} are noise resistance and minimum noise figure. Values of these parameters are given from manufacturer.

The first step in low noise amplifier design is synthesizing input matching network. From equation (1) and transistor parameters we find required reflection coefficient. The input characteristic impedance is 50Ω . We use interactive smith chart to synthesize matching network as shown in fig. 2. This network contains two components – parallel capacitor and series inductance. Schematic diagram of transistor with synthesized noise matching network at 12GHz is shown in fig. 3. This is theoretical circuit and we use ideal components. So with this matching noise figure of transistor is equal to $F_{min} = 0.34$ dB at 12 GHz.

After transistor input is noise matched, second step in amplifier design is to match the output. In general output matching network have to satisfy equation (2) in order to obtain conjugate matching at the output and maximize insertion gain. But if we neglect this parameters and our aim is good input matching we can use equation (3) to find output reflection coefficient which will satisfy (4). From (3) and (4) we find:

$$(5) \quad \Gamma_L = \frac{S_{11} - \overline{\Gamma_{opt}}}{S_{12}S_{21} - S_{11}S_{22} + S_{22}\overline{\Gamma_{opt}}}$$

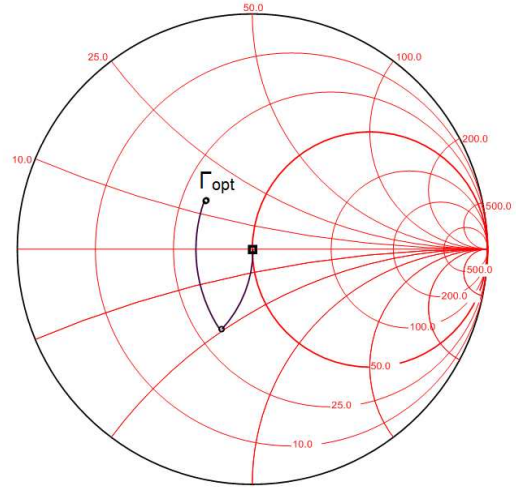


Fig. 2. Synthesizing input matching network using interactive smith chart

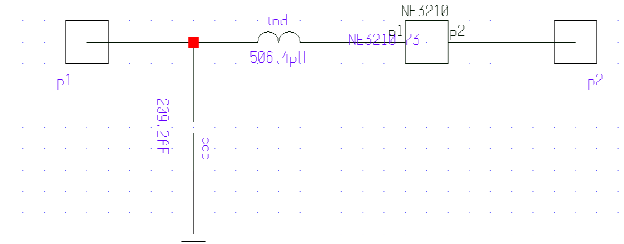


Fig. 3. Transistor connected to input noise matching network at 12GHz.

To obtain this reflection coefficient the output of transistor must be loaded with impedance:

$$(6) \quad Z_L = \frac{Z_0 - Z_0\Gamma_L}{\Gamma_L + 1}$$

From equations (5), (6) and transistor parameters given above we find required output reflection coefficient and load impedance for obtaining conjugate matched input.

$$\Gamma_L = 0.789\angle-48.89$$

$$Z_L = 104.6\angle-67.46$$

To synthesize output matching circuit is used interactive smith chart as shown in fig. 4.

Synthesized network contains two components – series inductance and parallel capacitance. Theoretically designed amplifier using ideal components is shown schematically in fig. 5.

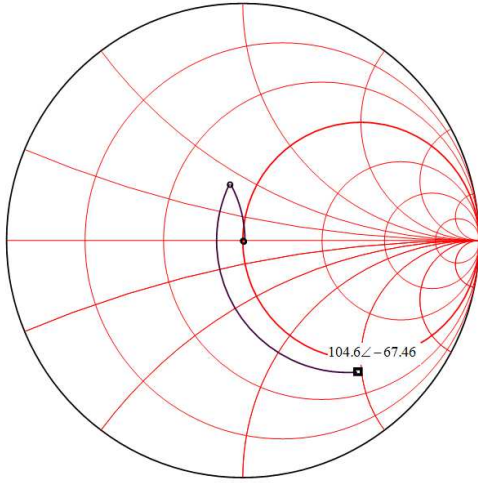


Fig. 4. Synthesizing output matching network using interactive smith chart

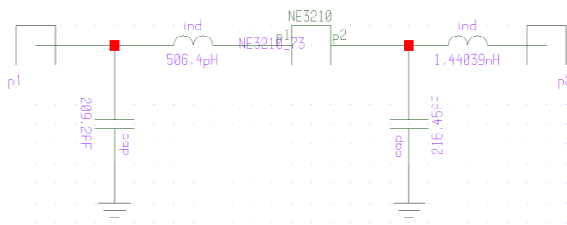


Fig. 5. Schematic diagram of single stage low noise amplifier with improved input matching

Conjugate input matching and minimum noise figure at the same time were reached but is necessary to be analysed how this type of matching is influencing to amplifier gain. The total transducer gain of amplifier can be written as:

$$(7) \quad G_T = G_S G_0 G_L$$

Where G_S is gain from source matching network, G_0 is transistor gain and G_L is gain from output network. The effective gains G_S and G_L of matching networks might be greater than unity. This is because unmatched transistor would incur power loss due to reflections at the input and output of transistor, and the matching sections can reduce this loss.

$$(8) \quad G_S = \frac{1 - |\Gamma_{opt}|^2}{|1 - \Gamma_{in} \Gamma_{opt}|^2} = 0.38 dB$$

$$(9) \quad G_0 = |S_{21}|^2 = 11.48 dB$$

$$(10) \quad G_L = \frac{1 - |\Gamma_L|^2}{|1 - S_{22} \Gamma_L|^2} = -4.62 dB$$

Using equations (7), (8), (9) and (10) is calculated transducer gain of amplifier.

$G_T = 7.6 dB$. From equation (10) is seen that 4.62 dB of amplifier's gain are lost by mismatching in output network. This is main problem in presented method for improving input matching of low noise amplifiers. Practically conjugate matched input will never be required. Parameter of amplifiers that is related to input matching is called input return loss of amplifier:

$$(11) \quad RL = 20 \log \left| \frac{VSWR - 1}{VSWR + 1} \right|, dB$$

The VSWR is voltage standing wave ratio. For most applications -20 dB return loss is sufficient. This means that input VSWR must be lower than 1.2. In fig. 6 is shown graphically area of input reflections that satisfy this requirement.

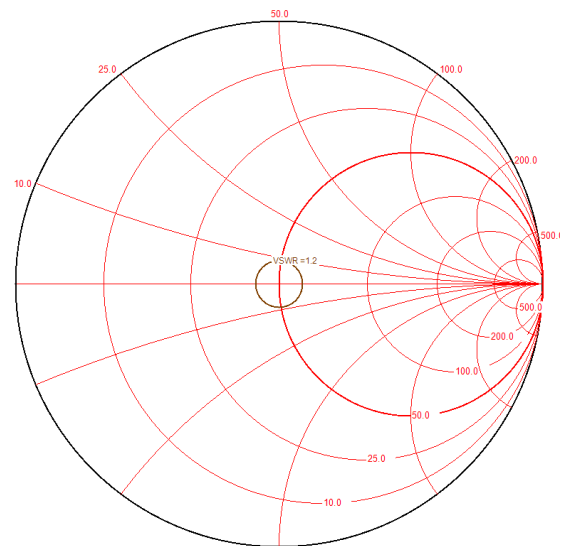


Fig. 6. Area of input reflections that satisfy practical requirements for input return loss

For amplifier's design might be chosen every input reflection coefficient inside the circle shown in fig. 6

$$(12) \quad \Gamma = \frac{Z_{opt} - \overline{Z_{in}}}{Z_{opt} + Z_{in}}$$

Z_{opt} is optimal impedance for low noise figure matching and Z_{in} is input impedance of transistor loaded with output matching network. From equation (12) we find Z_{in} and then:

$$(13) \quad \Gamma_{in} = \frac{Z_{in} - Z_0}{Z_{in} + Z_0}$$

When value for Γ_{in} is found we use (5) and (6) to find parameters of output network. With choosing proper value of Γ we can significantly reduce loss in gain due to output mismatch. Optimization procedure can be used to find the best values Z_{in} . With using linear optimization procedure in "Ansoft sere-nade" circuit simulator was found that if $Z_{in}=27-j10.1$ then loss in gain due to output mismatch will be reduced with about 3dB. Parameters of designed amplifier are: $RL=-20dB$, $G_T=10.5dB$, $NF= F_{min} = 0.35dB$.

Conclusion

A method for improving input return loss of microwave low-noise amplifiers was presented in this paper. For improving this parameter was used non-unilateral nature of transistors. A single stage low noise amplifier was analyzed and designed. The results shows that the input of amplifier can be simultaneously conjugate and noise matched but output matching will be poor and amplifier gain will be reduced. Some tradeoffs between input and output matching can be done and amplifier will meet most of the practical requirements. Further improvement of performance will be by adding second stage.

References

- [1] Mihail Tonev "Low Noise Microwave amplifiers with improved input matching applicable in active array antennas", CEMA 2014 conference, 16th – 18th October 2014, Sofia, Bulgaria, pp. 29-31
- [2] Max W. Medley "Microwave and RF circuits: Analysis, Synthesis and Design"
- [3] Pozar "Microwave Engineering 4ed"
- [4] Vendelin Rohde, Pavo "Microwave circuit design using linear and nonlinear techniques"
- [5] Guillermo Gonzalez "Microwave Transistor Amplifiers Analysis and Design"

ANALYSIS OF TWO-STAGE LOW NOISE AMPLIFIER WITH IMPROVED INPUT MATCHING BY USING NON-UNILATERAL CHARACTERISTICS OF TRANSISTORS

Mihail Plamenov Tonev

Technical University of Sofia, Bulgaria
Faculty of Telecommunication, TU-Sofia, "Kl. Ohridsky" str. 8, 1000 Sofia, Bulgaria
E-mail: mihail_tonev@abv.bg

Abstract

Improving input matching of low noise amplifiers (LNA) is general task for microwave engineers. Known methods for solving this problem and their advantages and disadvantages are discussed in [1] and [2]. In these papers is also presented one novel method which improves input matching by using non-unilateral characteristics of transistors. A detailed analysis of single stage amplifier is presented in [2]. It was shown that using this method costs loss in insertion gain of amplifier due to poor output matching. One possible decision of this problem is to add second stage of amplifier. This will be the topic of this paper. A detailed analysis and mathematical model of two stages LNA with improved input matching will be presented here. Furthermore the real S - parameters of transistor will be used to evaluate performance of theoretically designed amplifier.

1. INTRODUCTION

When single stage amplifiers cannot provide sufficient gain, we can either cascade stages already impedance matched or continuously match the output of one stage to the input of next stage until the desired gain is reached. As was shown in [2] improving input matching of single stage low noise amplifier by using non-unilateral characteristics of transistors costs poor output matching. For this reason we will try to match directly input of second stage to required output impedance of the first stage in order to obtain good input matching. Generalized block diagram with all specific impedances and reflection coefficient of two-stage amplifier which use this type of matching is shown in fig.1.

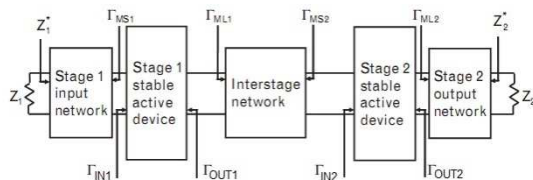


Fig. 1. Block diagram of two-stage amplifier with all specific reflection coefficients

Analyzed amplifier in this paper use transistors NE3210 manufactured by NEC corporation for both stages. Its S-matrix and noise parameters for 12 GHz are:

$$\begin{bmatrix} S_{11} & S_{12} \\ S_{21} & S_{22} \end{bmatrix} = \begin{bmatrix} 0.44\angle-166.2^\circ & 0.10\angle2.1^\circ \\ 3.91\angle23.5^\circ & 0.21\angle-123.1^\circ \end{bmatrix}$$

$$\Gamma_{opt} = 0.29\angle133^\circ$$

$$R_n = 4.5$$

$$F_{min} = 1.08$$

Where Γ_{opt} is optimal reflection coefficient, R_n and F_{min} are noise resistance and minimum noise figure. We will use designed single stage amplifier in [2] and upgrade it with second stage. In this paper was explained in details requirements for reflections at the input and the output of transistor in order to obtain low noise figure and conjugate matched input. So we will use synthesized in [2] input matching network, which is show in fig.2.

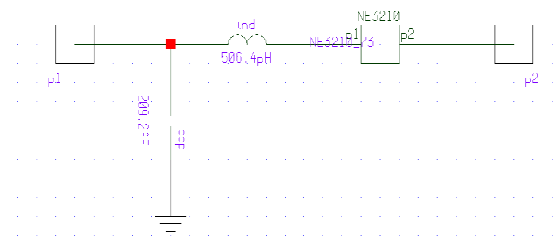


Fig. 2. Input noise matching network

The interstate and output matching circuits will be designed in order to be obtained conjugate matched input and output of amplifier and maximize insertion gain while noise figure remains unchanged.

2. ANALYSIS OF TWO-STAGE LOW NOISE AMPLIFIER WITH IMPROVED INPUT MATCHING

To analyse how this method for improving input matching influence to the other parameters of two-stage LNA is necessary the amplifier to be described mathematically. In this chapter will be presented mathematical model that find S – matrix and noise figure of this amplifier.

In general when we design multi- stage amplifier we cascade two port networks which are not conjugate matched to characteristic impedance. For analysing such circuit are used ABCD parameters of connected networks. Relationship between ABCD and S parameters is:

$$(1) \quad A = \frac{(1 + S_{11})(1 - S_{22}) + S_{12}S_{21}}{2S_{21}}$$

$$(2) \quad B = \frac{(1 + S_{11})(1 - S_{22}) - S_{12}S_{21}}{2S_{21}} Z_0$$

$$(3) \quad C = \frac{(1 - S_{11})(1 - S_{22}) - S_{12}S_{21}}{2S_{21}Z_0}$$

$$(4) \quad D = \frac{(1 - S_{11})(1 + S_{22}) + S_{12}S_{21}}{2S_{21}}$$

Using (1), (2), (3), (4) and S parameters given above we can find ABCD matrix of used transistor at 12GHz:

$$\begin{bmatrix} A & B \\ C & D \end{bmatrix} = \begin{bmatrix} 0.44 \angle -166.2^\circ & 0.10 \angle 2.1^\circ \\ 3.91 \angle 23.5^\circ & 0.21 \angle -123.1^\circ \end{bmatrix}$$

They will be used further when designed LNA is analyzed.

The mathematical model of amplifier can be obtained by multiplying ABCD matrices of active components and matching networks. From this model can be obtained reflection coefficient and insertion gain in every point of this circuit.

$$(5) \quad \begin{bmatrix} A_{LNA} & B_{LNA} \\ C_{LNA} & D_{LNA} \end{bmatrix} = \begin{bmatrix} A_1 & B_1 \\ C_1 & D_1 \end{bmatrix} \begin{bmatrix} A & B \\ C & D \end{bmatrix} \begin{bmatrix} A_2 & B_2 \\ C_2 & D_2 \end{bmatrix} \begin{bmatrix} A & B \\ C & D \end{bmatrix} \begin{bmatrix} A_3 & B_3 \\ C_3 & D_3 \end{bmatrix}$$

Where:

$$\begin{bmatrix} A_1 & B_1 \\ C_1 & D_1 \end{bmatrix} - \text{ABCD matrix of input matching circuit.}$$

$$\begin{bmatrix} A_2 & B_2 \\ C_2 & D_2 \end{bmatrix} - \text{ABCD matrix of inter - stage matching circuit.}$$

$$\begin{bmatrix} A_3 & B_3 \\ C_3 & D_3 \end{bmatrix} - \text{ABCD matrix of output matching circuit.}$$

By using S-parameters and equations (1), (2), (3), (4) we find ABCD matrix of input matching network

$$\begin{bmatrix} A_1 & B_1 \\ C_1 & D_1 \end{bmatrix} = \begin{bmatrix} 1.001 \angle -0.126^\circ & 38.189 \angle 90.149^\circ \\ 0.016 \angle 90.144^\circ & 0.397 \angle -0.318^\circ \end{bmatrix}$$

The inter-stage and output matching networks will be designed later by using interactive smith chart and linear optimization procedure in "Ansot Sere-nade circuit simulator". Their ABCD parameters will be calculated with (1), (2), (3) and (4). When we have ABCD matrix of two stages amplifier we can calculate its S – parameters with equations:

$$(6) \quad S_{11} = \frac{A + \frac{B}{Z_0} - CZ_0 - D}{A + \frac{B}{Z_0} + CZ_0 + D}$$

$$(7) \quad S_{12} = \frac{2(AD - BC)}{A + \frac{B}{Z_0} + CZ_0 + D}$$

$$(8) \quad S_{21} = \frac{2}{A + \frac{B}{Z_0} + CZ_0 + D}$$

$$(9) \quad S_{22} = \frac{-A + \frac{B}{Z_0} - CZ_0 - D}{A + \frac{B}{Z_0} + CZ_0 + D}$$

After S – parameters of amplifier are found is necessary to be analysed influence of second stage to noise figure. For this analysis is necessary to be known separately gain and noise figure of every stage. Total noise figure of amplifier can be calculated using equation:

$$(10) \quad F = F_1 + \frac{F_2 - 1}{|S_{21_A}|^2}$$

Where: F is total noise figure of two stages LNA, F_1 is noise figure of the first stage, F_2 is noise figure of second stage and S_{21_A} is gain of the first stage with input matching circuit.

The first stage is noise matched:

$$(11) \quad F_1 = F_{\min}$$

The S_{21_A} can be found using ABCD matrices and equation (8).

$$(12) \quad \begin{bmatrix} A_{-A} & B_{-A} \\ C_{-A} & D_{-A} \end{bmatrix} = \begin{bmatrix} A_1 & B_1 \\ C_1 & D_1 \end{bmatrix} \begin{bmatrix} A & B \\ C & D \end{bmatrix}$$

To finish analysis of noise figure we need to know noise figure of the second stage. It can be calculated using equation:

$$(13) \quad F = F_{\min} + \frac{4R_n |\Gamma_{MS2} - \Gamma_{opt}|^2}{Z_0 |1 + \Gamma_{opt}|^2 (1 - |\Gamma_{MS2}|^2)}$$

The Γ_{MS2} is reflection coefficient at the output of inter-stage matching circuit. We find Γ_{MS2} by multiplying ABCD matrices of input matching circuit, transistor and output matching circuit. And then use equation (6) to derive it.

$$(14) \quad \begin{bmatrix} A_{-B} & B_{-B} \\ C_{-B} & D_{-B} \end{bmatrix} = \begin{bmatrix} A_1 & B_1 \\ C_1 & D_1 \end{bmatrix} \begin{bmatrix} A & B \\ C & D \end{bmatrix} \begin{bmatrix} A_2 & B_2 \\ C_2 & D_2 \end{bmatrix}$$

3. DESIGN INTER-STAGE AND OUTPUT MATCHING CIRCUITS OF TWO STAGE LNA WITH IMPROVED INPUT MATCHING

As was explained in [2], for obtaining conjugate matched input is necessary to have a specific reflection coefficient of output matching network. In case of two stage amplifier this reflection coefficient will be obtained from interstate matching network as shown in fig.1. From [2] we take:

$$\begin{aligned} \Gamma_{ML1} &= 0.789 \angle -48.89 \\ Z_{ML1} &= 104.6 \angle -67.46 \end{aligned}$$

We need to design matching circuit which transform input impedance of transistor to required impedance Z_{ML1} . Furthermore the output matching circuit have to provide conjugate matching at the output of amplifier:

$$(15) \quad \Gamma_{ML2} = \overline{\Gamma_{OUT2}}$$

As was explained transistors do not have perfect isolation between output and input. For this reason inter-stage and output matching networks have to be designed simultaneously. This can be expressed

mathematically by solving system of equations but here will be shown simplified method for design matching networks. The full mathematical analysis of the matching circuits is not subject of this paper. First will be designed interstate matching network. We use interactive smith chart to synthesize it as shown in fig.2. This network have to transform input impedance of the second stage to required output impedance of the first stage in order to be obtained conjugate matched input of amplifier. Synthesized matching network contains parallel capacitor and series inductance.

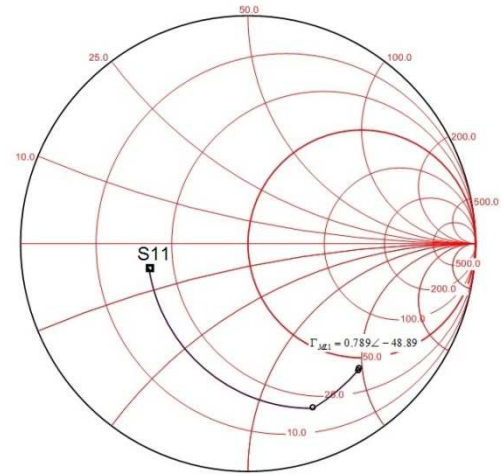


Fig. 3. Design inter - stage matching network using interactive smith chart

After inter-stage matching network is designed it will be connected to the input of transistor and Γ_{OUT2} will be calculated. The output matching network will be designed in order to satisfy equation (15). Again will be used interactive smith chart as shown in fig. 4.

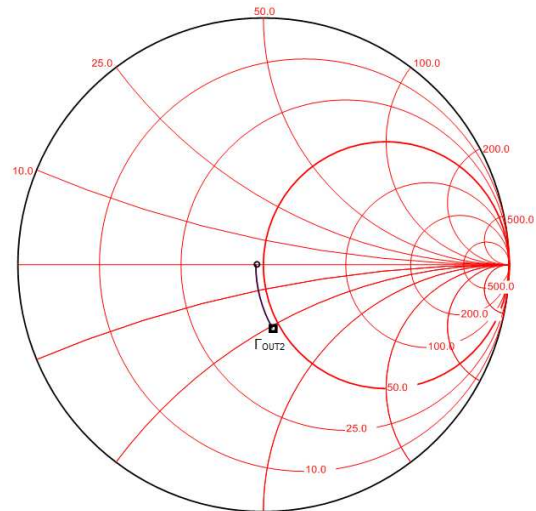


Fig. 4. Design output matching network using interactive smith chart

After that both matching networks will be connected to corresponding port of transistor. There will be some mismatch due to not perfect isolation and it will be compensated by using optimization. The ABCD parameters of optimized networks are:

$$\begin{bmatrix} A_2 & B_2 \\ C_2 & D_2 \end{bmatrix} = \begin{bmatrix} 1\angle 0^\circ & 68.54\angle -90^\circ \\ 0.005\angle -90^\circ & 0.65\angle 0^\circ \end{bmatrix}$$

$$\begin{bmatrix} A_3 & B_3 \\ C_3 & D_3 \end{bmatrix} = \begin{bmatrix} 1\angle 0^\circ & 30.16\angle 90^\circ \\ 0\angle 0^\circ & 1\angle 0^\circ \end{bmatrix}$$

When all matching networks are available, the ABCD and S parameters of two stages amplifier can be calculated using equation (5), (6), (7), (8), (9). The S-matrix of designed LNA is:

$$\begin{bmatrix} S_{11LNA} & S_{12LNA} \\ S_{21LNA} & S_{22LNA} \end{bmatrix} = \begin{bmatrix} 0.002\angle -146.7^\circ & 0.008\angle -9.5^\circ \\ 10.64\angle 33.26^\circ & 0.001\angle 48.2^\circ \end{bmatrix}$$

The noise figure can be found using equation (10). To solve it is necessary to calculate gain of the first stage with input matching network. We use equation (12) and then substitute in equation (8) and find:

$$S_{21-A} = 4.19\angle -28.96^\circ$$

The other parameter that we need to find noise figure of LNA is noise figure of second stage by itself. It can be calculated using (13) but first must be found reflection coefficient at the input of second stage. To do this we use (14) and then substitute in (6) and find:

$$\Gamma_{MS2} = 0.67\angle -62.64^\circ$$

The calculated noise figure of second stage is:

$$F_2 = 1.95$$

Now we have all parameters needed to find noise figure of designed two-stage LNA.

$$F = 1.13$$

Practically parameters of amplifiers are expressed in decibels:

$$G = 20\log|S_{21LNA}| = 20.5dB$$

$$RL_{IN} = 20\log|S_{11LNA}| = -53.8dB$$

$$RL_{OUT} = 20\log|S_{22LNA}| = -58.8dB$$

$$NF = 10\log|F| = 0.55dB$$

Where G is gain of amplifier, RL_{IN} is input return loss, RL_{OUT} is output return loss and NF is noise figure. Theoretically lowest possible noise figure will be obtained when inputs of both stages are noise matched. Then total noise figure of amplifier will be 0.36dB. So we can conclude that conjugate matched input and output of two stages LNA will increase noise figure with about 0.2dB. This will be due to contribution of second stage to total noise figure of amplifier. But as was explained in [2] conjugate matching is just theoretical. In practice will never be required amplifier to be conjugate-matched. Return loss of -20dB is often sufficient for microwave amplifiers. So some trade-offs between matching, gain and noise figure can be done in order to be satisfied practical requirements to LNA.

CONCLUSION

Theoretical analysis of two stages LNA with improved input matching by using non-unilateral characteristics of transistor was presented in this paper. The results of this analysis shows that in two stage configuration can be reached simultaneously noise matched input and conjugate matched ports of amplifier but contribution of second stage to total noise figure can be significant. Total gain of amplifier will also be reduced by this type of matching. Some tradeoffs between input matching, gain and noise figure can be done and amplifier will meet most of the practical requirements. Analysis of this trade-offs will be subject of further work.

References

- [1] Mihail Tonev "Low Noise Microwave amplifiers with improved input matching applicable in active array antennas", CEMA 2014 conference, 16th – 18th October 2014, Sofia, Bulgaria, pp. 29-31
- [2] Mihail Tonev "Analysis of method for improving input matching of single stage low noise amplifier by using non-unilateral characteristics of transistors", CEMA 2015 conference
- [3] Max W. Medley "Microwave and RF circuits: Analysis, Synthesis and Design"
- [4] Pozar "Microwave Engineering 4ed"
- [5] Vendelin Rohde, Pavio "Microwave circuit design using linear and nonlinear techniques"
- [6] Guillermo Gonzalez "Microwave Transistor Amplifiers Analysis and Design"

QoS-BASED ROUTE SELECTION IN HEALTHCARE CLOUD

A step towards autonomous control for Healthcare as a Service

Lina Narbutaitė, Tomas Adomkus, Rasa Brūzgienė

Department of Telecommunications
Faculty of Electrical and Electronics Engineering
Kaunas University of Technology
Studentu str. 50-452, Kaunas, Lithuania, LT- 51368
E-mail: rasa.bruzgiene@ktu.lt

Abstract

Today's technology-based health services transforms all Healthcare system substantially - from the provision of services in the hospital to the care of patient in the home. This transformation is a result of rapidly growing health data of patients in all health system. The fast changing face of Healthcare system comes from the integration of cloud computing and the Internet of Services with the requirements for Healthcare. This integration brings the technologically advanced solution – Health Cloud – for the issues of health data processing and managing in health system. However, the requirements for provision and deployment of medical services across a Health Cloud bring new challenges of the selection of suitable cloud service provider during the transmission of medical data over Health Cloud. The reliable, cost effective communication and Quality of Service based routing path between multi-cloud providers is a critical issue for Healthcare entities across over Health Cloud and its deployment models. Due to this, the task of this paper was to investigate the selection of route for health data transmission over Health Cloud according to the requirements of Quality of Service. The authors' proposed analytical model for health data path request and a reply to this request with the results of investigations are presented in this paper. The impact of the proposed Quality of Service based routing path to Health Cloud networking and service's provision effectiveness is presented as well.

1. INTRODUCTION

The evolution of new, technology based, medical services promotes the progress in one of the most important systems of services for humans – Healthcare. The growing number of people increases the need for technology-based health services as a doctor's consultation at a distance or the training and self-management of patient's health at home. The reason behind this is the growing health data of patients in overall Healthcare system. The increasing traffic of a health data raises the many challenges of data processing in all the system. First of all, the health data must be stored and archived for more than several years. The exact time for storing of it depends on the medical regulations of the country. That means the health entities as hospitals or wellness centers must have a strong infrastructure setup, which will be able to manage all the growing health data for many years. And this may affect the rising of investments for health entities or even pricing of health services to patients. Next, the security aspects of health data: the backup of this data have to be made constantly, the specifications for data recovery, rules of access to this data for patients, health entities have to be planned in any case of life event [1]. Very important is the issue of

the health data exchange between the Healthcare entities and its accessibility anytime, anywhere with any doctor's or patient's device for communication. Data exchange between the Healthcare entities would help to reduce a duplication of health data, patient's time of waiting for health procedures and strengthen the cooperation between the entities. However, this means a joint database for patient's health, the specific rules for such data exchange, sharing, and access to it. This is very challenging due to lack of fast and secure mechanism of data access, the issues for the interoperability between different infrastructure setup in the health entities. It also includes the sharing of health data across many different devices like smart phones, tablets, personal computers, as this will require very straight process of health data transmission over the all Healthcare system. Due to this, the cloud computing is a good solution for all of these challenges in the Healthcare system. This is an innovative technology, which can help in managing the increasing rate of digital health data. It also can play an important role in the accessibility and availability of Healthcare services in large, scalable on-demand computing infrastructures. The adoption of cloud computing can optimize costs and resources of

Healthcare services as well as achieve high performance and scalability for the Healthcare entities.

Although the cloud computing is a promising technology it brings new challenges raised from the integration of cloud computing and Internet of Services (IoS) [2] with the requirements for today's Healthcare system [3]. One of those challenges is the quality of performance of various Healthcare operations over the cloud based on Service Level Agreement (SLA) and Quality of Service (QoS) requirements. The number of medical services for performance of various Healthcare operations and service oriented architecture compose Health Cloud [4]. Health Cloud should cover the functions of IoS with the requirements for provision and deployment of dynamic medical services in a single cloud infrastructure provider as well as across different cloud infrastructure providers. Due to this, the Quality of service is a critical issue for Healthcare entities across cloud service and deployment models – private, community, hybrid or public clouds [3]. There are limitations to guarantee QoS between

deployed cloud infrastructures that are spread across distributed sites or domains. On the other hand, the user requires a QoS assurance, a high reliability and availability for his medical services over Health Cloud. It is very difficult for a single cloud service provider to satisfy this. In addition, if a Health Cloud is distributed over different cloud service providers, it should be designed as inter-cloud system with the ability to displace the medical services from one cloud service provider to another, to find the best ways for location of best resources as computing capacity, storage, connectivity, bandwidth and delay [5]. Furthermore, the networking aspect of cloud computing plays an important role for this as there is many challenges on how to choose suitable cloud service provider during the transmission of medical data over Health Cloud. The establishment of the reliable communication and routing path between multiple clouds over Health Cloud is based on traffic engineering with QoS requirements.

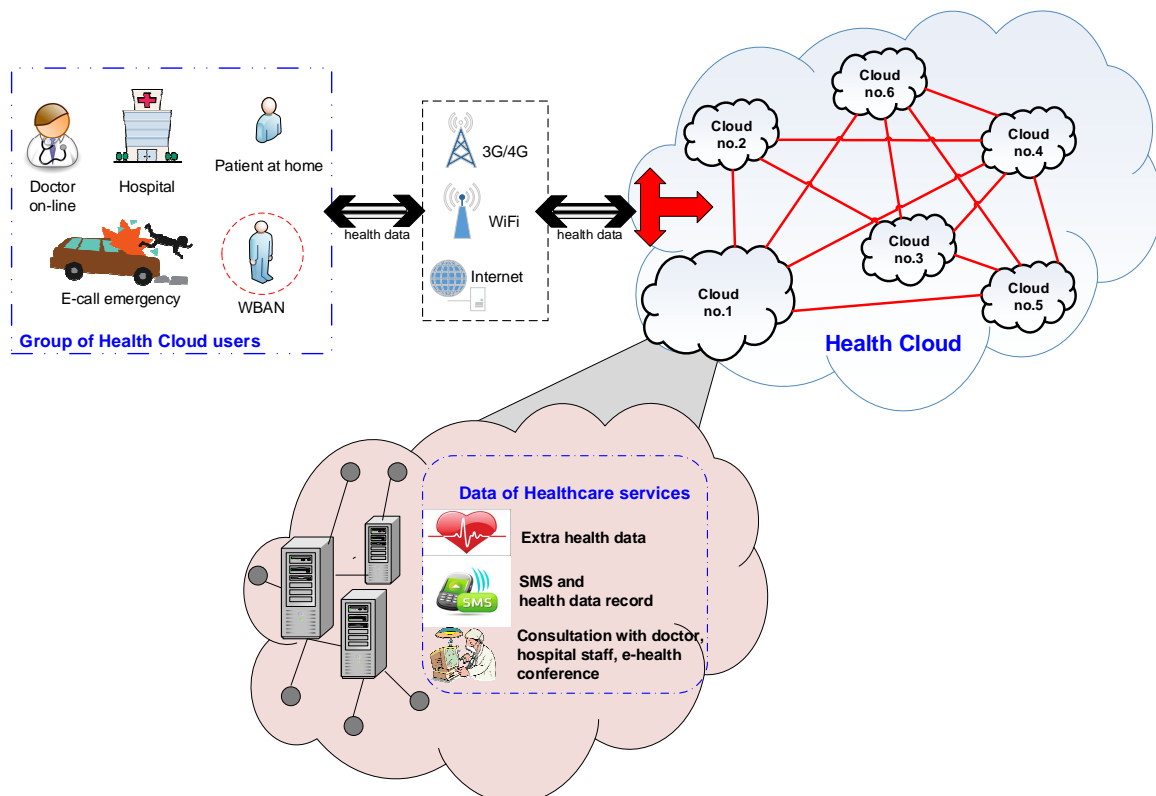


Figure 1. The structure of health data transmission over Health Cloud

One of the critical factors in this is a time interval between path request and a reply to this request. This is the duration for the medical data route selection over Health Cloud. Moreover, it must be as short that cannot cause blockage at the path

request and a reply time due to the resource reservation. If this duration will be too long, the resources that were available during the path request may be inaccessible and block the performance of the services. Due to this, the selection of route for data

transmission over Health Cloud based on QoS requirements is very problematic challenge for cloud service providers and it will be analyzed in this paper. The results for QoS-based route selection in Healthcare Cloud can simplify the complexity in cloud networking and increase the efficiency of services' provision. And this is one of the biggest steps towards the autonomous control for Healthcare as a Service (HaaS) [4] over Cloud.

The remainder of this paper is organized as follows: the structure of the health data transmission over Health Cloud and the authors' proposed analytical model for routing path selection are in Section II. Section III describes the results of the investigations from QoS based route selection over Health Cloud as multi-cloud system. Finally, Section IV concludes the paper and gives the new ideas for the future work on autonomous control for HaaS.

2. THE PROPOSED ANALYTICAL MODEL FOR HEALTH DATA ROUTING PATH OVER HEALTH CLOUD

The investigations of health data routing over Health Cloud were carried out for the structure, which is presented in Figure 1. The Health Cloud is designed as inter-cloud system with six different cloud service providers, where the medical services can be displaced from one cloud service provider to another. The users of such Healthcare system can be:

- patients at home;
- users, who are using services over Wireless Body Area Network (WBAN);
- doctors, who are using on-line consultation with their patients;
- staff in hospital, who records any medical documents into databases;
- paramedics, who provide emergency assistance to the patients at home or during any accident (as E-call emergency).

All health data from main Healthcare services are grouped into three groups with different priorities for guaranteed quality of service level:

- a) Low priority – on-line doctor's consultation, e-health conference'
- b) Best Effort – SMS, health data records
- c) High priority – extra health data (from emergency assistance);

All investigations for QoS based route selection over Health Cloud were done by using MATLAB

simulation platform. The authors' proposed analytical model for routing path selection is presented in Figure 2.

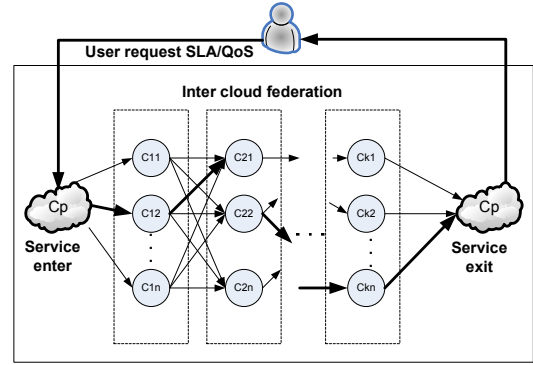


Figure 2. The analytical model for service path request/reply over Healthcare Cloud

General QoS routing problem is to ensure that users transfer data from the source point to the end point, so as to offer end-to-end quality assurance. A typical end-to-end provisioning system for composite network–Cloud services consists of both computing infrastructure that offers Cloud services and network services for Cloud access and inter-Cloud communications. If the end user wants a certain level of performance guarantee from the composite service provisioning, the end user must expect a certain level QoS from each network and Cloud service. The Health Cloud network can be described as an undirected weighted graph. A network is denoted by a graph

$$G(N, L); u \rightarrow v, u, v \in N, \quad (1)$$

where N is the set of nodes, L is the set of links.

Each link can be characterized by a link weight vector \vec{w} consisting of K link metrics. In our case QoS metrics can be

- additive: delay, jitter, in which case the path-weight vector consists of summing the link-weight vectors of the links defining the path

$$D(\text{path}(i, j)) = \sum_{N \in p(i, j)} d(N) + \sum_{L \in p(i, j)} d(L);$$

- min-max: bandwidth in which case the minimum (or maximum) link weight defines the weight of a path.

$$B(\text{path}(i, j)) = \min_{L \in p(i, j)} \{B(L)\}$$

A multicriteria QoS routing approach consists of taking into account all objective metrics of all different services. All metrics have different weight according

with QoS requirements of services and them priorities. For evaluating the route we calculate cost function:

$$Cost \rightarrow f(C1_{QoS}, C2_{QoS} \dots) \quad (2)$$

Every path cost function are calculate use equation:

$$Cost = w_i D_i + w_n U_n + \dots w_m B_m \quad (3)$$

The the total QoS routing is

$$QoS_{route} = \min\{Cost_1, Cost_2 \dots Cost_n\} \quad (4)$$

3. RESULTS OF INVESTIGATIONS

The investigations were done in different scenarios: 1) routing path for health data with different priorities; 2) routing path for health data without priorities, but in shortest way; and 3) routing path with minimum QoS cost for service provision (Figures 3–5) The results showed, that the shortest way to provide any Healthcare service is the same for all health services without priorities. However, if the service is with the high priority, such data will be transmitted in shortest way, comparing to other

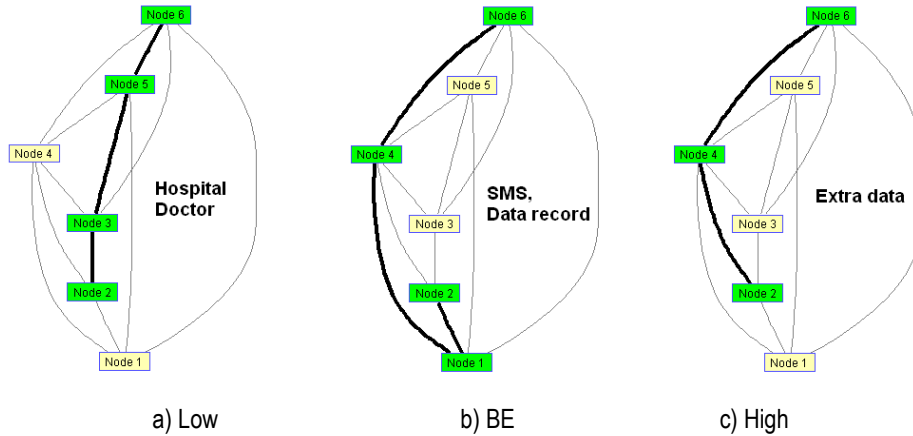


Figure 3. Routing path for health data with different priorities

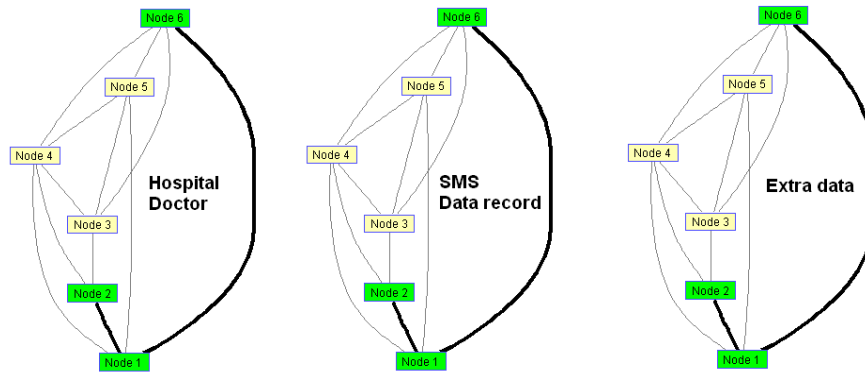


Figure 4. Routing path for health data without priorities, but in shortest way

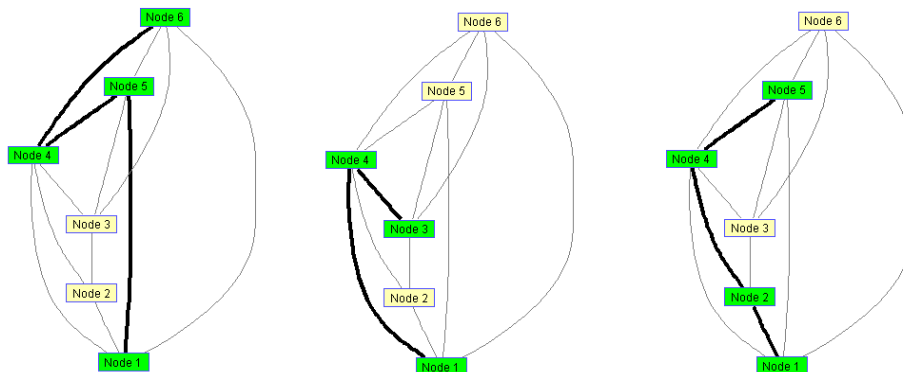


Figure 5. Routing path with min QoS cost to provide service (low priority)

medical services. On the other hand, if the health service is with priorities, the routing path over inter-cloud system will be through clouds, which are not overloaded at that moment and the resource reservation is in minimum cost of quality resources as time for path request/reply, delay, bandwidth, etc. (Fig. 5).

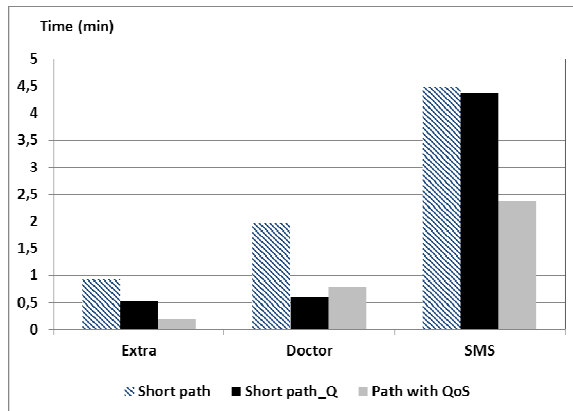


Figure 6. Time of path request and reply

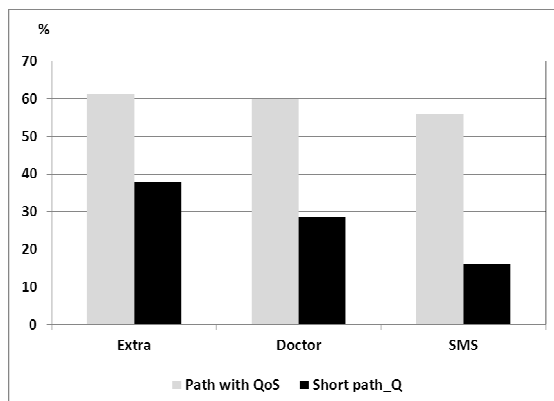


Figure 7. The percentage difference for time of path request and reply

The results for time of path request and reply (Fig. 6) approved that, health data routing with guaranteed QoS level increase the efficiency of medical service provision over Healthcare Cloud in 60% for high and low priority, and in 55% – for BE, in compare with the health data transmission without QoS requirements.

CONCLUSIONS

The investigations for QoS-based route selection over Healthcare Cloud showed, that the health data transmission with guaranteed QoS level can increase the efficiency of medical services' provision in 2 times and simplifies the complexity in multi-cloud infrastructure providers by reserving best resources with min QoS cost for service provision. As Healthcare Cloud should be deployed in reliable communication, the networking aspect of health data (routing model) over inter-cloud system can be used in autonomous control for Healthcare as a Service.

ACKNOWLEDGMENT

This work has been partially supported by the ICT COST Action IC1304 - Autonomous Control for a Reliable Internet of Services (ACROSS), November 14, 2013 – November 13, 2017, funded by European Union.

References

- [1] Department of Health and Human Services, "Health Insurance Reform: Security Standards", *Federal Register*, vol. 68, no. 34, 2003, p.p 8332-8381.
- [2] R., Moreno-Vozmediano; R.S., Montero and I.M., Llorente, "Key Challenges in Cloud Computing: Enabling the Future Internet of Services", *IEEE Internet Computing*, vol. 17, issue 4, 2013, pp. 18-25.
- [3] R., Chauhan; A., Kumar, "Cloud Computing for Improved Healthcare: Techniques, Potential and Challenges", in *proceedings of the 4th IEEE International Conference on E-Health and Bioengineering*, Romania, November 21-23, 2013, pp. 1 – 4.
- [4] N., John; S., Shenoy, "Health Cloud – Healthcare as a Service (HaaS)", in *proceedings of International Conference on Advances in Computing, Communications and Informatics*, New Delhi, September 24-27, 2014, pp. 1963 – 1966.
- [5] H., Mohamad; N., Mbarek; O., Togni, "Self-establishing a Service Level Agreement within Autonomic Cloud Networking Environment", in *proceedings of IEEE Network Operations and Management Symposium*, Krakow, May 5-9, 2014, pp. 1 – 4.

ON DIGITAL IMAGES SEGMENTATION BASED ON FRACTAL AND MULTIFRACTAL METHODS

N. Ampilova

St. Petersburg State University, Math. & Mech. Faculty, n.ampilova@spbu.ru

I. Soloviev

St. Petersburg State University, Math. & Mech. Faculty, i.soloviev@spbu.ru

Abstract

Segmentation as an important step in image processing is widely used to analyze medical images, faces, images of the Earth surface and many others. For complex textures and high resolution images fractal and multifractal methods often lead to better results than classical ones, because they seem to be more sensitive to intensity changes. In this work we apply fractal and multifractal methods to analyze biomedical preparation images. Both methods allow us to obtain numerical characteristics and perform the based on them segmentation.

1. INTRODUCTION

The common practice in image analysis is to apply several methods and compare results. The applicability of a given segmentation method depends on the problem under investigation. For complex texture images researches segmentation algorithms are based on fractal and multifractal analysis. Such an approach is suitable for high resolution images containing large number of fine details.

Textures are often may be considered as fractal (or multifractal) sets. Fractal sets have a self-similarity property that may be characterized by a scaling exponent. These exponents are base to define a fractal dimension (or several dimensions) of the set. In practice the class of so called box-computing dimensions (e.g. capacity dimension) is widely used [5]. A set M is covered by $N(\varepsilon)$ boxes with a side ε . It is assumed that the number of boxes is proportional to $\varepsilon^{-\alpha}$. Decreasing ε and taking the limit of $\frac{\ln N(\varepsilon)}{\ln \frac{1}{\varepsilon}}$ we obtain the value of α , which is called capacity dimension of M . For greyscale (or monochrome) images the Minkovsky dimension is more appropriate [5].

A union of several fractals, which of them has its own fractal dimension, is called multifractal. Such sets may be characterized not one by several scaling exponents. As components of multifractals are usually arranged by a complex way, segmentation problem by classical methods may be not very easy. Hence we may use scaling components as characteristics by which we combine image pixels

in subsets: namely, we assume that elements (cells of an image partition) with close exponents (or dimensions) belong to the same set.

In fractal methods it is convenient to calculate the fractal signature or the Minkovsky dimension for each cell of a given partition. Multifractal methods are based on the assumption that there is a measure defined on the image. Such a measure is given in terms of pixel intensities. Measure of a cell may be defined as the sum of pixel intensities or as the relation of the number of pixels having a given intensity to the common number of pixels. For multifractal methods one also assume that the measure of i -th cell $P_i(l) \sim l^{\alpha_i}$, where α_i are called singularity (scaling) exponents. Fractal dimensions of subsets of cells with close values of exponents form multifractal spectrum.

But for segmentation it is sufficient to use only singularity exponents.

In this work we consider two methods for image segmentation: modified fractal signature and multifractal analysis ones. The first method is based on the construction of the grey level function graphics for a greyscale image and calculation of the surface area for this graphic. This method is based on the blanket technic and was described in detail in [5, 10]. Using the area value we obtain a special characteristic — fractal signature and the Minkovsky dimension. The method was successfully applied to analyze text documents [11], ISAR images [6, 8, 9] and images of biomedical preparations [1-3]. The segmentation may be performed by a partition of

the image on cells, calculation fractal signature (or the Minkovsky dimension) and marking the cells by a color in accordance with the obtained value.

The second method is a modification of calculation of multifractal spectrum by using so called density function [13]. The image is divided on subsets of points that have close values of density function (level sets). The set of fractal dimensions of level sets is multifractal spectrum. This method was used to obtain level sets for different biomedical images [4]. We propose to optimize this approach and calculate density function for a small base cell. The size of cell is a parameter. Experiments show that such an optimization speeds up run time considerably and does not affect visibly on segmentation results.

2. FRACTAL SIGNATURE METHOD

The idea of the method is to calculate fractal dimension of the surface formed by the graphic of the grey level function for a given image. To do it we calculate the approximate value of the surface area, and this area may be obtained by using the volume of a special object.

Let $F = \{X_{ij}, i = 0, 1, \dots, K, j = 0, 1, \dots, L\}$ be an image with multigray level and X_{ij} be the gray level of the (i, j) -th pixel. In image processing the gray level function F is a nonempty bounded set in R^3 . The surface area A_δ may be calculated using the volume Vol_δ of a special δ -parallel body — blanket with the thickness 2δ [5].

$$A_\delta = \frac{Vol_\delta - Vol_{\delta-1}}{2}.$$

The expression $S_\delta = \frac{\log_2 A_\delta}{\log_2 \delta}$ is called fractal signature. Fractal dimension of the surface is defined by the formula

$$D \approx 2 - \frac{\log_2 A_\delta}{\log_2 \delta}.$$

In practice the approximate value of S_δ is obtained by the least square method as the slope of the line in axes $(\log_2 \delta, \log_2 A_\delta)$.

For segmentation we do the following. Partition the image into n cells by size $N \times N$ and then for $k = 1, 2, \dots, n$ calculate grey level functions F^k , u_0^k and b_0^k , u_δ^k and b_δ^k (for $\delta = 1, 2, 3$), Vol_δ^k and A_δ^k .

By the least square method calculate approximate values

$$S^k = \lim_{\delta \rightarrow 0} \frac{\log_2 A_\delta^k}{\log_2 \delta}.$$

Mark the cell having close values S^k by the same color.

3. CALCULATION OF DENSITY FUNCTION

3.1. Base method

In what follows we use the definition given in [13]. Let μ be a measure defined through pixel intensities. For $x \in R^2$ we denote $B(x, r)$ a square of length r with center x . Let $\mu(B(x, r)) = kr^{d(x)}(x)$ where $d(x)$ is the local density function of x and k some constant. Then

$$d(x) = \lim_{r \rightarrow 0} \frac{\log \mu(B(x, r))}{\log r}.$$

The density function measures the non-uniformity of the intensity distribution in the square $B(x, r)$. The set of all points x with local density α is a level set

$$E_\alpha = \{x \in R^2 : d(x) = \alpha\}.$$

In practice, not to increase the number of level sets, one really consider sets

$$E(\alpha, \varepsilon) = \{x \in R^2, d(x) \in [\alpha, \alpha + \varepsilon)\}.$$

It is clear that showing level sets results in a segmentation of the image. This approach was successfully applied in [4] to analyze biomedical preparation images.

3.2. Modification

It is easy to note that in segmentation problem we do not need to calculate multifractal spectrum. Hence we can use density functions (that are a sort of singularity exponents for one point). As the computing this function for every point of the image may be time-consuming we calculate it for a small base cell.

Let l be a side of a base cell, the measure (the sum of pixel intensities) of i -th cell be $\mu_i(l)$, and density function — α_i .

In this case for segmentation we partition the image into n base cells by size $l \times l$ and for $i = 1, 2, \dots, n$ calculate $\mu_i(l)$, select neighbourhoods of base cells by size $(l + 2) \times (l + 2)$ and

$(l + 4) \times (l + 4)$, calculate $\mu_i(l + 2), \mu_i(l + 4)$. By the least square method using points $(\ln l, \ln \mu_i(l)), (\ln(l + 2), \ln \mu_i(l + 2))$,

$(\ln(l + 4), \ln \mu_i(l + 4))$ calculate approximate values α_i . Mark base cells with close values of α_i by the same color.

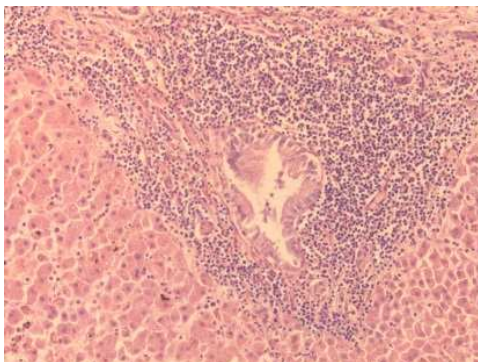
The number of colors depends on the range of exponent values.

4. NUMERICAL EXPERIMENTS

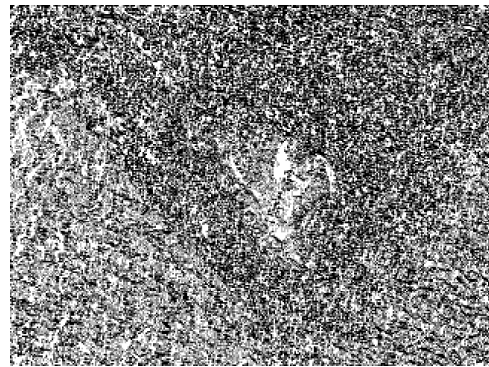
The experiments were performed for biomedical preparations images including high resolution ones. For color images numerical characteristics were obtained for all components of RGB palette. The number of colors used for segmentation was selected in accordance with the range of fractal signatures (the method of fractal signature) and the range of density function for base cells (the method of multifractal spectrum calculation). The results show that for complex textures multifractal method leads to better results.

4.1. Liver tissue

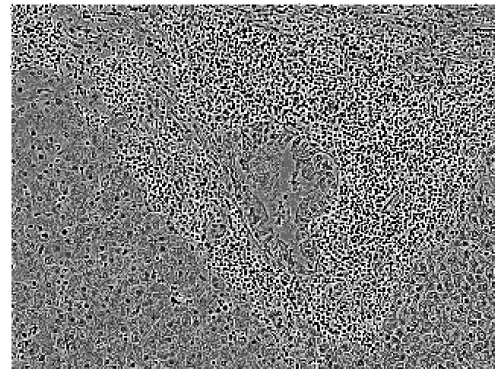
We considered high resolution image of liver tissue (chronic cholangitis). The image size is 2584×1936 . The results are shown for R component of RGB. We use the following notations: l — a cell side, nc — the number of colors. The fractal signature method localizes objects more clearly, whereas the multifractal one shows an averaged common structure. Both the results are important for analysis. We note that the selection of small l may not result in a finer segmentation. This depends on the image structure and the size of homogeneous segments. The most optimal values of parameters (l, nc) are selected experimentally.



a



b

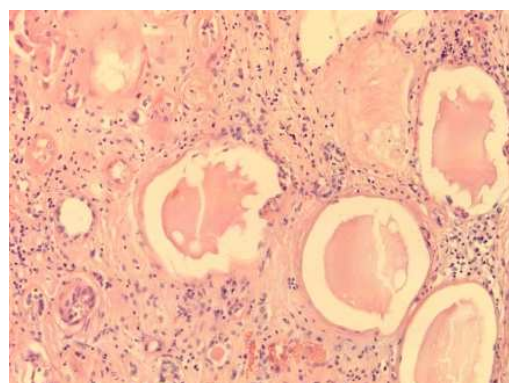


c

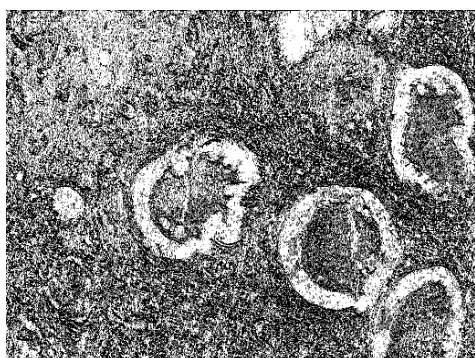
Fig.1a – the initial image; b – application of fractal signature method ($l = 8, nc=5$); c – application of multifractal method ($l = 8, nc=6$)

4.2. Kidney tissue

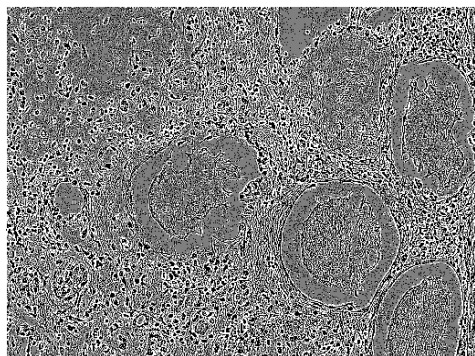
The image of kidney with chronic pyelonephritis was analyzed. The experiments were performed for all components of RGB. The results are shown for R component. The both methods give clear localization of main objects, but multifractal one reveals fine details more clearly.



a



b



c

Fig. 2a – the initial image; b – application of fractal signature method ($l = 5$, $nc=3$); c – application of multifractal method ($l = 5$, $nc=3$)

5. CONCLUSION

Complex textures and high resolution images often have fractal structure. Hence fractal and multifractal methods may be used for their analysis. As a result we obtain a set of numerical characteristics that may be used as classification signs. Moreover, these characteristics may be a base for natural image segmentation. Experiments show that these methods are often more preferable because they are very sensitive to pixel intensity changes.

ACKNOWLEDGMENTS

The work was partially supported by RFBR grant 13-01-00782.

References

- [1]. N. Ampilova, E. Gurevich, I. Soloviev. Application of Modified Fractal Signature & Regny Spectrum Methods to the Analysis of Biomedical Preparations Images. Proc. 6 Int. Conf. CEMA11, 6-8 Oct. 2011, Sofia, Bulgaria. p. 96-100.
- [2]. N. Ampilova, I. Soloviev, Y. Shupletsov. On Application of Fractal Analysis Methods to Biomedical Preparation Images. e-journal "Differential equations and control processes", www.math.spbu.ru/diffjournal, no. 2, 2013, p. 51-61.
- [3]. N. Ampilova, I. Soloviev, Y. Shupletsov. On some aspects of the fractal signature method. Proc. 8 Int. Conf. CEMA13, 17-19 Oct. 2013, Sofia, Bulgaria. p.80-84.
- [4]. N.Ampilova, Y.Shupletsov. Image segmentation algorithm based on multifractal spectrum computing. Proc. 9 Int. Conf. CEMA14, 16-18 Oct. 2014, Sofia, Bulgaria. p. 39-42.
- [5]. Falconer, K.J. Fractal geometry: mathematical foundations and application. – John Wiley & Sons, 1990.
- [6]. P. Frangos, C. Pandis, A. Malamou, P. Stefaneas. Applying the modified fractal signature method to image classification: some preliminary results for ISAR radar images. Proc. 7 Int. Conf. CEMA12, 8-10 Nov. 2012, Athens, Greece . p. 50-52.
- [7]. M. Ganesh and Dr. V. Palanisamy, High resolution MRI brain image segmentation technique using Holder exponent. International Journal of Soft Computing (IJSC),vol.3,no.4,2012,p.39-51.
- [8]. A. Malamou, C. Pandis, P. Frangos, P.Stefaneas. SAR image terrain classification using the modified fractal signature (MFS) method. Proc. 9 Int. Conf. CEMA14, 16-18 Oct. 2014, Sofia, Bulgaria . p. 8-11.
- [9]. A. Malamou A., C. Pandis, A. Karakasiliotis A., P. Stefaneas P.,D. Kodokostas, P. Frangos. Application of an autofocus algorithm for SAR image quality improvement and application of the modified fractal signature (MFS) method for SAR image classification for the case of real radar data. Proc. 8 Int. Conf. CEMA14, 17-19 Oct. 2013, Sofia, Bulgaria . p.108-111.
- [10]. S. Peleg, J. Naor, R. Hartley, D. Avnir. Multiple Resolution Texture Analysis and Classification.// Transactions on pattern analysis and machine intelligence, Vol. PAMI-6, NO. 4, JULY 1984.
- [11]. Tang Y. Y., Hong Ma, Dihua Xi, Xiaogang Mao, C. Y. Suen. Modified Fractal Signature (MFS): A New Approach to Document Analysis for Automatic Knowledge Acquisition. — IEEE Transactions On Knowledge and Data Engineering, vol.9, no. 5, 1997, pp. 747-762.
- [12]. M. Voorons, Y. Voirin, G. B. Benie, K. Fung. Very high spatial resolution image segmentation based on the multifractal analysis. In Proc.of 20th ISPRS,2004
- [13]. Xu Y., Ji H., Fermüller C. Viewpoint Invariant Texture Description Using Fractal Analysis. — International Journal of Computer Vision, no. 83, 2009, pp. 85–100

ON A VISUALIZATION OF LOW FREQUENCY MAGNETIC FIELDS BY USING PARAVIEW PACKAGE

B. Kudrin

St. Petersburg State University, Math. & Mech. Faculty, bogdan.kudrin@gmail.com

V. Nikolov

Technical University of Sofia, Faculty of Telecommunications, v_nikolov@tu-sofia.bg

Abstract

In this work we describe a process of visualization of low-frequency magnetic field generated by several coils. The technic was applied to visualize the magnetic field occurring in a special magnetotherapy device — magneto bed. The obtained image shows a patient position, coils, and the magnetic field distribution in the area of coils action. To do this we use Paraview tools, body model and the special scenario – Python language script.

1. INTRODUCTION

It is well known that the calculation and visualization of the low-frequency or constant magnetic field is both a time-and memory consuming. The computation depends on the environment geometry, field influence and the visualization method.

But in the case when we consider the magnetic field generated by a coil (that is the most frequent element in magnetotherapy devices) we can use a mathematical model where the superposition principle is applied: in this case due to constant current value the induction and self-induction are supposed to be negligible quantities and the common magnetic field is the sum of the fields generated by the contours of a coil. For several coils the magnetic field is the sum over all the coils.

In [1] this problem was solved for 3D case – the magnetic field was calculated in the points of 3D grid. In [2-4] some method for interpolation of magnetic field have been implemented. The visualization algorithms of obtained values of magnetic field were discussed in [5,6] and implemented by using Paraview package [7]. The result of the visualization showed the lines of magnetic fields in different ways depending on a selection of Paraview parameters. But such images did not show the patient position.

In this work we consider a method of visualization that shows a patient position, coils, and the magnetic field distribution in the area of effect on the patient body. To do this we use Paraview tools, body model and the special scenario – Python language [8] script. Such a scheme allows us to select

a pair of coils and corresponding data file (results of calculation or interpolation) and perform the visualization. We also may to watch all the pairs step by step. Such a visualization is a practical tool and may considerably help a physician in the estimation of magnetotherapy effects.

2. VISUALIZATION OF MAGNETIC FIELD FOR MAGNETIC BED

We used a system for magneto-therapy called “magnetic bed” (Fig. 1). In every moment only one pair of coils is active. In the process of the system functioning every pair of coils is active by turns and a movement of magnetic field occurs. The order of the choice of pairs of coils is defined by a data table. The number of every coil and the coordinate system XYZ are shown on the Fig. 1.

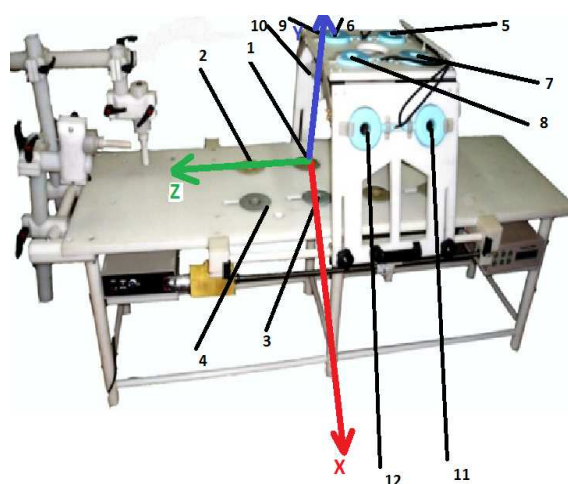


Fig. 1. Magnetic bed and the disposition of coils

In previous works we calculated magnetic field generated by a given pair of coils both by mathematical model and the interpolation using experimental data. To visualize the obtained results we use Paraview package that allows us to show the lines of magnetic field in various regimes.

It should be noted that in the package there are tools to interpolate data for better visualization, in other words Paraview performs an interpolation automatically if necessary.

There is a possibility to show a patient position schematically. For this purpose we use a template from [9] (the file has extension .stl) and Blender package to edit 3D images [10]. To repeat similar actions for different pairs of coils it is convenient to write scenarios (scripts), i.e macros which you may run with given parameter values. Scenario files are written in Python language and have extension .py. One can write script for a pair of coils or for several ones. We may use a list of coils (where all the pairs and their parameters are given in a definite order) to obtain a script to visualize step by step all the given combinations.

In this work we used results of calculation for the following pairs of coils: (1-5),(1-7),(1-9),(3-11),(1-3),(1-11),(3-7)

The obtained data files are numbered in accordance the order in the list of coil pairs. The order of the selection of a result file is given by the user in the script. In our experiments we follow the list of coil pairs, but it may be changed easily.

3. MAIN STEPS FOR VISUALIZATION

3.1. File loading

To visualize in Paraview the results of calculation (or interpolation by using experimental data) of magnetic field we have to load the data file: *File – Open*. Select the file required and click the button *Apply*. Data files have extension .vtk.

3.2. Primitive adding

If we tend to show the position of coils and the bed schematically in accordance with their sizes, we should use so called primitives or primitive objects (cylinder, line, plane, sphere, etc) by performing the following actions:

Find in menu item *Sources*, select the necessary object and then on the inlay *Properties* set up its parameters and click button *Apply*.

3.3. Object transformation

To set the primitive in the right position, which in our case is defined from the bed size and the position of the coils in the space we have perform a transformation. To do it we should select it in Pipeline Browser, then select *Filters – Alphabetical – Transform*. On the inlay *Properties* set up the parameters and click the button *Apply*

3.4. Resampling

To add a model in the image (to show a patient body position) we should use a template. After the definition of parameters for primitive objects and the template we can form a final image. It is performed as follows: Select a model (file with extension .stl) in *Pipeline browser*, then select *Filters – Alphabetical – Resample with Dataset*. The file with numerical data should be taken as *Input*, file of the model as *Source*. When clicking *Apply* we apply the obtained magnetic field to the model. To set up color scale we use the inlay *Properties* (item *Colors*).

We see that it is very time consuming to repeat the same actions many times. Hence we should write macros (scenario) that describes all necessary steps.

4. HOW TO RUN A SCENARIO

When working we select *Tools – Start Scenario-name*. Then we define the required parameters, perform actions and select *Tools – Stop Scenario-name*.

An example of the scenario written in Python language may be the following.

In the text the primitive objects (that will show the coils) are created. The parameters of the objects are set up in accordance with their sizes in the magneto bed construction.

```
from paraview.simple import *
from paraview.simple import *
import time
##### disable automatic camera reset on
'Show'
paraview.simple._DisableFirstRenderCameraReset()
# get active view
renderView1 = GetActiveViewOrCreate('RenderView')
# uncomment following to set a specific view size
```



```

# renderView1.ViewSize = [808, 783]
# reset view to fit data
renderView1.ResetCamera()
# create a new 'Cylinder'
cylinder1 = Cylinder()
# Properties modified on cylinder1
cylinder1.Height = 34.0
cylinder1.Radius = 58.0
cylinder1.Center = [184.0, 500.0, 116.0]
cylinder1.Capping = 0
# show data in view
cylinder1Display = Show(cylinder1, renderView1)
# trace defaults for the display properties.
cylinder1Display.ColorArrayName = [None, ""]
# create a new 'Cylinder'
cylinder2 = Cylinder()
# Properties modified on cylinder2
cylinder2.Height = 34.0
cylinder2.Radius = 58.0
cylinder2.Center = [416.0, 500.0, 116.0]
cylinder2.Capping = 0
# show data in view
cylinder2Display = Show(cylinder2, renderView1)
# trace defaults for the display properties.
cylinder2Display.ColorArrayName = [None, ""]
# create a new 'Cylinder'
cylinder3 = Cylinder()
# Properties modified on cylinder3
cylinder3.Height = 34.0
cylinder3.Radius = 58.0
cylinder3.Capping = 0
# create a new 'Transform'
transform2 = Transform(Input=cylinder3)
transform2.Transform = 'Transform'
# Properties modified on transform2.Transform
transform2.Transform.Translate = [550.0, 250.0, 116.0]
transform2.Transform.Rotate = [0.0, 0.0, 100.0]
# show data in view
transform2Display = Show(transform2, renderView1)

```

```

# trace defaults for the display properties.
transform2Display.ColorArrayName = [None, ""]
# create a new 'Cylinder'
...

```

5. VISUALIZATION ALGORITHMS

Hence the visualization algorithm may be the following:

- Calculate magnetic field induction for given pairs of coils. Number the obtained files in accordance with the list of coil pairs.
- Put in a working directory obtained data files, file containing 3D model of a body (template) and script file. In the script file the path to the working directory is given.
- Load script in Paraview and run it. When script running we see the picture of magnetic field distribution.
- Save screenshots by using Paraview tools
- Stop script running.

The block scheme of the algorithm is the following.

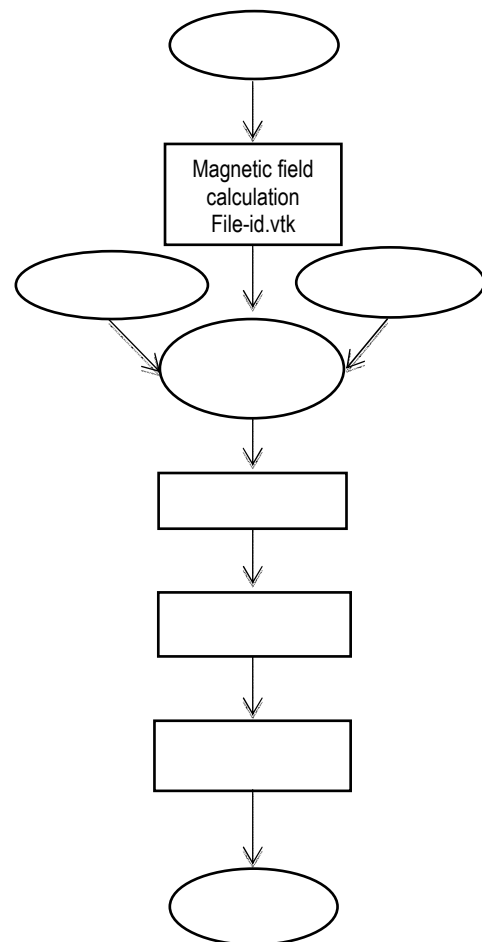


Fig. 2. Algorithm for the configuration of magnetic bed coils

Examples of visualization



Fig. 3. Visualization results for the pair of our-of-line coils

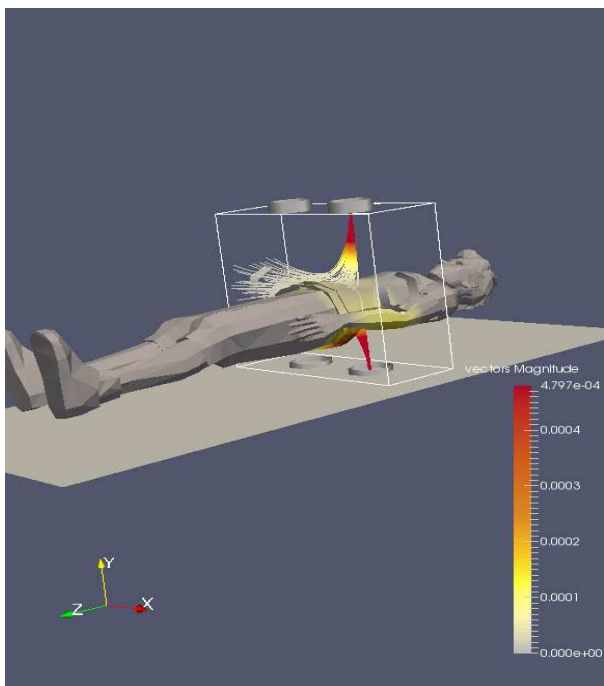


Fig. 4. Visualization results for the pair of coaxial coils

6. CONCLUSION

The implemented technic allows us to visualize the numerical data obtained by the calculation or interpolation of low-frequency magnetic field such that the position of a patient and the coils are shown. We use freeware packages Paraview and Blender, and templates for 3D images. To optimize the process of showing we use the Python language script. All the calculation may be performed before the visualization. The described method may be used for any magnetotherapy device.

7. ACKNOWLEDGMENTS

The work was partially supported by RFBR grant 13-01-00782.

References

- [1] N. Ampilova, D. Dimitrov, B. Kudrin. Mathematical modeling of low frequency magnetic field in systems for magnetotherapy . Proc. 8 Int. Conf. CEMA13, 17-19 Oct. 2013, Sofia, Bulgaria. p. 48-51.
- [2] B. Kudrin, I. Soloviev. On interpolation methods of low frequency magnetic field in systems for magnetotherapy. Proc. 9 Int. Conf. CEMA14, 16-18 Oct. 2014, Sofia, Bulgaria. KING 2001, p.154-157. ISSN 1314-2100.
- [3] B. Kudrin, V. Nikolov. Algorithms of interpolation and visualization of low frequency magnetic field using experimental data. Proc. 9 Int. Conf. CEMA14, 16-18 Oct. 2014, Sofia, Bulgaria. KING 2001, p.43-45. ISSN 1314-2100.
- [4] B. Kudrin, V. Nikolov. On the mathematical model of interpolation of low frequency magnetic field using experimental data. Proc. 9 Int. Conf. CEMA14, 16-18 Oct. 2014, Sofia, Bulgaria. KING 2001, p.80-84. ISSN 1314-2100.
- [5] B. Kudrin, A. Dimitrov. An algorithm for visualization of low-frequency magnetic signals in systems for magnetotherapy. Proc. 8 Int. Conf. CEMA13, 17-19 Oct. 2013, Sofia, Bulgaria. p.31-35.
- [6] B. Kudrin, A. Dimitrov. Computer visualization of low-frequency magnetic signals in systems for magnetotherapy with variable parameters. Proc. 8 Int. Conf. CEMA13, 17-19 Oct. 2013, Sofia, Bulgaria. p. 36-39.
- [7] ParaView Tutorial:
<http://paraview.org/Wiki/images/d/d5/ParaViewTutorial398.pdf>
- [8] Python programming language:
<http://www.docs.python.org>
- [9] <http://tf3dm.com/3d-model/boy-10833.html>
- [10] <https://www.blender.org/>

PERSONAL DATA PROTECTION FOR MEDICAL ASSISTIVE SYSTEM USED BY MOTOR DISABLED PATIENTS BASED ON MPEG-21 SCHEMAS

Ivo R. Draganov, Ognian L. Boumbarov

Radiocommunications and Videotechnologies Dept.
Faculty of Telecommunications, Technical University of Sofia
8 Kliment Ohridski Blvd., 1756 Sofia, Bulgaria
e-mail: idraganov@tu-sofia.bg, olb@tu-sofia.bg

Darko Brodić

University of Belgrade, Technical Faculty in Bor
Vojske Jugoslavije 12, 19210 Bor, Serbia
e-mail: dbrodic@tf.bor.ac.rs

Abstract

In this paper is proposed a general model for personal data protection of motor disabled patients who use recently developed medical assistive system for rehabilitation. During the predefined exercises by medical personnel an overall evaluation is done for the degree of completeness of each prescribed movement based on audio-visual and inertial sensor record. All this data needs to be protected from unauthorized access so here a systematic mean is proposed for the purposed based on MPEG-21 schemas for protection of digital resources.

1. INTRODUCTION

In a number of fully or semi-autonomous medical assistive systems specially designed for rehabilitation of people with various disabilities arises the need of introducing a robust approach for the personal data protection of the patients. A recently developed system of the kind [1] posed the same problem. Instead of developing an independent protocol for data storage, processing and transmitting here a more flexible approach is suggested by incorporating the well defined and widely approved MPEG-21 [2-8] schemas for intellectual property protection adapted for the current specific purpose. With a slight change of the existign xml-definitions from the standard it is possible to establish a fully portable framework for personal data protection of the patients.

2. RIGHTS EXPRESSION LANGUAGE (REL)

REL is designed as a machine-interpreted language by which to declare rights and permissions using the definitions from the dictionary with data rights (RDD).

In REL is set flexible, open mechanism to ensure transparent and increased use of multimedia resources. Discussed are ways to access and manage non-commercial redistributable resources that

are extremely personal content with the goal of protecting privacy.

REL guarantees and the possibility of interaction of "the end user – to an end user" regardless of the systems and devices. This implies wealth and extensibility when declaring the rights, conditions and obligations; ease and consistency in identification and association of these properties for each resource, as well as flexibility to support multi-business models.

MPEG REL adopts a simple and flexible model for many of its key concepts and elements. MPEG REL Information Modeling for defining the rights consists of four basic elements (Fig. 1). The relationship between them is defined by MPEG REL highlighting permission.

Principal	Resource	Condition
Right		

Figure 1. Information model of REL

Structurally it consists of:

- Primary user (Principal), who provides this permission;
- The right (Right), which defines permission;

- Resources (Resource), to which the law of permission applies;
- condition (Condition), which must be fulfilled before the right can be applied.

Primary user can represent multiple users who are given appropriate rights by permissions. Each primary user represents just one country through its unique content of information by proving his own identity. This type of identification supports the following technologies:

- Main users representing multiple proxies, the identity of each of which must be checked for authenticity;
- Marketing key to mean an individual who possesses the secret key, such as a private key encryption system, working with a pair of keys - public and private;
- Emerging technologies of identification.

The law is a set of actions that allowed the main user to exercise on a resource under certain conditions. MPEG REL defines an element which comprises information about the rights for those that are often used, and for the more specific ones. These are as rights for publication, cancellation and receipt. There are extensions to the MPEG REL to define specific rights such as to be viewed and printed at the printer and an e-record.

Resource is the object for which the main user receives certain rights. It may be a product or service. MPEG REL provides a mechanism for packing the information necessary for the identification and use of a single resource or resources that correspond to a certain class, i.e. characterized by similar parameters correspond to the particular business model or technical administration.

The condition determines the period, permissions and obligations in respect of which a right is exercised. Condition is just a time interval within which the right may be exercised. Slightly complicated condition is one in which requires a valid law, provided the main user. Using this mechanism the exercise of a right can become dependent on the exercise of other rights.

MPEG REL defines a separate element which covers the information on the conditions. Extensions to MPEG REL define and conditions suitable for specific use in consumer models as a watermark for example.

The main elements in the data model of the MPEG REL: basic user (principal), right (right), resource (resource) and condition (condition) can match (but not necessarily be equivalent) user (user, including Terminal), right (right), a digital object (Digital Item) and condition (condition) in the terminology of MPEG-21 Part 1.

Since MPEG REL is defined using XML schema recommendation of the W3C (World Wide Web Consortium), its elemental model follows the standard that connects some elements with classes from other elements. Example item permission (grant) is connected to its successor elements: the core consumer law resource and condition.

In the development of medical-based system, the subject of this study, as it's shown below, will use defined in this part of the standard language, namely REL. Here only it's pointed out the most important features and it's emphasized its importance in the design and maintenance of large complex systems for the organization and delivery of multimedia resources according to MPEG-21. The full specification defining specific rules in syntax and semantics, as well as the inevitable exceptions to them are given in [6].

3. RIGHTS DATA DICTIONARY (RDD)

Part 6 of the MPEG-21 is a natural continuation of the previous section 5. RDD includes a set of clear, consistent definitions that make up the base of REL, which integrate without controversy in it, but also to preserve their uniqueness matter. The structure of the dictionary is defined in parallel with the methodology of its creation. The means by which you can create new definitions are also addressed in this part of the standard. In this sense, the term RDD hiding two separate entities – first standard (Part 6) defining the means and rules to create new definitions, the other - the full range of already existing ones, which come into immediate use.

The dictionary is normative in the sense that it defines clearly important for any term (term), represented by separate RDD title (headword), but also recognizes the description of other RDD titles created by other sources and registers them by identical transformations defined in this Part 6 of MPEG-21.

There are four specific mechanism by which the terms defined in RDD in the above template can be presented in REL:

1. REL multimedia rights (multimedia rights) and RDD nudity type (act types) - REL defines a set of XML complex types using a base abstract type parent right (right). These newly types fall in the namespace urn: mpeg: mpeg21: 2002: 01-REL-NS. Any action in respect of multimedia resources in certain contexts may be related to the type of acts within the RDD. For this purpose it is necessary multimedia rights and acts types to be associated with unambiguous links.

2. Additional RDD nudity type represented as REL rights - these are all further implement the acts type than those listed above, which also includes within the namespace.

3. RDD resource type (resource types) as REL resources (resources) - they are obtained using a new generation of complex XML types, which are the heirs of an abstract resource type (resource).

4. RDD context type (context types) as REL conditions (conditions) - they are obtained using a new generation of complex XML types, which are the successors of the abstract type of condition (condition).

In order to synchronize the process of introduction of terms defining the rights whose existence and provision ensures smooth implementation of actions on multimedia products by consumers is developed and a regulatory scheme to support RDD. It is called control (management) model RDD (Fig. 2).

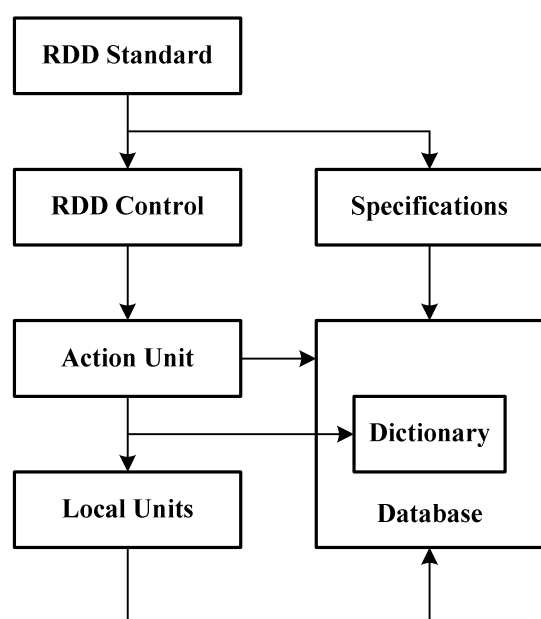


Figure 2. RDD Control Model

On the basis of this model it is created and called RDD system whose components are three:

1. The specifications defined by the standard RDD.

2. Dictionary composed of terms and their attributes, in accordance with the specification.

3. Database - the means by which the dictionary is stored.

This system will help a lot for reliable processing and exchange of information between all stakeholders in the management of rights over multimedia resources.

The process of registering a new term or terms set begins with filing an application to the governing body of the registration authority, which in turn provides samples of the applicant. The idea is for this process to be carried out electronically with the maximum degree of automation against errors of subjective factors. Management unit in turn appoint a new registration procedure for assigning identifier for the proposed new term that is included in the database. This is done in accordance with all established at RDD standard rules, which are the most senior in a hierarchical relationship in the system (Fig. 2). Executive departments, along with local ones, some of which may be set up temporarily when necessary, are assigned structured sequence and duration tasks related to the verification of the compatibility of the newly proposed terms. Another is their duty continuous maintenance of the database with already accepted terms and providing access to it for the purpose of authorized bodies or persons.

This completes the applicability of part 6 of the MPEG-21. The complete specification of RDD standard is given in [7], a full XML schemas for basic types-parents, referred to the above model - in [6].

4. DIGITAL ITEM ADAPTATION

Part 7 of the MPEG-21 is designed to describe a set of tools which enable the adaptation of digital objects to specific conditions of their use by consumers. For a description of these funds are used exclusively normative XML descriptions, descriptions of the semantics of each component of the given vehicle, as well as purely informative examples of their use.

The purpose of the item Terminals and Networks, described in ISO/IEC 21000-1 as part of a 7-element model of the interaction between users is to

enable transparent access to the latest multimedia resources and protect them from any procedures for installation and setup of network components and terminals. Achieving this goal is possible with the introduction of DIA. Key elements of this model are the module to adapt the resource (resource adaptation engine), the module to adapt the description (description adaptation engine), integrated into a single module to adapt the digital objects. The result of processing is adapted to digital object (adapted digital item) while this treatment been used, DIA (DIA Tools), are the basic subject to standardization.

We note that both modules of Fig. 3 themselves are not subject to standardization within the meaning of Part 7 of MPEG-21.

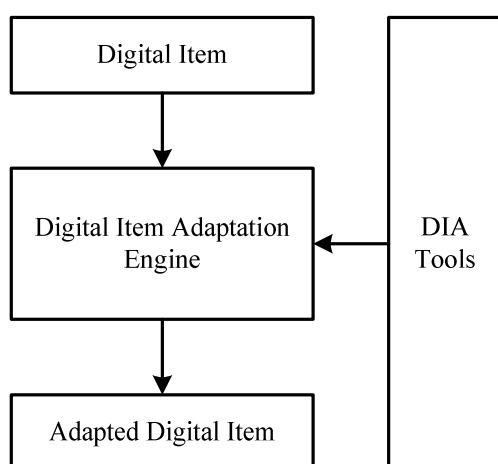


Figure 3. Digital Item Adaptation

These descriptions and mechanisms that are format (in terms of file or other structured records) in independent processing resource within the digital object can be regarded as an external set of tools (DIA Tools) and that they are standardized here. Specific application on specific platform (operating system), communication protocols, etc. are not subject to consideration.

DIA resources are divided mainly into three groups. The division is mainly by functional status.

The first group is a means to describe the environment of use (Usage Environment Description Tools), which include customized features, capacity of terminals, network characteristics and conditions of the surrounding environment in the broadest sense. These characteristics directly affect the ways of transmission, storage and processing of multimedia resources, mainly from actions which are under their physical media.

The second group is the means of adapting the resources of digital objects (Digital Item Resource Adaptation Tools). These agents directly affect the structure and management of resources of digital objects. When using bit-stream syntax description of these tools one can control the transmission speed of the transport flow. This method is particularly suitable for the exchange of resources, stored in the network nodes (nodes abutment), which load can vary widely depending on the needs of the consumers. Another important tool, found a place in this group is what controls the quality of the service(s) on a network terminal (Terminal and Network QoS (Quality of Service)). Third means of this group provides the adaptability of metadata (Metadata Adaptability) filtering and scaling official information flows based on simplified XML frameworks (templates) for a description.

The third and final group is the means of adapting the reporting of digital objects. They demonstrate the overall adaptation of the structure completed on digital objects, not just the resources that are part of them. One means of providing mobility session, expressed in the possibility of redirecting the flow of information from one terminal to another without impairing quality of reception and keeping the overall structure of the otherwise complex digital objects. Elections within a digital object can be changed by using the tool to configure preferences for the declaration of the digital object (DID Configuration Preferences) and then, depending on the intentions and preferences (preferences) to the user. And with reports of a profile adaptation of digital objects (DIA Description Messages) providing conditions for registration, transfer, update and delete DIA descriptions.

The fundamental unit of distribution and supply in terms of MPEG-21 is a digital object. While individual parts of this standard deal with different aspects of this fundamental unit, the connection between all of them forms a complete multimedia framework. It rationalization and realization of this relationship is crucial to reach a workable system for MPEG-21.

Part 2 of ISO / IEC 21000 (DID) provides a wrapper of all other parts of this standard. One of the input parameters for the module performing the adaptation of digital objects is meaningful digital object (Content Digital Item - CDI), which is a special case of a digital object, which necessarily incorporates a few resources, respectively. With DII this object is identified by content (ISO / IEC 21000-3). Possible,

but not necessarily it contains elements defined in other parts of the standard - 4, 5 or 6 in any combination, but to perform DIA, it must be carrier of the required funds set according to Fig. 4.

Digital Item Adaptation Tools	Usage Environment Description Tools
	Digital Item Resource Adaptation Tools
	Digital Item Declaration Adaptation Tools

Figure 4. Digital Item Adaptation Tools Organization

This is not necessarily because the model to perform DIA is provided and the possibility that these funds are part of contextual digital object (Context Digital Item - XDI). This type of objects does not carry any resources, but they are carriers of multimedia metadata framework themselves. Thus XDI is a catalyst in the process of adaptation as a second input to the module, carrying out adaptation. They are also subject to identification (DII) before being used. Thus a possibility is provided to adapt and to receive digital object as an output from the DIA with a changed DID identifiers, IPMP / REL elements, DIA elements, and resources. The complete specification of Part 7 of MPEG-21 is given in [8].

5. CONCLUSION

In this paper a new methodical approach is suggested for personal data protection based on the existing and widely spread MPEG-21 schemas for intellectual property rights management extended to medical information obtained during the process of patient rehabilitation. It is addressed towards a currently developed medical assistive system for motor disabled users whose results from undertaking prescribed exercises must be protected from unauthorized access. It is considered that the proposed methodology is applicable to wider range of medical systems yet to be amended.

6. ACKNOWLEDGMENTS

This work was supported by the National Scientific Fund at the Ministry of Education and Science, Republic of Bulgaria, within the project DFNI I02/1 "Intelligent man-machine interface for assistive medical systems in improving the independent living of motor disabled users".

References

- [1] I. Draganov, N. Neshov, D. Brodić, Testing Oculus Rift Virtual Reality Headset Applicability to Medical Assistive Systems, Proc. of ICEST'2015, June 24-26, Sofia, Bulgaria, pp. 54-57, 2015.
- [2] ISO/IEC TR 21000-1:2001, Information Technology – Multimedia Framework – Vision, Technologies and Strategy, N4333.
- [3] ISO/IEC IS 21000-2:2002, Information Technology – Multimedia Framework – Digital Item Declaration, N3971.
- [4] ISO/IEC CD 21000-3:2001, Information Technology – Multimedia Framework - Digital Item Identification and Description, N4532.
- [5] ISO/IEC CD 21000-4:2001, Information Technology – Multimedia Framework - Intellectual Property Management and Protection, N4269.
- [6] ISO/IEC CD 21000-5:2002, Information Technology – Multimedia Framework - Rights Expression Language, N4942.
- [7] ISO/IEC CD 21000-6:2002, Information Technology – Multimedia Framework - Rights Data Dictionary, N4943.
- [8] ISO/IEC CD 21000-7:2002, Information Technology – Multimedia Framework - Digital Item Adaptation, N5353.

AN APPROACH TO ESTABLISHING MODELS FOR THE EMF EMISSION OF THE LAPTOPS BY ANN

Darko Brodić, Dejan Tanikić, Milena Jevtić

University of Belgrade, Technical Faculty in Bor
Vojske Jugoslavije 12, 19210 Bor, Serbia
e-mail: dbrodic@tf.bor.ac.rs, dtanikic@tf.bor.ac.rs, mjevtic@tf.bor.ac.rs

Ivo R. Draganov

Laboratory of Audio and Video Technologies
Radiocommunications and Videotechnologies Dept.
Faculty of Telecommunications, Technical University of Sofia
8 Kliment Ohridski Blvd., 1756 Sofia, Bulgaria

Abstract

The paper describes the measurement of the electromagnetic field around laptops. According to obtained results, we propose an approach to model magnetic field emission of the laptop. As an input element, we use vector of three known laptop characteristics. The output represents the magnetic field emission of the laptop. At the end, the proposed model obtained by ANN is validated on the real measured magnetic field values. The linearity between measured and predicted values proves the correctness of the proposed approach.

1. INTRODUCTION

Today, in most houses and work places in the modern world you can find at least one personal computer (PC). All computers emit low frequency magnetic radiation from all electric parts they are built-in. A laptop is a compact portable PC, usually battery-powered, which is small enough to carry it as well as to use it on the user's lap. This means that they are often used at close contact with the body, i.e. to the skin, bones, blood, genitals, and, in pregnant women, close to the fetus. All aforementioned circumstances are very dangerous to the users health [1]. The laptop emits extremely low frequency (ELF) magnetic field from the processors, cooler, electrical chips on motherboard and hard disc all the time it is working. If you put your laptop on a table you will reduce your exposure from ELF magnetic field at the bottom part of laptop to very low levels. Due to dangerous use of laptop in certain circumstances, it is an obstacle to predict magnetic field emission around laptop. The problem of modeling the laptop magnetic field emission to a very best of the authors knowledge hasn't been considered yet. Hence, some studies about this topic can be of great interest to professionals and scientists. In this paper, we try to establish a simple, but yet functional model giving the level of magnetic field emission in according to some laptop characteristics. This approach is based on three inputs vector representing laptop characteristics and one

output representing magnetic field emission of the laptop in the office environment, i.e. at the top positions of the keyboard. These measuring positions are very important, because the laptop users are in close contact with the keyboard and touchpad all the time.

The paper is made in the following manner. Section 2 describes the magnetic field basics. Section 3 gives the measuring device characteristics and proposes the measuring positions at the laptop body. Section 4 presents the magnetic field measuring results. Section 5 proposes the ANN model according to the magnetic field measuring results. Section 6 makes conclusions.

2. MAGNETIC FIELD

The magnetic field is induced as a consequence of the current that flows through the electronic components of the laptop. The laptop users are exposed to a uniform magnetic field (in the neighborhood of the magnetic field emitter), which means that the time dependence of the field is the same in all points of the exposed subjects (laptop users) [2]. The magnetic induction \mathbf{B} as a vector is characterized with its direction and magnitude. The direction of \mathbf{B} can be decomposed into the three-unit directional vectors, which are parallel to each one giving its direction along the x , y , and z axis. The magnitude of \mathbf{B} can be decomposed into the scalar components B_x , B_y and B_z , which are measured in the

direction of the x , y , and z axis. Hence, \mathbf{B} can be represented as follows:

$$\mathbf{B} = B_x \cdot \hat{x} + B_y \cdot \hat{y} + B_z \cdot \hat{z}. \quad (1)$$

where \hat{r} is a unit vector in the direction of r decomposed into the unit directional vectors along the x , y , and z axis.

The devices usually measure the root mean square value of the magnetic field induction $|\mathbf{B}|$, which is calculated using its scalar components B_x , B_y and B_z :

$$|\mathbf{B}| = \sqrt{(B_x^2 + B_y^2 + B_z^2)}. \quad (2)$$

3. MEASUREMENT

The measurements were performed in the office where the influence of the magnetic field is negligible, i.e. it is lower than $0.01 \mu\text{T}$. EMF measurement was performed by Lutron EMF 828 device. It measures the magnetic induction from $0.01 \mu\text{T}$ to 2 mT , which frequency range is between 30 and 300 Hz . The EMF 828 has three measurement extents: $20 \mu\text{T}$, $200 \mu\text{T}$ and $2000 \mu\text{T}$. The precision of the measurement heavily depends on the measurement extent. Consequently, it is of the order $0.01 \mu\text{T}$ for the measurement extent of $20 \mu\text{T}$, $0.1 \mu\text{T}$ for $200 \mu\text{T}$ and $1 \mu\text{T}$ for $2000 \mu\text{T}$, respectively. Lutron EMF 828 measures all three components of the magnetic induction B , i.e. B_x , B_y and B_z . Accordingly, it measures root mean square (RMS) in the ELF magnetic field frequency given in eq. (2).

The measurement of magnetic field is usually performed by an EMF measuring device in the positions where the influence of the external magnetic field is negligible. It means that the level of the magnetic field has to be lower or equal to $0.01 \mu\text{T}$ [2]. In this study, we explore the magnetic field emitted by the laptop in the office environment. Up to now, the magnetic field measurement positions have been proposed in literature. The TCO standard proposed the positions where the laptop users are not in close contact with the laptop body. Hence, it is irrelevant to the laptop users [3]. Furthermore, ref. [4] proposes one measurement position in the middle of the keyboard and others 10 cm and 20 cm below the laptop and 10 cm up of the keyboard center and at the screen position. This approach is superfluous too. Except the position in the middle of the keyboard, all other positions are completely unsuitable. It is valid because the

screen has negligible magnetic field emission. Furthermore, 10 and 20 cm away from the center point of emission is too far away to register significant amount of magnetic field emission, especially when the laptop is used at the desk. Due to the laptop construction, different level of the magnetic field is present in different parts of the keyboard/touchpad area. Hence, this area should be divided into different measuring areas. In this study we use the approach which is proposed in [5]. It takes into account nine positions at the top of the laptop body, i.e. at the top of the keyboard. Figure 1 shows typical measuring position at the top of the laptop (office condition when laptop is operating on the office table).

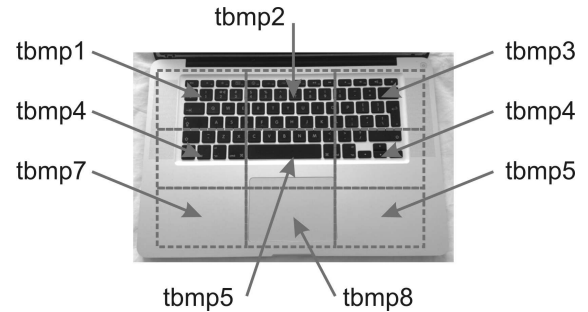


Figure 1. Nine measuring positions at the top of the keyboard

From Figure 1, the measuring points are marked as tbmp1-tbmp9. The measuring method is evaluated on 10 laptops of different typology and screen size: $17''$, $15.6''$, $14''$, $13.3''$ and $11.6''$. Measures have been collected when laptops were supplied by alternating current (AC) in the office environment.

4. RESULTS

The measurement results of the magnetic field B obtained at the top body measurement points in normal operating condition of the laptop are given in Table 1.

The minimum values of the measured magnetic field B obtained at the measuring points tbmp1-tbmp9 are between 0.0000 and $0.0548 \mu\text{T}$. Furthermore, the maximum values of the magnetic field B are between 0.5819 and $2.2011 \mu\text{T}$. At the end, the average values of the magnetic field B are from 0.1219 to $0.5468 \mu\text{T}$.

5. ANN MODELING

Using into the consideration the level of the ELF magnetic field emission from the laptops, it is pos-

sible to design an artificial neural network (ANN) in order to predict the intensity of the magnetic field at the measured (top body) positions of the laptop. The neural network is mapping between a data set of numeric inputs and outputs, i.e. targets. We explore the results obtained by measuring magnetic field emission around 10 different portable computers in normal office operation condition. The measurement positions are at the top part of the laptop. Each area above the laptop was divided into nine regions such as: (i) upper left, (ii) upper central, (iii) upper right, (iv) medial left, (v) medial central, (vi) medial right, (vii) lower left, (viii) lower central and

(ix) lower right. Collected data was pre-processed beforehand, and the total amount of 90 measured values was used in the ANN training phase. There are many physical parameters that can affect the intensity of the magnetic field. The most important of them are: (i) Passmark, which represents the one of the known processor calculation power estimation values, (ii) CPU total dissipation (CPU TD), i.e. processor dissipation in W, and (iii) laptop maximum power consumption (Laptop MPC), i.e. the total power consumption of the laptop in W.

Table 1. The measured magnetic field B at the top part of laptops in normal operating condition

Laptop	1	2	3	4	5	6	7	8	9	10
Minimum	0.0100	0.0141	0.0000	0.0173	0.0000	0.0548	0.0224	0.0173	0.0374	0.0316
Maximum	0.5819	1.7686	0.6138	2.2011	1.3743	1.8958	1.5069	4.2164	1.6739	1.4279
Average	0.1219	0.4805	0.1714	0.3709	0.4243	0.5468	0.2685	0.5475	0.3615	0.5323

Table 2. The laptop characteristics used for magnetic field prediction by ANN

Laptop	1	2	3	4	5	6	7	8	9	10
CPU Passmark	2327	2327	1687	2113	1911	7493	961	795	1477	2646
CPU TD (W)	17	17	25	35	35	45	17	31	25	35
Laptop MPC (W)	45	45	65	90	90	120	33	60	75	80

Table 3. The correlation coefficient R of the various neural network architectures

Number of hidden layer neurons	5 neurons	9 neurons	10 neurons
Correlation coefficient – R	0,946	0,874	0,915

Table 2 shows aforementioned laptop characteristics used to predict a magnetic field by ANN.

Accordingly, each input is given as a 3-element vector. The values of this vector are normalized to be used as input parameters. This process ensures that each input parameter will be in the range [0, 1].

Training and testing data sets were used for training and testing of the various ANN architectures. The number of nodes X in the hidden layer was varied from 5 to 10 neurons. The percentage of data used for training, testing and validating was varied.

The accuracy of the ANN model is performed by means of statistical parameters such as correlation coefficient. The correlation coefficient R is a statistical measure of the strength of correlation between the predicted and measured values. The correlation

coefficients of the various ANN architectures are given in Table 3.

All of the used ANN architectures have relatively good fitting capabilities. Essentially, increasing the number of neurons in the hidden layer of the ANN didn't achieve the expected increasing in the value of the correlation coefficient R . Consequently, all architectures have relatively uniform values of the correlation coefficients R . Hence, there is no need for using robust neural network, which is memory and computer time consuming. Accordingly, ANN with 5 neurons in hidden level has satisfactory accuracy with the correlation coefficient equal to 0.946. The predicted values, along with the measured values of the ANN with 5 neurons in the hidden layer are shown in Figure 2.

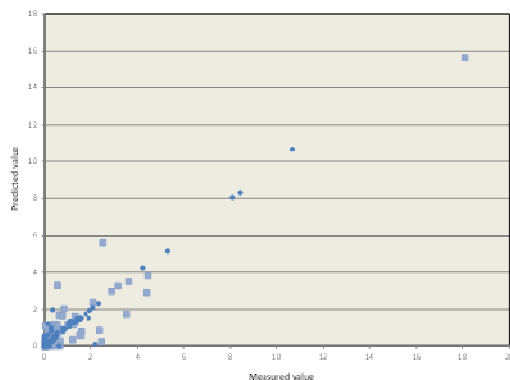


Figure 2. Measured vs. ANN predicted magnetic field values

The linearity of the given graph shows that the proposed ANN model predicts magnetic field values very good. Furthermore, it proves that our premise about important laptop characteristics that influence the output representing magnetic field is valid. This approach can be used for other measurements of the magnetic field emission around laptop.

6. CONCLUSION

The paper addressed the problem related to the ELF magnetic field emission produced by laptops. The measurement of the magnetic field was carried out by Lutron EMF 828. The obtained results showed that the laptop characteristics like power consumption and dissipation as well as laptop processor calculation capabilities have a tremendous impact on the level of the magnetic field emission. It was proved by modelling laptop magnetic field emission with ANN.

Further research direction will be toward establishing the unique ANN based model for prediction of magnetic field emission around all parts of the laptop.

7. ACKNOWLEDGMENTS

This work was partly supported by the Ministry of Education, Science and Technological Development of the Republic of Serbia TR33037 and 33046.

References

- [1] International Agency for Research on Cancer (IARC) (2002). Monographs on the Evaluation of Carcinogenic Risks to Humans, Vol. 80, Non-Ionizing Radiation, Part 1: Static and Extremely Low-Frequency (ELF) Electric and Magnetic Fields. Lyon, France: IARC Press.
- [2] Bellieni, C. V., Pinto, I., Bogi, A., Zoppetti, N., Andreuccetti, D., Buonocore, G. (2012). Exposure to electromagnetic fields from laptop use of "laptop" computers. Archives of the Environmental and Occupational Health, 67 (1), 31-36.
- [3] W. Hayt, J. Buck (2012). Engineering Electromagnetics. 8th ed. Ed. McGraw-Hill. New York, USA. pp. 1-25.
- [4] [3] TCO'05 standard (2012). <http://tcodevelopment.com/files/2013/04/TCO-Certified-Notebooks-4.0.pdf>
- [5] Maluckov, B. S., Tasić, V., Mladenović, S., Maluckov, Č. A. (2014). The magnetic field from laptop computers. In Proceedings of XXII International conference Ecological Truth, ECO-IST'14, Bor, pp. 531-535.
- [6] Brodic, D., Amelio, A. (2015). Classification of the Extremely Low Frequency Magnetic Field Radiation Measurement from the Laptop Computers. Measurement Science Review, 15 (4), 202-209.

DESPECKLING OF MEDICAL ULTRASOUND IMAGES BASED ON WAVELET DECOMPOSITION

Veska M. Georgieva

Faculty of Telecommunications, Technical University of Sofia, Bulgaria
1000 Sofia, "Kl. Ohridsky" str.8
T. (+359 2) 965-3293; E-mail: vesg@tu-sofia.bg

Stephan G. Vassilev

Faculty of German Engineering Education and Industrial Management, Technical University of Sofia, Bulgaria
1000 Sofia, "Kl. Ohridsky" str.8
E-mail: stephan.vassilev@gmail.com

Abstract

In the paper is presented a new wavelet -packet domain technique for despeckling of medical ultrasound (US) images for improved clinical diagnosis. For modelling an image with speckle noise is used the generalized Gaussian distribution and generalized gamma distribution. For noise reduction is used modified homomorphic filter based on wavelet packet decomposition of the transformed US image.

Some experimental results are presented, obtained by computer simulation in the MATLAB environment. Implementation results are given to demonstrate the visual quality by suppressing of the speckle noise and preserving the organ surfaces with application in clinical diagnosis.

1. INTRODUCTION

Due to its non-invasive nature and easily portable devices, ultrasound imaging is nowadays used for the diagnostic and clinical studies of many diseases. The quality of US images is very important by detection of some pathological modifications in a body structures and tissues.

Speckle is a type of noise which generally masks the fine details of the US image, thereby making the interpretation of an US image difficult for medical diagnosis. Speckle noise is presented as the random mottling of the image with dark and bright spots which hides certain details [1]. As a result, despeckling methods are necessary to enhance the image quality and increase the diagnostic value of medical US images. In [2] is demonstrated that the speckle is signal-dependent in the sense that the mean is proportional to the standard deviation of the speckled image. The multiplicative nature of the speckle was proposed in [3] where the multiplicative noise is converted to an additive one through log transformation and the problem of despeckling is thus reduced to the estimation of signal in the presence of additive noise. Wiener filtering can be used in order to reject the additive noise, followed by an exponential transformation. This algorithm is general because it allows further modification by replacing the linear Wiener filter with other filtering sche-

mes. The application of the wavelet transform for despeckling of medical US images was reported in [4]. These methods use logarithmic transformation of the speckled image before wavelet denoising. After the log transform, the speckle can be approximated by zero-mean additive white Gaussian noise, and estimators/filters are designed accordingly. The methods are referred to as the homomorphic wavelet based despeckling (HWDS) methods. The most studies show that despeckling of an US image is major research problem and the performance of HWDS schemes may be improved by an accurate analysis of the statistical properties of the log-transformed speckle noise. In [5] is proposed to model the speckle in the detailed wavelet sub-bands of log-transformed US images by the generalized gamma distribution (GGAD) and use the model for despeckling in the Bayesian framework and the noise is removed in Discret Wavelet Transform (DWT) domain.

This paper proposes to use a similar model an image with speckle noise based on the generalized Gaussian distribution and generalized gamma distribution. We use for noise reduction a modified homomorphic filter based on wavelet packet decomposition and adaptive threshold of the transformed US image.

The paper is arranged as follows: In Section 2 is described the speckled image model; In Section 3 is presented the main algorithm of processing; in Section 3 are given some experimental results, obtained by computer simulation and their interpretation; in Section 4 - the Conclusion.

2. SPECKLED IMAGE MODEL

It is defined that the fully-developed speckle is a multiplicative noise and can be modeled as:

$$I(x, y) = g(x, y)n(x, y), \quad (1)$$

where, I and g are the observed noisy image and noise-free image, respectively, n is the noise variable modeled as a stationary unity means random variable independent of g . The homomorphic despeckling methods take the advantage of the logarithmic transformation that, when applied to both sides of Eq.(1), converts the multiplicative noise into an additive one:

$$\ln I(x, y) = \ln g(x, y) + \ln n(x, y) \quad (2)$$

The wavelet transform now becomes a linear operation. In this case the application of the WPT to the noisy image $\ln I(x, y)$ gives:

$$W[\ln I(x, y)] = W[\ln g(x, y)] + W[\ln n(x, y)] \quad (3)$$

where W is the WPT operator. So the Eq. (3) can be rewritten as:

$$Y = X + N \quad (4)$$

where, Y , X , and N are the random variables representing wavelet coefficients, respectively, of the noisy data, noise-free data, and the noise in Equation (2).

For most of images, the signal components in the detail sub-bands after wavelet decompositions have heavier tails and are sharply peaked at zero. They are described by the zero-mean generalized Gaussian distribution (GGD). Some limiting case of the GGD is the gamma distribution. We have used the generalized gamma model, which is more general than the Gaussian to approximate the speckle statistics in the sub-band representation of US images [5].

3. GENERAL ALGORITHM FOR SPECKLE NOISE REDUCTION OF US IMAGES

In this paragraph is presented the general algorithm, used to reduce speckle noise. Fig. 2 presents the block diagram of the proposed algorithm. For filtering stage is used a wavelet packet decomposition issued from a given orthogonal wavelets. As this number may be very large, it is interesting to find an optimal decomposition with respect to a conventional criterion. The classical entropy-based criterion is a common concept [6]. In obtained best shrinkage decomposition is used soft threshold on all highpass sub-bands to reduce the wavelet coefficients, regarding to chosen model of the speckle statistics in the sub-band representation of US images.

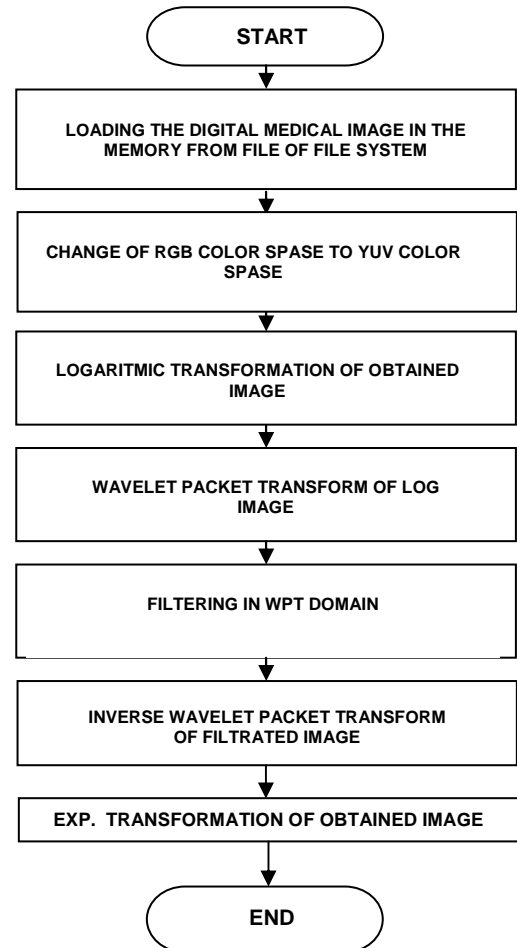


Figure 2. Block diagram of the General Algorithm for Despeckling of US Images

4. EXPERIMENTAL RESULTS

The formulated stages of processing are realized by computer simulation in MATLAB 7.14 environment by using IMAGE PROCESSING and WAVELET TOOLBOXES [7]. In analysis are used 20 US ima-

ges from kidney with size 640x480 pixels in jpg file format. For processing they are converted in bmp. format.

Some results from simulation, which illustrate the working of proposed algorithm, are presented in the next figures below.

In Fig. 2 is shown the original US abdominal image of right kidney.

The best shrinkage decomposition is obtained by Shannon entropy criterion on level 2. In Fig. 3 is presented this decomposition and the original image in node (0,0).

Fig. 4 presents the wavelet packet decomposition and the processed image after filtration in node (5,0).



Figure 2. Original US image of right kidney

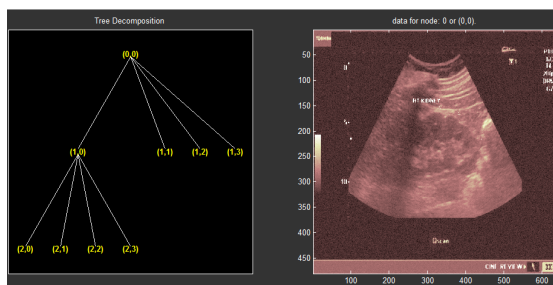


Figure 3. Wavelet decomposition and the original US image

The presented figure illustrates the visual enhancement of the processed images.

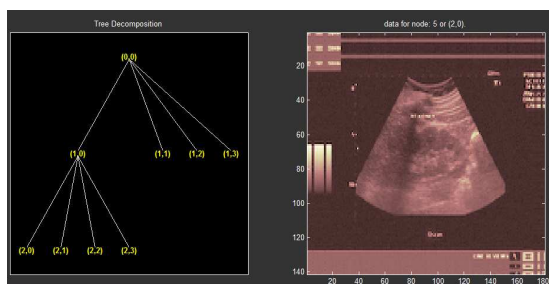


Figure 4. Wavelet decomposition and the processed US image

In Fig. 5 is shown the US image after speckle noise reduction.



Figure 5. US image of right kidney after speckle noise reduction

In the paper are analyzed some quantitative estimation parameters: Noise reduction ratio (NRR), Signal to noise ratio in the noised image (SNR_Y), Signal to noise ratio in the filtered image (SNR_F), Effectiveness of filtration (E_{FF}), Peak signal to noise ratio (PSNR). The obtained averaging results by calculation of some estimations parameters are presented in Table 1. They are compared with the parameters, obtained with the algorithm on the base of DWT.

Table 1. Simulations results

Method of processing	Estimations Parameters			
	PSNR [dB]	SNR_Y [dB]	SNR_F [dB]	E_{FF} [dB]
HM based on DWT	24.619	9.304	10.362	1.058
HM based on DWPT	27.327	9.304	11.224	1.920

The obtained result for noise reduction ratio (NRR) by the method of homomorphic filtering based on DWT is 0.502 and shows that the noise is reduced about two times. This parameter is better by our method of homomorphic filtering based on WPT and adaptive threshold. It is 0.221 and shows, that the noise is reduced about 5 times.

The presented results show that the proposed approach is more effective by speckle noise reduction in comparison with DWT.

5. CONCLUSION

In the paper is presented a new and effective approach for speckle noise reduction in US images. The implemented study and obtained results show

its advantage by applying of WPT in homomorphic filtering schema as DWT.

The proposed method can be used in a preprocessing stage for future segmentation of kidney or other organs, as well for future analysis and classification of diseases.

Our future work will be concentrated in effective enhancement techniques and methods for segmentation of kidney or other organs.

5. ACKNOWLEDGMENTS

The paper was supported by the PhD Students Research Project "Algorithms for US Image Segmentation based on Wavelet Transformation", NIS № 152 PD0019-07/2015.

References

- [1] O. V. Michailovich, A. Tannenbaum, Despeckling of Medical Ultrasound Images, *IEEE Transactions on Ultrasonics, Ferroelectronics and Frequency Control*, Vol. 53, no. 1, pp. 64-78, 2006.
- [2] J. S. Lee, Speckle analysis and smoothing of synthetic aperture radar images, *Comput. Graph. Image Processing*, Vol. 17, no. 1, pp. 24-32, 1981.
- [3] A. K. Jain, *Fundamentals of Digital Image Processing*, 3rd ed., Engle wood Cliffs, NJ: Prentice Hall; pp. 569, 1989.
- [4] S. Gupta, R. C. Chauhan, and S. C. Saxena, Homomorphic wavelet thresholding technique for denoising medical ultrasound images, *Taylor and Francis Int. J. Med. Eng. Technol.* Vol. 29, pp. 208-14, 2005.
- [5] B. Deka, P. Bora, Wavelet-based Despeckling of Medical Ultrasound Images, *IETE Journal of research*, Vol. 59, pp. 97-108, 2013.
- [6] V. Georgieva, Edge detection in US images using wavelet decomposition, *CEMA'10*, pp.108-111, 2010.
- [7] MATLAB User's Guide. Accessed at: www.mathwork.com

MODELING THE FLUID FLOW IN HUMAN INNER EAR

Svetlin Antonov

Technical University of Sofia
Faculty of Automatics, building 12, office 12502, 8 Kl. Ohridski Blvd, Sofia 1000, Bulgaria
T. +35929653367; E. svantonov@yahoo.com.

Abstract

A mathematical model is developed related to the work of the cochlea based on the turbulent fluid movement equations. This is concluded from the basic equation of fluid dynamics in stress using so called effective viscosity. A characteristic equation is made on the basis of the resulting equations, as well as its components. The most common model of turbulence is used- $k - \varepsilon$.

Key words: flows in biological processes, cochlea, turbulent motion, characteristic equation, model of turbulence

1. INTRODUCTION

When worked out the theoretical model is approached in a way that corresponds to the equations used in the program Fluent (Ansys). These equations differ from the usual used in Reynold's fluid mechanics equations [1]. The work out is made on the base of the main equation of the fluid mechanics in tensions [2]. Instead μ is replaced by μ_{eff} in processing equations (8). It is obtained a very convenient form of the system equations in a practical point of view. It is necessary to define some of the numbers [3] in the mentioned above equations of turbulence model and to replace them in the resulting system.

2. PHYSICAL DESCRIPTION OF THE FLOW IN COCHLEA

It is assumed that due to the impact of pounding the gavel on the oval window, arises an transient flow in cochlea tube which wraps the basilar membrane along its entire length, passes through the helicotrema to the bottom side, reaching the round window and back. Knowing that the cochlea fluid has the same properties as the water, it is easy to calculate the Reynolds number:

$$Re = \frac{ud}{\nu} \quad (1)$$

In the pressure Δp created on the surface of the oval window the liquid is driven at a speed $u \approx 0,77 m/s$. The diameter of the cochlea is taken approximately as $d = 0,003 m$; the viscosity of the liquid when the body temperature is

$t = [36,5 \div 37]^\circ C$ then $\nu = 0,77 \cdot 10^{-6} m^2/s$. In these parameters Re- number is obtained as $Re \approx 3078$. This gives grounds to assume turbulent nature of the flow. Since this value is close to the critical Reynolds's number ($Re_{critical} = 2320$) in the resolve will require consideration of viscous stresses. Reason for this is the presence of boundary layers on the walls of the cochlea and the basilar membrane in a very small range of $2,5 \div 3 mm$.

The flow is isothermal at a constant temperature or at slightly changing in the range from $t = 36,5 \div 40^\circ C$. In this situation, the density remains constant ($\rho = const$). The flow is a liquid which in particular at a constant temperature is an incompressible fluid.

When recording of differential equations of continuity and motion is adopted:

$$v_i = \frac{\mu_i}{\rho} \quad (2)$$

$$\nu = \frac{\mu}{\rho} \quad (3)$$

i.e. they will appear on the coefficients of the kinematic viscosity ν and hence turbulent viscosity ν_i .

3. MATHEMATICAL MODEL OF THE FLOW

The mathematical model of the flow is based on the equation of continuity and the dynamics of fluids in tensions. In vector form they can be presented as [2]:

$$\text{div} \vec{V} = 0 \quad (4)$$

$$\begin{aligned} \rho \frac{d\vec{V}}{dt} + \rho (\vec{V} \cdot \nabla) \vec{V} = \\ = \rho \vec{F} + \frac{\partial \vec{p}_x}{\partial x} + \frac{\partial \vec{p}_y}{\partial y} + \frac{\partial \vec{p}_z}{\partial z} \end{aligned} \quad (5)$$

where $\vec{V} = u\vec{i} + v\vec{j} + w\vec{k}$ is 3 dimensional flow velocity; u, v, w are components of the velocity by x, y, z ; $\vec{F} = X\vec{i} + Y\vec{j} + Z\vec{k}$ is the intensity of the field of mass force and its relevant components along the axes; $\vec{p}_x, \vec{p}_y, \vec{p}_z$ are internal tensions in

the three axes; $\vec{\nabla} = \frac{\partial}{\partial x} \vec{i} + \frac{\partial}{\partial y} \vec{j} + \frac{\partial}{\partial z} \vec{k}$ is Hamilton operator.

According to summarized Newton's law is considered the relation between the tensor of the internal tension P and deformation speed S .

$$P = aS + b \quad (6)$$

At the conclusion of the equations in the case of turbulent flow is assumed:

$$a = 2\mu_{eff} \quad (7)$$

$$\mu_{eff} = \mu + \mu_t \quad (8)$$

Thus determined tensor unit a difference with the usual Navier-Stokes' equations.

By using (7) and (8) for tangential and normal strains of turbulent flow of incompressible fluid is obtained:

$$\begin{aligned} \tau_{yx} = \tau_{xy} &= (\mu + \mu_t) \left(\frac{\partial u}{\partial y} + \frac{\partial v}{\partial x} \right) \\ \tau_{zx} = \tau_{xz} &= (\mu + \mu_t) \left(\frac{\partial u}{\partial z} + \frac{\partial w}{\partial x} \right) \\ \tau_{yz} = \tau_{zy} &= (\mu + \mu_t) \left(\frac{\partial v}{\partial z} + \frac{\partial w}{\partial y} \right) \\ \delta_x &= -p + 2(\mu + \mu_t) \frac{\partial u}{\partial x} \\ \delta_y &= -p + 2(\mu + \mu_t) \frac{\partial v}{\partial y} \\ \delta_z &= -p + 2(\mu + \mu_t) \frac{\partial w}{\partial z} \end{aligned} \quad (9)$$

After substituting (9) into (5) developed in scalar type by the respective axes is obtained as follows:

$$\begin{aligned} \frac{\partial u}{\partial t} + u \frac{\partial u}{\partial x} + v \frac{\partial u}{\partial y} + w \frac{\partial u}{\partial z} = \\ = -\frac{1}{\rho} \frac{\partial p}{\partial x} + 2 \frac{\partial}{\partial x} \left[(v + v_t) \frac{\partial u}{\partial x} \right] + \\ + \frac{\partial}{\partial y} \left[(v + v_t) \left(\frac{\partial u}{\partial y} + \frac{\partial v}{\partial x} \right) \right] + \\ + \frac{\partial}{\partial z} \left[(v + v_t) \left(\frac{\partial u}{\partial z} + \frac{\partial w}{\partial x} \right) \right] \end{aligned} \quad (10)$$

$$\begin{aligned} \frac{\partial v}{\partial t} + u \frac{\partial v}{\partial x} + v \frac{\partial v}{\partial y} + w \frac{\partial v}{\partial z} = \\ = -\frac{1}{\rho} \frac{\partial p}{\partial y} + 2 \frac{\partial}{\partial y} \left[(v + v_t) \frac{\partial v}{\partial y} \right] + \\ + \frac{\partial}{\partial x} \left[(v + v_t) \left(\frac{\partial u}{\partial y} + \frac{\partial v}{\partial x} \right) \right] + \\ + \frac{\partial}{\partial z} \left[(v + v_t) \left(\frac{\partial v}{\partial z} + \frac{\partial w}{\partial y} \right) \right] \end{aligned} \quad (11)$$

$$\begin{aligned} \frac{\partial w}{\partial t} + u \frac{\partial w}{\partial x} + v \frac{\partial w}{\partial y} + w \frac{\partial w}{\partial z} = \\ = -\frac{1}{\rho} \frac{\partial p}{\partial z} + 2 \frac{\partial}{\partial z} \left[(v + v_t) \frac{\partial w}{\partial z} \right] + \\ + \frac{\partial}{\partial x} \left[(v + v_t) \left(\frac{\partial u}{\partial z} + \frac{\partial w}{\partial x} \right) \right] + \\ + \frac{\partial}{\partial y} \left[(v + v_t) \left(\frac{\partial v}{\partial z} + \frac{\partial w}{\partial y} \right) \right] \end{aligned} \quad (12)$$

Accordingly continuity equation:

$$\frac{\partial u}{\partial x} + \frac{\partial v}{\partial y} + \frac{\partial w}{\partial z} = 0 \quad (13)$$

4. CHARACTERISTIC EQUATION

The problem is reduced to solving a 3 dimensional unsteady flow of a incompressible turbulent fluid. These equations ((10) - (13)) can be reduced to the characteristic equation:

$$\frac{\partial \Phi}{\partial t} + \text{div}(V\Phi) = \text{div}(\Gamma \text{grad} \Phi) + S \quad (14)$$

where: Φ is the relevant dependent variable; V accepted values u, v, w ; Γ is diffusion coefficient; S is source article on relevant Φ . Values of Φ, V, Γ, S are given in Table 1.

The solution of (14) leads to the determination of the values of the three components u, v, w of the velocity and the pressure p in 3-dimensional unsteady flow over incompressible fluid. For this solving, it is necessary to determine the coefficient of kinematic turbulent viscosity ν_t . Fluent software have brought several models of turbulence, which allow the determination of: a modification of $k-\varepsilon, k-\Omega$ and models based on Reynolds tensions. In solving the problem is using a $k-\varepsilon$ model where:

$$\nu_t = c\mu \frac{k^2}{\varepsilon} \quad (15)$$

where K is turbulent kinetic energy

$$\left(k = \frac{1}{2} (\bar{u}'^2 + \bar{v}'^2 + \bar{w}'^2) \right); \varepsilon \text{ is the speed of dis-}$$

sipation. Equations about k and ε have the expression:

$$\begin{aligned} \frac{\partial}{\partial t}(\rho k) + \frac{\partial}{\partial x}(\rho k u) = \\ = \frac{\partial}{\partial y} \left[\left(\mu + \frac{\mu_t}{\sigma_k} \right) \frac{\partial k}{\partial y} \right] + \\ + G_k + G_b - \rho \varepsilon - Y_M + S_K \end{aligned} \quad (16)$$

$$\begin{aligned} \frac{\partial}{\partial t}(\rho \varepsilon) + \frac{\partial}{\partial x}(\rho \varepsilon u) = \\ = \frac{\partial}{\partial y} \left[\left(\mu + \frac{\mu_t}{\sigma_k} \right) \frac{\partial \varepsilon}{\partial y} \right] + \\ + C_{1\varepsilon} \frac{\varepsilon}{k} (G_k + C_{3\varepsilon} G_b) - C_{2\varepsilon} \rho \frac{\varepsilon^2}{k} + S_\varepsilon \end{aligned} \quad (17)$$

The constants of the equations above are given in Table 2 [4], [5].

Because the flow is isothermal, and the fluid is incompressible $G_B = 0$ and $Y_M = 0$. The article G_K defines the generation of energy due to the interaction of Reynolds tensions and the gradient of the average speed is defined as:

$$G_K = -\overline{u'v'} \frac{\partial v}{\partial x} \quad (18)$$

According to the Boussinesq approximation can determine:

$$G_K = \nu_t S^2 \quad (19)$$

where S is the tensor of deformation speeds; the members S_K and S_ε are viscous dissipation.

Table 1. Coefficients the in characteristic equation

Φ	Γ	S
1	0	0
u	$v + \nu_t$	$\frac{\partial}{\partial x} \left(\Gamma \frac{\partial u}{\partial x} \right) + \frac{\partial}{\partial y} \left(\Gamma \frac{\partial v}{\partial x} \right) + \frac{\partial}{\partial z} \left(\Gamma \frac{\partial w}{\partial x} \right) - \frac{\partial p}{\partial x}$
v	$v + \nu_t$	$\frac{\partial}{\partial x} \left(\Gamma \frac{\partial u}{\partial y} \right) + \frac{\partial}{\partial y} \left(\Gamma \frac{\partial v}{\partial y} \right) + \frac{\partial}{\partial z} \left(\Gamma \frac{\partial w}{\partial y} \right) - \frac{\partial p}{\partial y}$
w	$v + \nu_t$	$\frac{\partial}{\partial x} \left(\Gamma \frac{\partial u}{\partial z} \right) + \frac{\partial}{\partial y} \left(\Gamma \frac{\partial v}{\partial z} \right) + \frac{\partial}{\partial z} \left(\Gamma \frac{\partial w}{\partial z} \right) - \frac{\partial p}{\partial z}$

Table 2. Constants of the equations about k and ε

$C_{1\varepsilon}$	$C_{2\varepsilon}$	$C_{3\varepsilon}$	C_μ	σ_k	σ_ε
1,44	1,92	0,8	0,09	1.0	1.3

5. CONCLUSION

It is worked out equations related to the unsteady turbulent incompressible fluid flow in human inner ear (cochlea). These equations are very close to the Navier-Stokes equations. They are very convenient for numerical solution of the problem as they allow selection of the most suitable model of turbulence. This paper presents the characteristic equation with its components and used later $k - \varepsilon$ model of turbulence. The approach is a novelty in resolving similar biomedical problems.

References

- [1] Antonov, R. Velichkova, S. Antonov, "Differential equations for turbulent flow", volume 53, University of Ruse "Angel Kanchev", Ruse, 2014, pp.119-123
- [2] L. Loycianski, Mechanics of liquids and gases, Nauka, Moskva, 1973
- [3] Chapter 10- Modeling turbulence, Fluent Inc., November 28, 2001
- [4] S. Patankar, Numerical heat transfer and fluid flow, McGrawHill Book company, New York, 1980
- [5] B. Spalding, "Older and newer approaches to the numerical modelling of turbulent combustion". Keynote address at 3rd International Conference on Computers in reciprocating engines and gas turbines, IMechE, London, 9-10 January, 1996

LOCATING THE AREAS OF ARISING OF NEW OUTBREAKS IN SPREADING FOREST FIRE THROUGH COMPUTER SIMULATION ALGORITHM

Svetlin Antonov

Technical University of Sofia
Faculty of Automatics, building 12, office 12502, 8 Kl. Ohridski Blvd, Sofia 1000, Bulgaria
T. +35929653367; E. svantonov@yahoo.com.

Abstract

Using computer modeling for simulation of the distribution of high temperature gas flow in the presence of wind is a possibility to determine the areas in which it is expected another outbreak of fire. The presented algorithm for computer simulation is built on a relatively quick solution integral method with accuracy allowing prognosis the development of fire setting. The algorithm is easy to learn and can run on any laptop configuration. It is necessary to input data for power of the fire and wind velocity. It allows to determine the maximum speed of the gas burning flow and its temperature.

Key words: forest fire, integral method, computer model, high temperature gas flow, ecology

1. INTRODUCTION

Forest fires have a large impact on nature (trees, grass and animals) and humans every year. Once arises of any source the fire can spread on a larger area from one part in the forest to the next trees and other objects (Figure 1). Some of the basic parameters in this process are the power of the fire and is there any wind. The wind velocity and its direction influence on the fire setting.

The fire is spread generally in the same direction as the wind direction with a level of speed depending on the wind velocity. In this paper some parameters like: geometry of the burning object; barriers as rivers, roads etc. are ignored.

The algorithm presents the steps of computing and understanding the deformation and raising gas burning flow over the fire. Some analyses of many experimental results are given in sources [1], [2], [3]. The mathematical model in this paper will be used as a base of the computer algorithm. It can be developed in Matlab environment [4].

2. MATHEMATICAL MODEL

For the purposes of calculating the parameters mentioned above the first step is to calculate the speed of the convective flow above the burning zone:

$$V_0 = 1,9Q^{0,2} \quad (1)$$

where Q is the power of the fire measured in kW.

Wind speed affects the axis of the upward flow over the fire and the length of the flow (Figure 2) is determined by:

$$l = \int_0^x \sqrt{1 + y'^2} dx \quad (2)$$

where x and y show the length of the trace (coordinates) in meters.

After transforming the equation (2) it can be presented as:

$$l = x\sqrt{1 + y'^2} \quad (3)$$

$$y'^2 = \frac{1}{Kx} \quad (4)$$

where K is a constant calculated for simplicity:

$$K = \frac{\rho_w Ww^2}{b_0 \rho_0 V_0^2} \quad (5)$$

where $b_0[m]$ is the width of the fire surface; $\rho_w = 1,2[kg / m^3]$ is the density of the wind; $\rho_0 = 0,4[kg / m^3]$ is the initial density of the flame; $T = 873[K]$ is the temperature of the fire; $Ww[m/s]$ is the wind velocity.

The damping of the maximal velocity by l is described by:

$$\overline{Um} = A_u n^{\frac{1}{2}} \left(\frac{l}{b_0} \right)^{-\frac{1}{2}} \quad (6)$$

$$n = \frac{\rho_w}{\rho_0} \quad (7)$$

$$Um = V_0 \overline{Um} \quad (8)$$

where $A_v = 2,48$ is an integral value after integration of the cross section.

The damping of the density of the gas flow along the length l is defined by:

$$\Delta \overline{\rho_m} = \frac{\Delta \rho_m}{\Delta \rho_0} = A_p n^{\frac{1}{2}} \left(\frac{l}{b_0} \right)^{-1} \quad (9)$$

$$\Delta \overline{\rho_m} = \frac{\rho_w - \rho_l}{\rho_w - \rho_0} \quad (10)$$

Then:

$$\rho_l = \rho_w - 0,8 \Delta \overline{\rho_m} \quad (11)$$

The calculations related to l start when $\rho_l > \rho_0$. In other case it is assumed that the temperature of the gas flow is a constant, i.e. the temperature is not reducing.

The temperature of the gas flow along the center line of the jet is obtained in Kelvins by:

$$T_l = \frac{P}{\rho_l R} \quad (12)$$

Where $p = 10^5 [Pa]$ is the atmospheric pressure; $R = 287$ is a gas constant.

The width of the gas flow over the fire is obtained by the equation:

$$b = b_0 + 0,22l \quad (13)$$

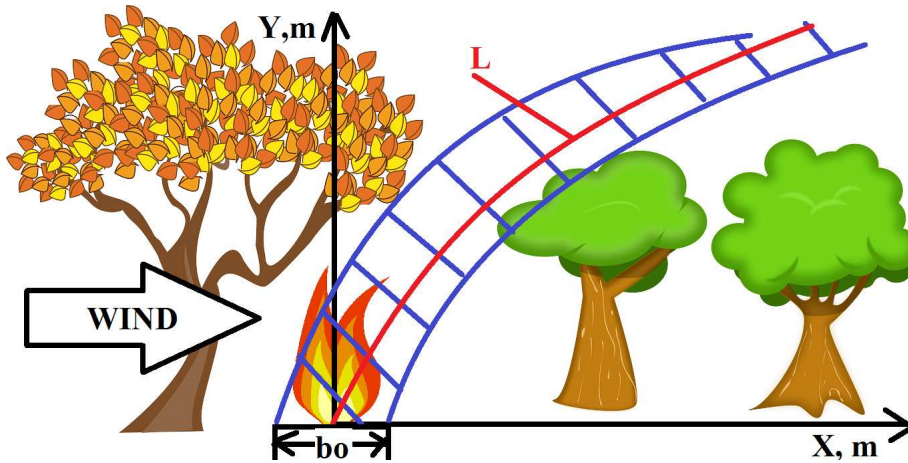


Figure 1. Forest fire scheme

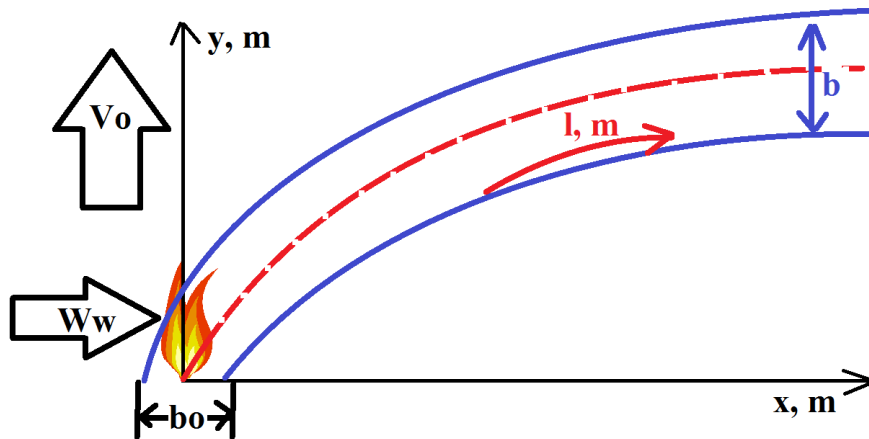


Figure 2. Forest fire calculated parameters

3. COMPUTER ALGORITHM

The mathematical model described above can be implemented in a computer system through developing an algorithm which is showed on Figure 3. This will give the possibility to use the model in emergency cases as fires in forest and to predict the gas burning flow position and its temperature. The initial data is listed as:

- ✓ the power of the fire in 3 cases-
 $Q1 = 400KW$, $Q2 = 600KW$,
 $Q3 = 800KW$;
- ✓ the distance from the fire source is
 $x \in [2, 20]m$;
- ✓ the wind velocity is $Ww1 = 2m/s$,
 $Ww2 = 4m/s$, $Ww2 = 6m/s$,
 $Ww2 = 8m/s$, $Ww2 = 10m/s$;
- ✓ $\rho_w = 1,2kg/m^3$;
- ✓ $T = 873K$;
- ✓ $\rho_0 = 0,4kg/m^3$;
- ✓ the atmospheric pressure $p = 10^5 Pa$;
- ✓ the gas constant is $R = 287J/kg^\circ K$.

For the purposes of this paper the above parameters are mentioned to show that the algorithm can use different input data and to calculate different combinations of initial data.

5. CONCLUSION

The proposed computer algorithm is very easy to learn and understand and then to implement it in any operational system and any laptop or a smart-phone. This is useful for the people when fighting the forest fires to predict the direction of the high temperature gas flow over the flame and the possible enlargement of the disaster.

The algorithm can be used to obtain and to transfer information for the fire setting in real time by an electronic device. The source code can be written in different environment such as Matlab, Java, C etc.

The automatic processing of the inputted data save time and allows saving human lives, animals and trees in forests. This is the main reason to renew the methods of planning and performing rescue and extinguishing activities.

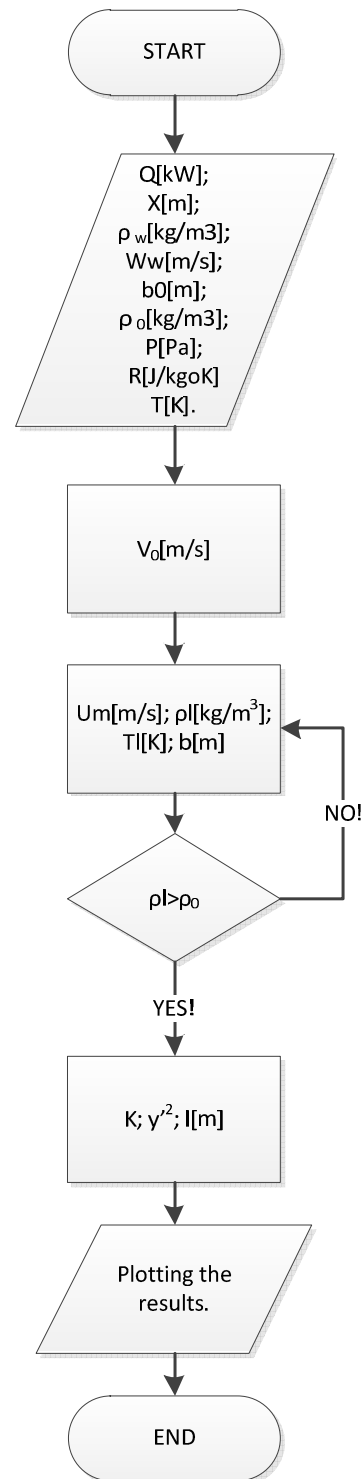


Figure 3. A simple computer algorithm

References

- [1] L. Elenkov, Forest fire dynamics, 2001, Sofia
- [2] <http://www.energyjustice.net/files/biomass/library/Carey-Schumann.pdf>
- [3] https://nature.berkeley.edu/moritzlab/docs/Cova_etal_2005.pdf
- [4] <http://www.mathworks.com/videos/programming-and-developing-algorithms-with-matlab-71067.html>

COMPOSITE LASER SPOT USE FOR HARD TISSUE PROBLEMS TREATMENT IN THE DENTAL MEDICINE – NEW TECHNOLOGY, ANALYSIS, APPARATUS AND TEST

Margarita Deneva¹, Stanislava Rabadgiiska¹, Nadejda Kaimakanova³, Valko Kazakov¹,
Pepa Uzunova², Marin Nenchev¹

¹ Technical University of Sofia, Plovdiv Branch and R&D Department QOEL Laboratory,
25 Tsanko Dystabanov St., 4000 Plovdiv

² Faculty of Stomatology – Medical University, Sofia

³ Plovdiv University "Paissii Hilendarski", Plovdiv

E-mail: mdeneva@yahoo.com, s1983@abv.bg, marnenchev@yahoo.com

Abstract

We develop and present here important details of proposed by us principle for improvement of enamel caries treatment using spatially formed high power laser pulses. We give the principle, the approach for calculation of the needed spatial shape of illuminating radiation with corresponding energies and describe the experimental test. Considered is a specially developed by us patented laser on the base of Nd:YAG active medium. The laser provides composed spot with annular external and circle internal light each with conveniently chosen energy and time characteristics. Such formed pulse illumination assures, except for the caries lesion cleaning in given condition, the strong decreasing of the temperature gradient built in the treated enamel area and respectively permits to avoid the neighbouring enamel bursting.

1. INTRODUCTION

The application of the high power/energy laser radiation for treatment of caries or other defects in hard tooth tissues is considered as a perspective procedure [1]. Increasing the energy parameters of the operating light facilitates and allows effective treatment of the hard dental tissue. However, due to general reasons, especially due to non-homogeneous heating of the tooth tissue, this can lead also to tooth damage. The aim of this work is to present the development of the introduced by us idea for improvement of such treatment with corresponding calculation and preliminary experiments and the developed laser source on the base of our patented principle to use a complex laser spot. The laser with specialised coaxial two-beam geometry provides composed spot with annular external and circle internal light each with conveniently chosen energy and time characteristics. Such formed pulse illumination assures, except for the caries lesion cleaning, the strong decreasing of the temperature gradient in the treated area and respectively permits to avoid the strongly no desired neighbouring enamel cracking.

2. THE PROBLEM, THE PROPOSED PRINCIPLE, ANALYSIS AND LASER FOR SOLUTION

Principle and analysis

During our previous study of the processes of high energy density laser light treatment of tooth tissues [2,3], we have clearly observed the problem of enamel crack when the tooth surface is treated with high energy density laser light. From the general and well clear physical reasons, the problem via high energy and short time duration pulses using (typically employed) can be related with appearance of high temperature gradient that creates the mechanical tension, combined with the heated volume expansion. The laser illumination, typically of few hundred and less μs and respectively without the heat dissipation, increase the temperature of the treated area to many hundred degree against the few tens degree of the surrounding enamel. Both non-desired effects – tension and volume expansion, are essential factors for the crack formation.

Our experimental observation and measurement, for practically realized by us condition, show that when the laser illuminating energy $E \sim 1 \text{ J}$ is focalized in a spot with diameter of $D \sim 0.7 \text{ mm}$ ($\sim 150 \text{ J/cm}^2$) on the carious lesion, there is a

strong ablation, accompanied with the fire filament in depth of the tooth of $d \sim 0.1$ mm. In our analysis we will consider the case of small area enamel surface lesion. Using the noted dimensional data and the enamel thermo and physical parameters we can calculate the temperature increasing in the treated lesion. Our study shows that the variation of the characteristics of the same type of tooth is so large, that we can speak only for 'evaluation', i.e. with a precision in the order of 50 – 70 %. The question of this type of analysis is very complicated and has, generally speaking, the character of the qualitative discussion with some reasonable estimation. Part of the needed enamel thermo and physical parameters we take from the literature [4] and other – from our proper experimental investigations. We collected for the enamel the following series of data: mass density (ρ_e) of 2950 kg /m³, thermo-capacity (C_{ec}) of 970 J/kg.K with thermal conductivity (H_{et}) of 0.79 W/m.grad [4]. The other parameters – the latent heat of fusion (L_{ef}) and of vaporization (L_{ev}) can be taken to be as the one for some other materials that show thermic behaviour like this one of the enamel. For example, here we can note the steel and iron. For the same illuminating energy density (pulse energy, focal spot) and duration we obtain for these materials the formation of similar holes as this one in enamel. Thus, on the base of this not so strong reason, we can accept the latent heat of the fusion (L_{ef}) and the vaporization (L_{ev}) of the enamel to be no strongly different from these ones of the steel – i. e. in the order of 2.5×10^5 J/kg and 6×10^6 J/kg respectively. We accept also that the small caries lesion has approximate parameters such as the pure dentin – as these ones, noted before. From our measurement we found the coefficient of the reflection for the interesting wavelength of 1.06 μ m. For the pure enamel the reflection was as the one from a convex spherically like mirror with strong diffusion component. In the measurements we have focused the reflected light with convenient lens. We found that the reflected light is in the order of 20 % (averaged; $R_e \sim 20$ %) and strongly varied from teeth to teeth (10 to 25 %). For the carious lesion the reflection also was definitively variable for the different lesions with diffusion character and of order to 3 – 10 % (R_i). Note also that due to the low thermal conductivity of the enamel (~ 0.7 W/m. $^{\circ}$ C [4]) the heat energy cannot be dissipated and increases the temperature of the treated area.

The given approximate values showed in the previous paragraph can be still practically used for estimation of the temperature rising in the treated enamel carious lesion (averaged, typical) and of the pure enamel. Thus, for the considered spot, after some clear physical calculations (applied the composed formula (1)) we obtain that the temperature of the treated area, during the laser pulse and before the ablation, increases to be about 1400 - 1700 $^{\circ}$ C.

$$\Delta T = \left[E(1 - R_e) - (L_{ef} + L_{ev}) \cdot \left(\pi \frac{D^2}{4} d \cdot \rho_e \right) \right] * \left[C_{ec} \cdot \left(\pi \frac{D^2}{4} d \cdot \rho_e \right) \right]^{-1} \quad (1)$$

where the used notations in (1) are given in the text.

The temperature of the lesion surrounding enamel rests as of this one of the human body of $\sim 36^{\circ}$ C (for the case of absence of external heating illumination). It is reasonable that such very high temperature gradient provides high thermo-elastic tension and respectively formation of the compromising the laser treatment cracks in the enamel. As addition, the appearance of such cracks is favoured by the structural transformation for long time illumination (~ 20 s, ~ 0.1 J in the pulse) and probably by enamel melting (after 1000 $^{\circ}$ C) [4]. We will accept that for our conditions the main reason for the cracks appearance is the mechanical tension as a result of the high temperature differences (our proper observation, also from the literature [4]).

Our experiments clearly show existing of the crack problem. In Fig.1 are shown photographs of teeth after enamel lesions treatment with high energy laser light ~ 150 J/cm² (focalized $E \sim 0.8$ J on the area of ~ 0.7 mm diameter, the used by us laser pulses with duration of 0.1 to 500 μ s).

This energy density is convenient for enamel lesion cleaning. However, from the photograph, the formed cracks are clearly evident. Such cracks increase constantly with time and finally destroy the tooth.

Our experimental investigations show that for acting on the caries lesion and enamel with low laser light energy density (less than ~ 80 J/cm²) the cracks do not appear. However, the treatment (lesion cleaning) is not effective.

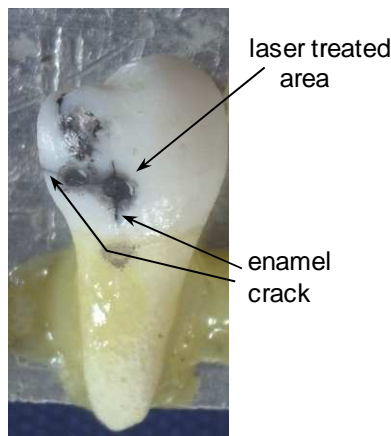


Fig. 1. Photograph of the dental caries on the enamel lesion after treating via focalized microsecond duration laser pulse with energy of 0.8 J (energy density $\sim 150 \text{ J/cm}^2$). The formed cracks in the enamel can be seen.

The idea for elimination of the essential problem with formation of cracks is to strongly reduce temperature gradient formed in the enamel operating region. For realization of this idea we have proposed and developed, on the base of our patented principle [5], a special pulsed laser, in our case with most commonly used Nd:YAG active media. The solution of the laser permits to be produced convenient composed beam for eliminating of the crack problems. On the base of application of our two coaxial channels geometry, the laser emits the complex beam, formed by the annular external part and in the bore axially disposed internal circular beam. The beam cross section of our laser is shown in the photograph in Fig. 2

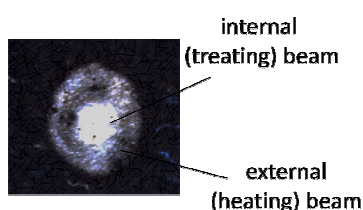


Fig. 2. The beam cross section of our laser - photograph

3. ANALYSIS

The parameters of each beam are independently controlled - energy, duration, wavelength. In this laser it is easy to form spot with external annular light that assures heating of the enamel surrounding of the treated lesion to the high temperature, however lower than this one for the cracks formation ($\sim 800^\circ\text{C}$). The internal beam for efficient treatment, heated the lesion to the noted $1400 - 1700^\circ\text{C}$. However, now the temperature difference

between lesion with high temperature and the surrounding decreases low than the difference for the crack formation. On the other hand, the temperature of the heated surrounding is less than this one, causing the cracks and thus the cracks formation is avoided.

Taken the discussed already approach for calculation; we can obtain the expression for calculation of needed energy in the annular part that permits to heat the lesion surrounding to the needed temperature. The calculations are identical to these ones given by the formula (1) but without the terms describing the fusion and vaporisation and take into account annular spot surface with approximately the same heating depth as for treatment with central spot.

4. EXPERIMENTS

Our experiments, described below, confirm well the usefulness of the developed technique and the convenience of the developed apparatus.

4.1. Laser apparatus description

As a first point, a short technical description of our coaxial geometry laser will be given. More detailed description is given in our recent work [6]. The optical scheme of the laser is presented in Fig. 3. For the advantageous realization we use low-Nd³⁺-doped (in our work ~ 0.5 at %) Nd:YAG crystal. Such doping, instead of typical $\sim 1\%$, is also commonly used and assures sufficient efficiency of the generation in combination with high quality of the output beam. The cylindrical YAG rod (diameter $\varnothing = 0.7 \text{ cm}$ and length $l = 8 \text{ cm}$) was with silvered envelope wall. Our study shows that a laser active element with the given parameters assures a notable focusing effect in the axial region, resulting in an increase of $\sim 2\frac{1}{2}$ times for the pump power density in the near axial rod part. In the experimental arrangement, the laser rod was in a close position with a pump flash-lamp in a commercial pump-chamber with UV-absorbing quartz elliptic cylinder-pump light concentrator (by silvered walls; axes $23 \times 29 \text{ mm}$, length 78 mm) and with holes for the laser rod and the lamp of $\varnothing 9.5 \text{ mm}$ and 11.5 mm . The lamp (IFP 1200 type, 700 Torr of Xe, $\varnothing 0.95 \text{ cm}$, Russia) and the crystal were surrounded with cooled flowing water at temperature $18 \pm 0.3^\circ\text{C}$. The electrical supply was standard, homemade, providing electric energy from 70 to

160 J in $\sim 400 \mu\text{s}$ FWHM lamp pulse duration (at 1 Hz repetition rate). Typically, we have used as pump energy of 140 J.

The light generation at two beams was achieved in two, coaxially arranged and optically separated parts of the Nd:YAG laser rod, each equipped with its own 40 cm length resonator (hatched differently in Figure 2 (a)). The optical separation is realized using a rectangular separating prism SPr with a hole (in our experiment with 3.7 mm diameter, length of 4 mm) through the cathetus and the hypotenuse. A thin metal tube with ~ 0.12 mm thick walls and 30 mm length was introduced in the hole. The external part is coupled with its resonator by reflection of the SPr outside the hole. The described prism separator assures very good formation of both spots.

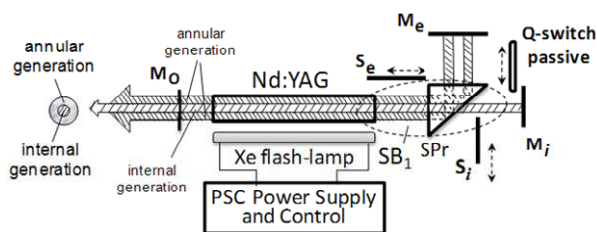


Fig. 3. Scheme of the developed two-coaxial beam emitting Nd:YAG laser, using as separator of the channels a prism SPr with a hole and selective-flat mirror resonators. The passive Q-switch is Cr^{4+} :YAG plate with convenient parameters

4.2. Experimental test

In our work, we have experimentally illustrated the use of our described two-channel laser, the ideology of the composed beam and the given approaches for laser beam parameters estimation. For the test we investigate the small surface laser lesions on the enamel (diameters $\sim 0.7 - 1$ mm). This permits the usage of focalized laser beam for treatment. We found that the effectiveness of the laser action increases essentially if the treated area of the enamel by the laser was slightly marked with black pencil. The corresponding energy is estimated by expression (1). For our condition of the treated small area lesions (diameters of ~ 0.7 mm) we have estimated the laser treating beam energy to be ~ 0.7 J (energy density $\sim 150 \text{ J/cm}^2$). This provides temperature increasing in the treated area up to $\sim 1700^\circ\text{C}$. The heating beam has external diameter of 1.5 mm and internal one of 0.7 mm. The needed energy was estimated

to be ~ 0.3 J assuring increasing of the temperature to $\sim 700^\circ\text{C}$.

With our laser, described already in Sec.3.1, we easily have realized these requirements. The principle of the technical realization via laser beam focalization is shown in Fig. 4 (the picture). With stopped heated beam (external beam) we, as a rule, have obtained the effects of enamel cracking around and in the treated area, as it is shown in Fig. 1. The crack traces on the enamel is clearly evident.

When the laser produces the complex beam with the described parameters, no cracking was noticed. In Fig. 5 is given the photograph of the tooth after treating via focalized laser light. Note that to improve absorption by the caries we have coloured the illuminated tooth's surface with appropriate very thin black dye layer.

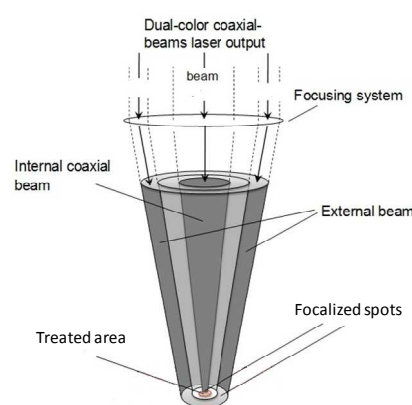


Fig. 4. Scheme of the technical realization via laser beam focalization

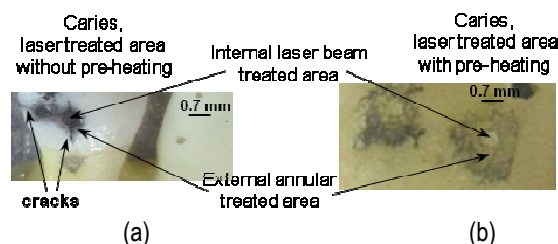


Fig. 5. The photograph of caries treated area with direct illumination with a Q-switched pulse (a) and with annular illumination before high power pulse; (b) – no trace of crack can be seen

5. CONCLUSION

In the work we have reported the important details of proposed by us principle for improvement of enamel caries treatment using spatially formed high power laser pulses. The developed formed

pulse illumination, assure, except for the caries lesion cleaning in given condition, the strong decreasing of the temperature gradient built in the treated enamel area and respectively permits to avoid the neighbouring enamel bursting. We give the principle, the approach for calculation of the needed spatial shape of illuminating radiation with corresponding energies and describe the experimental test. The used Nd:YAG laser for the experimental test, specially developed by us on the base of patented principle, is shortly described. Generally speaking, as we have noted already, that the phenomenon of cracking vary essentially with the teeth treated, especially the laser energy density and power. This is related with the treated teeth property variation. However, the proposed solution for the cracks formation avoiding can be generalised with the chosen convenient combination of the complex light beam parameters for lager assurance of the positive action. This is the problematic of our future work.

ACKNOWLEDGEMENTS

Thanks to the contracts DNTS/Austria 01/3 (Pr. No. BG 07/2013) for useful scientific cooperation and Technical University of Sofia, R&D Department, Laboratory of Quantum and optoelectronics (QOEL) and Dept. Optoelectronics and Lasers, Branch Plovdiv where this work was carried out.

References

- [1] V. S. Beena, Laser application in dentistry, J.of.D., Indian Dental Associaton, vol.63, Issue 3 (1992) 1-7
- [2] P. Uzunova, T. Uzunov, S. Rabadjiiska, N. Kaimakanova, M. Deneva, M. Nenchev, Analisis of the penetration of the laser radiation in dental tissue, J. Techn. Univ. Sofia, br. Pd Vol. 16 (2011) 179-183
- [3] P. Uzunova, S. Rabadjiiska, Tz. Uzunov, Hr. Kisov. N. Kaimakanova, E. Dinkov, M. Deneva, M. Nenchev, Study the penetration of IR laser radiation in human teeth - determination of the absorbed and scattered parts, Proc. SPIE, Vol.8770-50 (2013) 87701A-1-7
- [4] W. Seka, D. Fried, J.D.B. Featherstone and S.F. Borzillary, Light Deposition in Dental Hard Tissue and Simulated Thermal Response, J Dent Res 1995 74:1086; R. Bedini, Ann.Inst. Super. Santina, Vol.46, 2, Apr, June (2010)
- [5] M. Nenchev, Multicolor laser, Bulg. patent IIR No 25954/reg.38529
- [6] M. Deneva, M. Nenchev, E. Wintner, S. Topcu, Coaxial-geometry tunable dual-wavelength flashlamp-pumped Nd:Yag laser, J. Optical and Quantum Electronics, Springer, DOI: 10.1007/s11082-015-0205-3 (2015).

DEMODULATOR FOR SATELLITE TV SIGNALS

Lyubomir Laskov

Department of Radio Communications and Video Technologies, Faculty of Telecommunications,
Technical University of Sofia, 8 Kl. Ohridski Blvd, Sofia 1000, Bulgaria,
E mail: laskov@mail.com

Abstract

In this paper the demodulator of satellite television signals formed by standard DVB-S2 is considered. A detailed block diagram and description of the blocks are given. A mathematical description of the algorithms used for carrier phase recovery is given. A parametric analysis of these units is done.

1. INTRODUCTION

One of the main problems in digital satellite TV receivers is the carrier phase recovery. The reason for this is the fact that the DVB-S2 receiver should operate at very low CNRs and consumer-type DVB-S2 receivers typically use low cost oscillators, which introduce a large initial carrier frequency offset. An additional problem occurs when operating in Adaptive Coding and Modulation (ACM) mode in which modulation can change at any package.

In the satellite TV receiver, the radio signal with intermediate frequency obtained after the second frequency conversion is digitized and transmitted in the form of samples with the symbol rate. It is important to take samples at the right moment, because otherwise the influence of inter-symbol interference increases. For this purpose the position of the maximum peak is necessary to be accurately determined. This is achieved by usage of the symbol timing recovery circuits.

It is known that the maximum noise immunity is provided by coherent demodulation, in which the carrier frequency and carrier phase are required to be known. Therefore it is necessary to perform accurate recovery of the carrier frequency and carrier phase and for this purpose the carrier frequency and phase recovery circuits are used.

In systems in which seeks simplicity of the scheme implementation and sustainability usually non-coherent or kvazi-coherent demodulation are used. Since in this type of demodulation the decision is based on the phase shift, which itself does not depend on current state of phase, then only carrier frequency recovery is performed.

It is generally assumed that in satellite-receiver channel the attenuation is a constant, depending only on the carrier to noise ratio at the receiver input. The other effects (clock and frequency errors, phase noise, etc.) are usually counted as occurred in the receiver. Errors in timing recovery are obtained mainly because of the instability of the generator providing a clock frequency for sampling. The main reasons for the carrier frequency errors are the instability of the generator used in low noise converter (LNC) and the Doppler effect caused by the movement of geostationary satellites. The main source of phase noise is a radio-frequency generator in LNB, and the influence of the tuner can be ignored.

The aim of this paper is to provide background information for digital processing in the second generation satellite TV receiver, and to examine the effectiveness of systems for carrier phase recovery.

2. BLOCK DIAGRAM OF DVB-S2 DEMODULATOR

Fig. 1 shows a block diagram of the demodulator of the satellite signals formed according to the standard DVB-S2. Incoming signal with intermediate frequency (IF) is digitized by high speed Analog to Digital Converter (ADC) and submitted to the block Digital Down Converter (DDC). The sample rate F_s in the ADC is chosen such that to satisfy the Nyquist criterion and to be k times larger than the symbol rate R_s of the received signal, where k is an even number. In DDC a two-step process is implemented, in the first one samples from the ADC are multiplied by a periodic sequence, as a result yielding two complex I and Q signals with a frequency equal to half of the input signal frequency

$(F_s / 2)$. In order to avoid unwanted high-frequency components, the resulting signals pass through a low pass filter, and then subjected to a frequency reduction.

In the second step of processing in DDC, the signal passes through a programmable frequency reducer, consisting of digitally controlled oscillator (NCO) and a complex multiplier. NCO is controlled

by coarse carrier frequency recovery block. The signal obtained by the complex multiplication is fed to Sample Rate Converter (SRC), which consists of Polyphase filter with a Finite Impulse Response and suitable decimator. Its purpose is to transform the samples rate so that the rate of output samples is an integer times bigger the real rate of the samples.

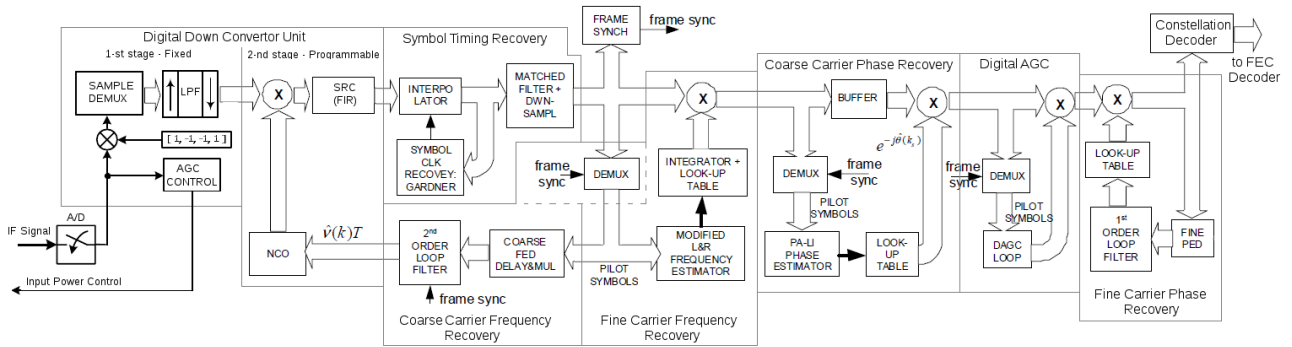


Fig. 1. Block Diagram of DVB-S2 Demodulator

In order to ensure that the signal level of the ADC input will be in its dynamic range, in the DDC is provided a control unit of the system for automatic gain control (AGC) of the IF amplifier.

The signal obtained at the output of the DDC is fed to the Symbol Timing Recovery (STR) block. It consists of a cubic interpolator with Farrow's structure, Gardner Timing Error Detector (TED), as well as the second order filter connected in a feedback circuit. The main task of the interpolator is to calculate the output samples $y(kT_i)$ on the basis of the input samples $x(mT_s)$ and the error information (m_k и μ_k) coming from sub-blocks "Symbol Clk Recovery; Gardner". When with T_s is denoted the period of input samples, and with T_i the period of interpolated output samples.

The sub-block "Symbol Clk Recovery; Gardner" has several functions, namely: determining the timing error by using Gardner's algorithm, proportional integration through first order loop filter and management of the interpolator. The main advantage of the Gardner's algorithm is its independence from the transmitted information and frequency error. The bandwidth of the filter in the feedback determines the time for synchronization as well as accuracy during operation in search and track modes. For each input sample control device calculated base point m_k and relatively delay μ_k , in order to obtain the corresponding interpolated values.

The last sub-block of the symbol timing recovery system is "Matched Filter + Dwn Sampl." Its task is to ensure a coherent filtering and appropriate decreasing of the frequency of samples generated by STR cycles.

The package synchronization is done by searching the header of the physical layer by suitable correlator, operating symbol by symbol. By using differential decoding correct packet synchronization is possible even in the presence of a large carrier frequency error. The block is implemented through a shift register consisting of 89 elements, divided into two groups - the first (25 elements) is connected to the symbols indicating the start of a packet (SOF), and the second (64 pieces) - with the symbols of the physical layer (PLS). There are 57 connections to the 89 elements of the shift register, as in the second half only 32 of the 64 symbols are known in the receiver. The contents of the shift registers is multiplied by the relevant coefficients and then summed. The maximum value of the outputs of the two adders, whose signal is fed to a peaks detector is obtained when the whole header of the physical layer occur in the shift register.

In DVB-S2 a two-layer system for carrier frequency recovery is used. The coarse carrier frequency recovery is initially performed, by using the second order feedback loop, based on the frequency error detector which use "delay and multiply" (D & M) algorithm. For fine carrier frequency recovery a

modified version of the Lewis and Regianini (L & R) algorithm is used, which is boiling down to averaging the sums of autocorrelation functions for many neighboring fields before calculating the argument of the function. Detailed information, block diagrams and mathematical description of the carrier frequency recovery are given in [9].

The carrier phase recovery can be achieved by single-layer (for QPSK and 8PSK modulations), or dual-layer (for APSK modulations) system. In the coarse carrier phase recovery (applied to any received signals) for evaluation of phase error is used forward link system based on the maximum likelihood (FF-ML) algorithm, using pilot fields. In this technique is carried out finding of the phase trajectory at the time of the data symbols by using a linear interpolation on two consecutive / neighboring pilot fields as for each pilot field was calculated average phase.

The separation of pilot signals is done by the demultiplexer (Demux), while in the block "Pa-Li Phase Estimator" is carried out a mathematical processing and the calculation of the error signal corresponding to the phase during the information signal. Thus, obtained signal is fed to the look-up table, which makes a comparison of the error signal with the coefficient corresponding to an obtained phase error. For the duration of corresponding processing, the signal is stored in the buffer.

For fine carrier phase recovery a feedback system, based on algorithm for determining of the phase error by raising the input signal to the Q-degree (Q = 3 for 16APSK and Q = 4 for 32APSK) is used. The algorithm is applied directly to the transmitted information. When 16 APSK / 32APSK constellations is raised on third / fourth degree and then phase shifted on $0 / \pi / 4$ rad, the inner points of the original constellations are collected in the center, while the outer points form a QPSK constellation.

Raising of the input constellation on the corresponding degree, its phase shifting, as well as the mathematical processing of the resulting signals is performed in the block "Fine PED". The error signal from the output of the block passes through the first order filter and fed to a look-up table in which a comparison of the error signal and the phase error is performed.

Typical for this algorithm is its simplicity as well as the fact that it is relatively insensitive to the amplitude errors, because of the operation "cutting of

quadrant". The presented algorithm is not suitable for use in the demodulators with a "hard" decision.

Block digital Automatic Gain Control (DAGC) is placed after coarse carrier phase recovery system. Its purpose is to change the levels of the incoming symbols to those of the reference constellation. This is required because the decoder needs precise "soft" information about the distance between the received symbol and reference point from the constellation. For this purpose, the pilot symbols are separated in the Demux and fed to the block DAGC Loop for evaluation of their amplitude. Based on this evaluation, the appropriate coefficient is selected, with which the data symbols are multiplied.

3. MATHEMATICAL DESCRIPTION OF THE STUDIED ALGORITHMS FOR CARRIER PHASE RECOVERY

The phase estimation in the method of coarse carrier phase recovery is obtained by the using of L_p number of samples from the output of the matched filter corresponding to the pilot signals and by applying the following mathematical operation:

$$\hat{\theta}^{(p)} = \arg \left(\sum_{k=0}^{L_p-1} \{c^{(p)}(k) * z^{(p)}(k)\} \right) = \theta + N_I \quad (1)$$

The second equality is valid at high CNR, as N_I denotes Gaussian noise with zero mean value corresponding to the phase evaluation and having dispersion

$$\sigma_{N_I}^2 \cong \sigma_{\hat{\theta}^{(p)}}^2 = \frac{1}{2L_p E_s / N_0} \quad (2)$$

In order to ensure that the phase will not grow beyond the interval $[-\pi; \pi]$ system to determine the total phase evaluation is used. If with l denote the number of the pilot evaluation, the final unwrapped evaluation $\theta^{(p)}(l)$ is calculated on the basis of $\hat{\theta}^{(p)}(l)$ by the expression

$$\hat{\theta}_f^{(p)}(l) = \hat{\theta}_f^{(p)}(l-1) + \alpha \text{SAW}[\hat{\theta}^{(p)}(l) - \hat{\theta}_f^{(p)}(l-1)], \quad (3)$$

where $\text{SAW}[\Phi] = [\Phi]^{+\pi, -\pi}$ is a saw tooth non-linearity that reduces Φ to the interval $[-\pi; \pi]$, a α is a parameter in the range $0 \leq \alpha \leq 1$, which is usually chosen to be equal to 1 ($\alpha = 1$).

The cycle slip probability P_{CS} is determined by the expression

$$P_{CS} = \Pr\{\hat{\theta}^{(p)}(l) - \hat{\theta}^{(p)}(l-1) > \pi\} =$$

$$= 2 \int_{\pi}^{\infty} \frac{1}{\sqrt{4\pi\sigma_{N_l}^2}} e^{-\frac{x^2}{4\sigma_{N_l}^2}} dx \quad (4)$$

The system for fine carrier phase recovery uses an algorithm for determining the phase error by raising the input signal on the Q-th degree. For the given algorithm estimated by the detector phase error has the form

$$e_{\phi}(k) = \text{Im}\{q(k) \cdot (\text{sign}[\text{Re}\{q(k)\}] - j \text{sign}[\text{Re}\{q(k)\}])\} \quad (5)$$

where

$$q(k) = \begin{cases} [z(k)]^3 & \text{3a } 16\text{APSK} \\ [z(k)]^4 e^{j\frac{\pi}{4}} & \text{3a } 32\text{APSK} \end{cases} \quad (6)$$

4. PARAMETRIC ANALYSIS OF THE STUDIED ALGORITHMS

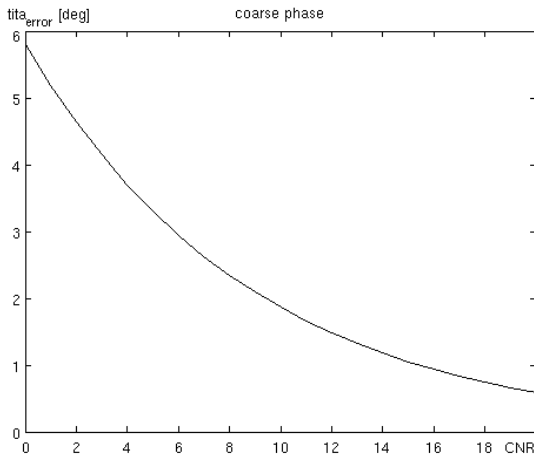


Figure 2. Dependence on phase estimation of CNR

The dependence of the estimated phase error on the carrier to noise ratio for the system for coarse carrier phase recovery is shown on Fig.2. During the simulations it is accepted that there is no residual frequency error, and the number of pilot signals in one sequence is: $L_p = 36$. From the figure it is seen that with the increase of CNR the dependence of the established phase error becomes weaker, while for large values of CNR it has a value close to 0. The figure allows determining the estimated phase error by the system for a given value of the CNR. In the working range for the DVB-S2 receivers ($9 \text{ dB} \leq \text{CNR} \leq 12 \text{ dB}$) the value of the estima-

ted phase error varying in the interval from $2,1^\circ$ to $1,5^\circ$.

Fig. 3 shows the influence of the ratio of energy per symbol to the Spectral Noise Density (E_s/N_0) to the cycle slip probability in the system for coarse carrier phase recovery for different number of pilot signal in the pilot block.

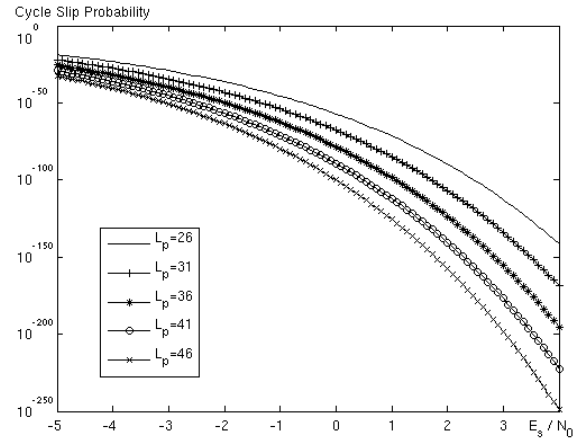


Figure 3. Dependence on cycle slip probability of E_s/N_0

From fig. 3 it is seen that by increasing the number of the pilot signals cycle slip probability decreases. The cycle slip probability for different values of the E_s/N_0 and L_p are given in Table 1. From Table 1 it is seen that even when the $E_s/N_0 = -2 \text{ dB}$ the cycle slip probability is very small, which allows the given algorithm to be widely used in satellite television receivers from the second generation.

Table 1. cycle slip probability

E_s/N_0	$L_p=26$	$L_p=31$	$L_p=36$	$L_p=41$	$L_p=46$
-2 dB	10^{-36}	10^{-43}	10^{-50}	10^{-57}	10^{-63}
0 dB	10^{-57}	10^{-68}	10^{-78}	10^{-89}	10^{-100}
2 dB	10^{-90}	10^{-107}	10^{-124}	10^{-141}	10^{-158}
4 dB	10^{-142}	10^{-168}	10^{-196}	10^{-222}	10^{-249}

Fig. 4 shows the dependence on the variation of estimated phase error of the E_s/N_0 at coarse carrier phase recovery system, for different values of the residual frequency error. During the simulations it is accepted that $L_p = 36$. The figure shows that when reducing residual frequency error below 10^{-3} its influence on the variance of estimated phase error is minimal.

The dependence on the average value of the estimated phase error, of the CNR, at the fine carrier phase recovery system for different modulations is given in Fig. 5. From that figure can determine the value of the estimated phase error depending on

the CNR at the input of the receiver. In the working range for the DVB-S2 receivers the value of the estimated phase error varying in the interval from $3,975^\circ$ to $3,945^\circ$ for 16APSK modulation and from $1,516^\circ$ to $1,5^\circ$ for 32APSK modulation.

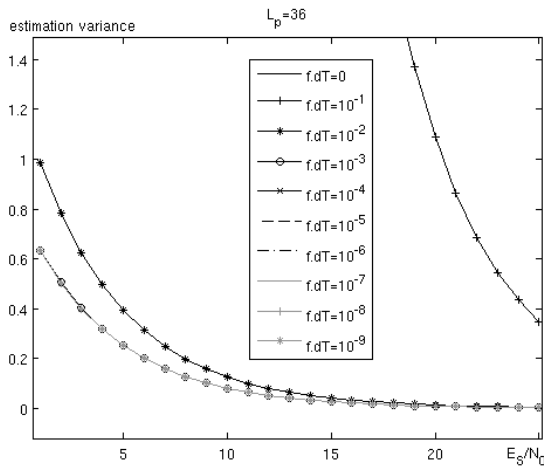


Figure 4. Phase estimation variance vs frequency offset

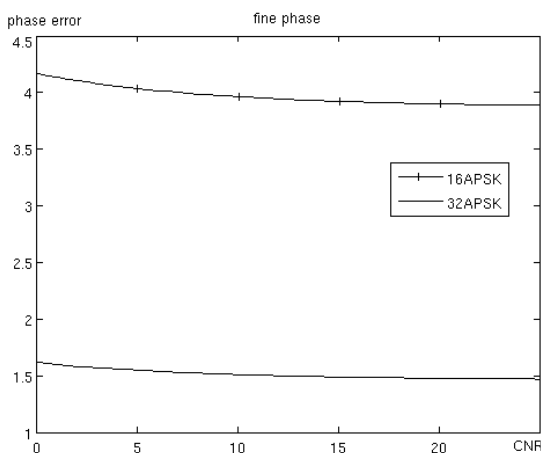


Figure 5. Dependence on average phase estimation of CNR

5. CONCLUSION

Presented in this paper mathematical models and graphical dependencies of the carrier phase recovery systems makes possible to determine the estimated phase error, its dispersion and the cycle slip probability, depending on the carrier to noise ratio as well as the number of pilot symbols in a block and residual frequency error.

6. APPENDIX AND ACKNOWLEDGMENTS

The research described in this paper is supported by the Scientific Research Sector of TU-Sofia under the contract No 142пд0011-07.

References

- [1] Morello, V. Mignone, DVB-S2: The second generation standard for satellite broadband services, Proc. IEEE, vol. 94, no. 1, pp. 210227, Jan. 2006.
- [2] E. Casini, R. De Gaudenzi, A. Ginesi, DVB-S2 modem algorithms design and performance over typical satellite channels, International Journal of Satellite Communications and Networking 2004, vol. 22(3), pp. 281–318, 2004.
- [3] ETSI TR102 376 v1.1.1, Digital Video Broadcasting (DVB) User guidelines for the second generation system for Broadcasting, Interactive Services, News Gathering and other broadband satellite applications (DVB-S2), 2005.
- [4] F. M. Gardner, A BPSK/QPSK timing-error detector for sampled receivers, IEEE Trans. Commun., vol. 34, no. 5, pp. 423–429, May 1986.
- [5] F. M. Gardner, Interpolation in digital modems - Part I: Fundamentals, IEEE Trans. Commun., vol. 41, pp. 502–508, Mar. 1993.
- [6] F. W. Sun, Y. Jiang, L. N. Lee, Frame synchronization and pilot structure for DVB-S2, Int. J. Satell. Commun. Network., vol.22, no. 3, pp. 319–339, May–Jun. 2004.
- [7] J. Gyu Oh, J. Tae Kim, An Alternative Carrier Frequency Synchronization Scheme for DVB-S2 Systems, ICACT'10 Proceedings of the 12th international conference on Advanced communication technology, pp. 529–533
- [8] L. Erup, F. M. Gardner, R. Harris - Interpolation in Digital Modems - Part II Implementation and Performance, IEEE Trans. Commun., vol. 11, no. 6, pp. 998–1008, June 1993
- [9] L. Laskov L. Jordanova. Algorithms for Carrier Frequency Recovery in DVB-S2 receivers. Proceedings of the Science Journal "Electrotechnica+Electronica" E+E (приета за отпечатване).
- [10] L. Litwin, Matched filtering and timing recovery in digital receivers. A practical look at methods for signal detection and symbol synchronization, www.rfdesign.com, September 2001
- [11] M. Luise, R. Reggiannini, Carrier frequency recovery in all-digital modems for burst mode transmissions, IEEE Trans. Commun., vol. 43, no. 2/3/4, pp. 1169–1178, Feb/Mar/Apr 1995.
- [12] M. Oerder, H. Meyr, Digital filter and square timing recovery, IEEE Trans. Commun., vol. 36, no. 5, pp. 605–612, May 1988
- [13] P. Savvopoulos, N. Papandreou, Th. Antonakopoulos, Architecture and DSP Implementation of a DVB-S2 Baseband Demodulator, Euromicro Symposium on Digital Systems Design (DSD), 2009, pp. 441–448
- [14] P. Savvopoulos, T. Antonakopoulos, Comparative performance analysis of symbol timing recovery for DVB-S2 receivers, In Proc. 13th Ka and Broadband Communications Conference, Turin, Italy, Sep. 2007
- [15] U. Mengali, A. N. D'Andrea, Synchronization Techniques for Digital Receivers, New York: Plenum, 1997.

INFRARED INVESTIGATION ON THE THERMAL FIELD IN THE CASE OF INFLUENCE OF ULTRA HIGH FREQUENCY SIGNALS ON THE HUMAN BODY

Desislava Chocheva, Viktor Mihaylov, Kalin Dimitrov

8, Kl. Ohridski, Sofia, Bulgaria, TU-Sofia, bl. 1, lab.1257
+359 2 965 3145; des@motorsport.bg, vvmihaylov@abv.bg, kld@tu-sofia.bg

Abstract

In this paper the subject of infrared thermal imaging cameras and their potential for medical applications are investigated. Two different medical physiotherapeutic appliances are reviewed in terms of heat eminence during a standard therapy session..

1. INTRODUCTION

Through the development of technics and technology, every day we are facing new perspectives in health care – both diagnostically and therapeutically. What is observed in the last few years is an increasingly more significant implementation of infrared thermal-imaging-based medical apparatus, generally in the diagnostic sphere. However the potential of this technology in contemporary medicine is still to be explored in further detail. The current paper is an attempt to broaden the view and deepen the understanding of some of the existing therapies (ultrasound and UHF) through the analysis of data provided by a thermal camera.

2. CURRENT STATE OF THE PROBLEM

Another broadly accepted for its soothing, anti-inflammatory, desensitizing, trophic, anti-hypertensive and stimulating effect of regenerative processes in damaged tissues is the UHF pulse therapy. Given the fact, that the spectrum of this therapy (40.86MHz) is known to hold certain risks in special cases (such as patients with neoplasms, cardiac insufficiency with signs of decompensation, pronounced atherosclerosis, hyperthyroidism, a tendency to bleeding, pregnancy, pulmonary tuberculosis in advanced lesions and risk cause haemoptysis), it is beneficial to be able to analyse thoroughly the coverage of greater influence of the appliance. This can be achieved with a great amount of accuracy through the analysis of the thermal field, changed throughout the therapeutic session under the emission of the UHF apparatus.

3. EXPERIMENTS

For the experiments the same thermal camera is used for data collection – FLIR E40, with thermal sensitivity of $< 0.07^{\circ}\text{C}$, accuracy of $\pm 2^{\circ}\text{C}$ or $\pm 2\%$ of reading and temperature range of -4°F to $1,202^{\circ}\text{F}$ (-20°C to 650°C) [3], [4]. For maximum accuracy, the camera is fixed on a stand and movement of the object is avoided.

With UHF therapy the setting includes two objects of interest – one is the patient and another one for testing the amount of thermal radiation emitted outside of the direct field of application, shown in Fig. 1:



Fig. 1. UHF therapy – sinusitis treatment

4. RESULTS

For the UHF therapy images there are 3 points of analysis used in all 19 thermal images taken – SP1, which is where directly next to the point of application of the plates, SP2, which is a control point on the head of the patient and SP3, which is on another person in the room, but far from the plates (Fig. 2):

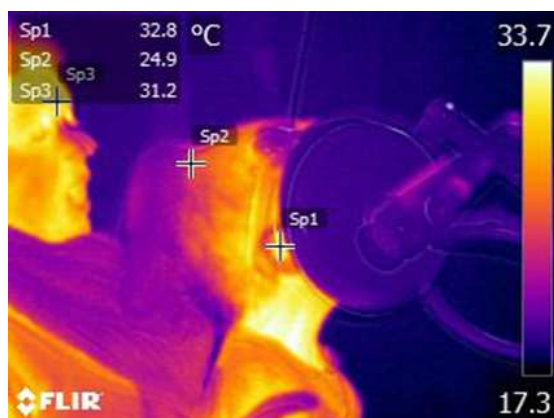


Fig. 2 Thermal image of UHF therapy – points used for analysis

It is important to note that for each image the emissivity of human skin is considered through the coefficient $\varepsilon=0.98$.

The data collected from the UHF session shows a steady temperature rise as for all examined points (Fig. 3).

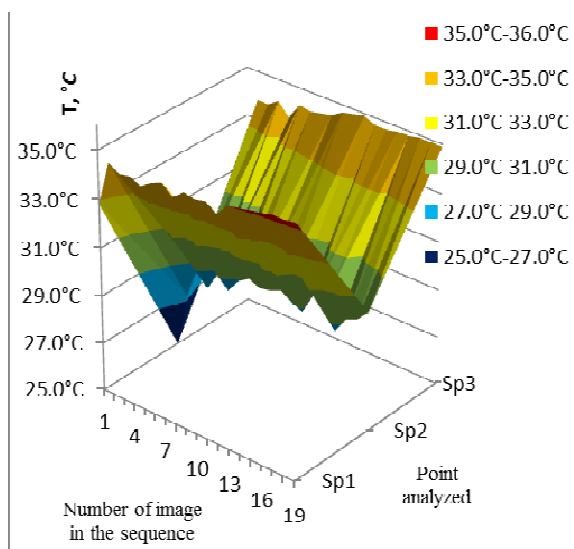


Fig. 3. UHF Therapy – thermal changes in the analyzed points

What is observed in a more dynamic temperature increase at the beginning of the session for all points of analysis (with about 3-4 °C) and then a

more gradual, but still noticeable increase until the end. It should be emphasized that there is a major temperature rise for SP3 (3,7°C), which is chosen to be in a subject different from the one to whom the treatment is directly applied. This means there is significant emission outside of the plates' focal point, which could make it dangerous for anyone in the near proximity. That is why it is of great importance to use a shielded room (Faraday cage) for UHF treatment sessions.

5. CONCLUSION

The analyzed data gives one more perspective of the countless applications of thermal imaging cameras for medical purposes. Such analysis can be very useful in providing a new understanding of widely-used technology in terms of safety and effectiveness. Since IR imaging is non-invasive and does not bear and risks, it can be implemented wherever it is useful and possible. It carries a great potential also for diagnostic medicine – early tumor/cancer detection, diagnosing neuropathies, all kinds of inflammation, scanning large groups of people for high body temperature, veterinary purposes and many others. In the near future IR thermography might become a valid single diagnostic method for many diseases that involve intricate changes in temperature field.

6. APPENDIX AND ACKNOWLEDGMENTS

This research was supported by the personnel of Studentska Polyclinic and Technical University of Sofia. We want to thank them for facilitating this research and providing the appliances to analyze.

We would also like to thank Prof. Dimitar Dimitrov for assisting whenever needed and for providing comments that greatly improved this paper.

References

- [1] Childs P., (et. all), Practical Temperature Measurement. Butterworth Heinemann, Reed Elsevier plc group, 2001.
- [2] Darling, Charles R.; "Pyrometry. A Practical Treatise on the Measurement of High Temperatures." Published by E.&F.N. Spon Ltd. London. 1991.
- [3] http://www.scigiene.com/productimages/429_INFRARED_THERMOMETERExplanation.doc.pdf - Scigiene Corporation, 1295 Morningside Avenueue, Unit 16, Scarborough, ON M1B 4Z4, Canada
- [4] <http://www.flir.com/cs/emea/en/view/?id=41372> - FLIR Systems, Inc.

MULTIPLE SCLEROSIS DIAGNOSTICS BASED ON SIMULTANEOUS USE OF EEG AND INFRARED THERMOGRAPHY

Viktor Mihaylov, Kalin Dimitrov

8, Kl. Ohridski, Sofia, Bulgaria, TU-Sofia, bl. 1, lab.1257
+359 2 965 3145; vvmihaylov@abv.bg, kld@tu-sofia.bg

Abstract

In this paper the subject of simultaneous use of infrared thermography and EEG are investigated. Two different diagnostic methods are reviewed in terms of standard sessions.

1. INTRODUCTION

The ability to detect problems early on is a tremendous advantage that is gained through technological advances in the medical imaging field. Diagnosing patients is becoming easier and less intrusive. Most medical imaging methods, however, are becoming increasingly hard to set up and expensive. Medical thermography is one of these technological advances and provides a diagnostic medical imaging procedure that is non-invasive, objective, and relatively inexpensive. EEG is used in the diagnosis of MS but in conjunction with other tests. Utilizing medical thermography might speed up and ease that process.

2. CURRENT STATE OF THE PROBLEM

Thermal Imaging Cameras can be used for a variety of disease monitoring, trending, and medical applications. Multiple sclerosis causes poor circulation and blood flood to the extremities.

"Multiple sclerosis (abbreviated MS, also known as disseminated sclerosis or encephalomyelitis disseminata) is an autoimmune disease in which the body's immune response attacks a person's central nervous system (brain and spinal cord), leading to demyelination. Disease onset usually occurs in young adults, and it is more common in females. It has a prevalence that ranges between 2 and 150 per 100,000. MS was first described in 1868 by Jean-Martin Charcot.

MS affects the ability of nerve cells in the brain and spinal cord to communicate with each other. Nerve cells communicate by electrical signals called action potentials down long fibers called axons. Those are wrapped in an insulating substance called myelin. In MS, the body's own immune sys-

tem attacks and damages the myelin. Due to myelin is depletion, the axons can no longer effectively conduct signals. The name multiple sclerosis refers to scars (scleroses—better known as plaques or lesions) in the white matter of the brain and spinal cord. It is mainly composed of myelin. Although much is known about the mechanisms involved in the disease process, the cause remains unknown. Different environmental risk factors have also been found.

MS takes several forms, with new symptoms occurring either in discrete attacks (relapsing forms) or slowly accumulating over time (progressive forms). In between attacks, symptoms may vanish, but permanent neurological problems often occur, especially as the disease advances.

Treatments attempt to return function after an attack, prevent new attacks, and prevent disability. MS medications can have adverse effects or be poorly tolerated, and many patients pursue alternative treatments, despite the lack of supporting scientific study. The prognosis is difficult to predict; depending on the type of the disease, the individual patient's disease characteristics, the initial symptoms and the degree of disability the person experiences as time advances

An EEG is a non-invasive method for identifying seizure disorders.

3. EXPERIMENTS

For experiments the same thermal camera is used for data collection – FLIR E40, with thermal sensitivity of $< 0.07^{\circ}\text{C}$, accuracy of $\pm 2^{\circ}\text{C}$ or $\pm 2\%$ of reading and temperature range of -4°F to $1,202^{\circ}\text{F}$ (-20°C to 650°C) [3], [4]. For maximum accuracy, the camera is fixed on a stand and movement of the object is avoided.

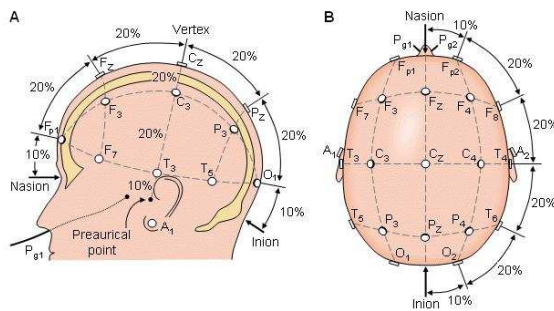


Figure 1. Standard EEG electrode distribution 20-10 System

EEG signals have highly non-Gaussian and non-stationary characteristics. In order to extract any beneficial information signal processing has to be employed. The postsynaptic potentials sum is the range of about 5uV to 100uV and frequency range 3Hz to 70Hz [4]. This narrows down to a few of the shelf solutions as the one chosen for the project – National Instruments USB-6211 data acquisition module alongside the LabView graphical programming language. LabView allows a fast paced and low cost development of smart algorithms for signal processing. Also utilized is the Nihon Kohden EEG 9100.

A setup was prepared to approximate standard EEG acquisition techniques – separated from active electronics and with reduced electromagnetic interference. Signal recordings were made with differentiation in the electrode to electrode comparison. NRSE (detect the ground voltage provided by the signal for all EEG leads) and differential voltage between the electrodes. 7 of the frontal leads are chosen for the measurement – Z (for ground - ear), Fp1, Fp2, F7, F3, Fz, F4 and F8. All are placed on the EEG cap and linked to bridge electrodes.

4. RESULTS

There are 3 points of analysis used in all 19 thermal images taken – SP1, which is where directly next to the point of application of the plates, SP2, which is a control point on the head of the patient and SP3, which is on another place.

The data collected from the recorded session shows a steady temperature rise as for all examined points.

What is observed in a more dynamic temperature increase at the onset of the measurement for some points of analysis (with about 2-2.5 °C) and then a more gradual, but still noticeable increase until the end. It is hard to differentiate a significant increase

in any of the points. Thus meaning a more circum-spect and segregated analysis should be performed.

5. CONCLUSION

The analyzed data gives one more perspective of the countless applications of thermal imaging cameras for medical purposes. Such analysis can be very useful in providing a new understanding of widely-used technology in terms of safety and effectiveness. Since IR imaging is non-invasive and does not bear and risks, it can be implemented wherever it is useful and possible. It carries a great potential also for diagnostic medicine – early tumor/cancer detection, diagnosing neuropathies, all kinds of inflammation, scanning large groups of people for high body temperature, veterinary purposes and many others. In the near future IR thermography might become a valid single diagnostic method for many diseases that involve intricate changes in temperature field. Allocating cognitive tasks through each measurement would allow better spatio-temporal segregation.

6. APPENDIX AND ACKNOWLEDGMENTS

This research was supported by the personnel of diagnostic-consultant practice "Dr. Alexiev and son" and Technical University of Sofia. We want to thank them for facilitating this research and providing the appliances to analyze.

We would also like to thank Prof. Dimitar Dimitrov for assisting whenever needed and for providing comments that greatly improved this paper.

References

- [1] Childs P., (et. all), Practical Temperature Measurement. Butterworth Heinemann, Reed Elsevier plc group, 2001.
- [2] Darling, Charles R.; "Pyrometry. A Practical Treatise on the Measurement of High Temperatures." Published by E.&F.N. Spon Ltd. London. 1991.
- [3] http://www.scigiene.com/productimages/429_INFRARED_THERMOMETERExplanation.doc.pdf - Scigiene Corporation, 1295 Morningside Avenueue, Unit 16, Scarborough, ON M1B 4Z4, Canada
- [4] <http://www.flir.com/cs/emea/en/view/?id=41372> - FLIR Systems, Inc.
- [5] Letizia Leocani, Bruno Colombo; "Fatigue in Multiple Sclerosis Is Associated with Abnormal Cortical Activation to Voluntary Movement—EEG Evidence" Neurol-

mage, Volume 13, Issue 6, June 2001, Pages 1186–1192

- [6] P. Striano, G. Orefice, V. Brescia Morra; “Epileptic seizures in multiple sclerosis: clinical and EEG correlations”; *Neurological Sciences*, December 2003, Volume 24, Issue 5, pp 322-328
- [7] S.D.Jenkins and R.D.H.Brown; “A correlational analysis of human cognitive activity using Infrared Thermogra-

CEMA’15 conference, Sofia

phy of the supraorbital region, frontal EEG and self-report of core affective state”

- [8] Sean Jenkins, Raymond Brown, Neil Rutterford; “Comparing Thermographic, EEG, and Subjective Measures of Affective Experience During Simulated Product Interactions”; *International Journal of Design*, Vol 3, No 2, 2009

EVALUATION OF EXPERIMENTAL RESULTS FOR DIFFERENT CENTRIFUGES AND PURPOSES FOR OPTIMIZATION

Tsvetan Kachamachkov, V. Manoev

8, Kl. Ohridski, Sofia, Bulgaria, TU-Sofia,
Postal Sofia - 1309,,Sv. Troitsa" 303 - B - 39

Abstract

Construction and development of the improvements based on medical results and data taken by experiments. Establishing a functional and save environment for the experiments to take place is the first task, it's no secret that for the improvements to be successful the equipment and the environment are going to play a crucial point. The first challenge is to keep the condition in which the improvement is going to be implemented as unchangeable as possible because the results have to be as close to the real environment as possible. After that the types of medical centrifuge difference by the type of mechanisms used in the current hospitals so the type of mechanism improved is the second problem that needs to be solved.

- *Evaluation of experimental results for different centrifuges and purposes for optimization.*
- *The author has done evaluation of experimental results for different centrifuges and purposes for optimization.*
- *Achieving a thorough experimental study experimental results for different centrifuges and purposes for optimization. In this paper the subject of simultaneous use of infrared thermography and EEG are investigated. Two different diagnostic methods are reviewed in terms of standard sessions.*

1. INTRODUCTION

Features that can quantify human gait play a major role in the studies of injury rehabilitation, improving athletic performance, and the design of prosthetic limbs. Human gait has long been an active area of research, and many system shave been proposed for observing gait irregularities. Thu sfar, most of these systems are based on image information from video sequences. When used in conjunction with biomechanical models, these features can allow quantitative analysis of many specific gait characteristics such as joint moments and powers (kinetic analysis), joint angles, angular velocities, and angular accelerations (kinematic analysis) [1].In these systems, optical markers are placed near anatomical landmarks of the body and features related to gait are extracted from video sequences. Parametric models have been used extensively to describe a set of image observations. An example is 3-D modelling of moving people which can be achieved by using volumetric bodies based on elliptical cylinders [2] [3].In general, methods that consider the use of kinematic constraints can handle more complex motions and occlusions. [4] use soft constraints in a hierarchical structural model of the human body to analyse video sequences captured in a home environment. Reviews on human motion analysis based on video, including summaries of modelling, tracking and recognition, are provided by Dariush [5] and Aggrawal et al.[6].

An alternative to vision based gait analysis is the use of body worn sensors to obtain motion data. The variables that can be measured during gait analysis depend on the technique selected. The most commonly measured variables include initial contact (IC) that defines the beginning of a complete gait cycle and thus cycle duration and frequency, and terminal contact (TC) that marks the start of the swing phase. Gyroscopes, which measure angular velocity, and accelerometers which measure linear acceleration, have been used as a wearable option to measure these variables [7] Coleman et al. [8], Aminian et al. [7] and Selles et al. [9] provide methods of measuring both TC and IC timing information. On the other hand, Yoshida et al. [10] use an accelerometer attached to the patient's waist and observe frequency peaks in the anterior plane to detect leg injury. In reality, however, injury causes changes in both the temporal and frequency domains and this variation is not normally limited to one direction of motion. After developing an experimental platform for studying the mechanical parameter of medical centrifuge we realized that the condition in which we conduct our experiment are not even supposed to be fixed. Why because you don't have fixed conditions in the pilot's cockpit, everything including: temperature, acceleration, air pressure, every condition is not constant. That why we conducted our experiments at free constantly changing environment. We basically left the same centrifuge conditions on open environment where every parameter was

unpredictable and change able as natural as it comes. Living the platform in open conditions with a test subject allowed us to discover one of the first possibilities for optimization temperature take big effect in how our vestibular system reacts. It plays a keen roll in how long it is going to take your vestibular system to require. The reason for that is very simple the fluid in your vestibular system contracts depending on that temperature.



Figure 1: Medical centrifuge experiments conducted in open field with life test subject subjected to different temperatures by day and night.

The M7 is dedicated to processing and translating the inputs provided to it by the discrete sensors; the gyroscope and electrometer and electromagnetic compass mounted throughout the main printed circuit for the accelerometer and the gyroscope while the electromagnetic compass would again be Asahi to be STMicroelectronics. But to our surprise the accelerometer is actually a design win for Bosch Sensor tech with their BMA220 3-axis accelerometer (the first Bosch we've ever seen in an Apple product). We dive deeper into the M7 and it's children in the next section. The previously unknown MEMS devices that had us so interested when we first cracked open the iPhone 5s one with marking B361LP and another B320. The first is a 3-Axis Accelerometer. Based upon the die mark-

ings observed in the 2mm x 2mm device, the first unknown MEMS device has been ID'd as a Bosch Sensor tech BMA220 3-axis accelerometer. This is the first time in our experience looking at Apple products that we see a Bosch! The second is a 3-Axis Gyroscope. The device with package marking B329 has been identified as an STMicroelectronics 3 – axis gyroscope, as expected. Holding the compass socket for another round is AKM's AK8963 3-axis electronic compass IC. The AK8963 combines a magnetic sensors to detect X, Y, and Z axis, a sensor driving circuit arithmetic and signal amplifier.

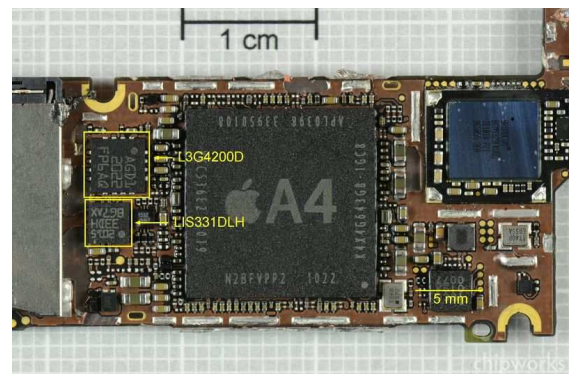


Figure 2: The AK8963 combines a magnetic sensors to detect X,Y, and Z axis. {Model 1}

Developing and wiring a special program along with a wireless transfer system was one of our biggest challenges, yet Apple did provide most of the solutions. Unfortunately it didn't provide all the solutions for us. So we developed our own personal software and equipment for wireless transfer of mechanical parameters. [1]



Figure 3: System for data re of mechanical parameters {Model 2}

The electronic management system and collecting information Rotostol 1 consists of the following components:

Access point Server /controller Server/ controller software for 32 clients gTouchpad is an open touchpad project aimed at comfort, low latency, and portability. All touchpad functionality is implemented in JavaScript and HTML5, which makes it very easy to implement new features or modify existing. The server side consists of a high performance, multi-threaded WebSocket server implemented in C++. The server supports hundreds of parallel connections. Scrolling and zooming is adapted to the currently active program, giving a smooth and comfortable experience in any program. The software supports auto-reconnection, no user action is needed if the server program gets restarted. – Software developed by from Eng. Dokt. Georgi Valkov



Figure 3: System for wireless transfer of mechanical parameters. {Model 3}

2. EXPERIMENTAL SETUP

Earlier in the day we established from the look of the die that the A7 was manufactured by Samsung. In the meantime our guys have been grafting away in the lab, and came to the “boring” conclusion that the chip looked exactly the same as the last one. The devil is in the details, however, and we have to do some measurements to see the difference. Below is an electron microscope image of a cross-section of a group of the transistors in the A6 (APL0598) chip, fabbed in the Samsung 32-nm high-k-metal gate (HKMG) process. For convenience we have measured ten, so the dimension of the “contacted gate pitch” (a standard industry measure) is 123 nm. Now if we look at a similar image of the A7 (APL0698), and we see that the contacted gate pitch is 114 nm. So, even allowing

for measurement error (we figure $\pm 5\text{nm}$), we're pretty sure that we see a shrink, and that the A7 is made on the same process as the new Samsung Exynos 5410, the 28 – nm HKMG process. That doesn't sound much a mere 4 nm, but again if you do the math and remember that we're talking area shrink, not linear dimensions, then 28^2 divided by 32^2 ($784/1024$) comes out at about 77% of the area for functions in a slightly bigger area.

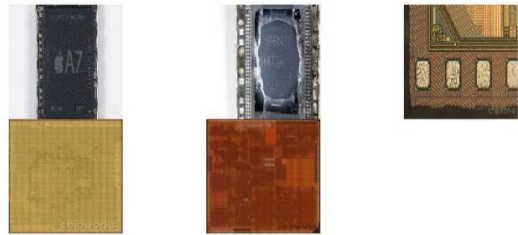
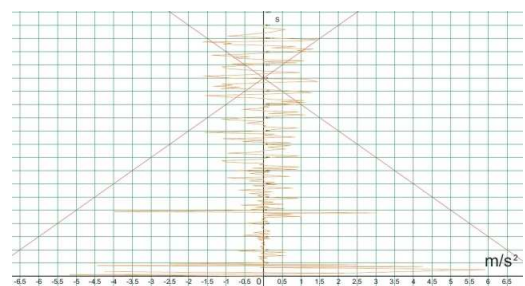
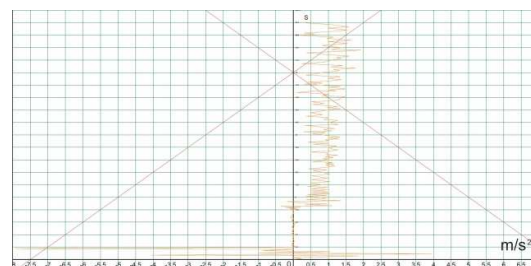


Figure 4: A7 Processor {Model 4}

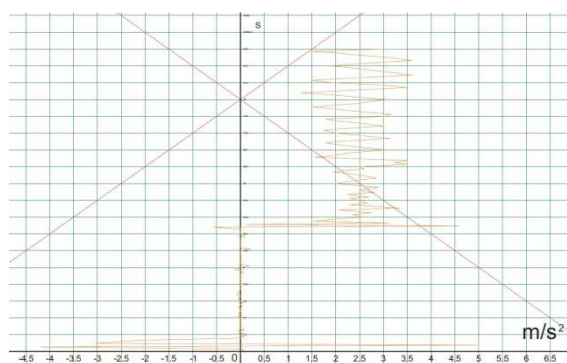
From the experimental results we took in constantly changing conditions the acceleration charts give us good visual idea of what is going on with fluid in the inner ear of the vestibular system. [11] Experimental results for the axis X, Y, Z with medical centrifuge the data was collected in real life conditions with live test subject. The constantly changing acceleration has a tremendous effect over our sense of balance what we have managed to learn so far is that the conditions and temperature on with it actors and on which we restore our sense of balance played a crucial role to our regeneration and restoring time for our sense of balance. The acceleration conditions established by experiments with live test subject are:



(A) The acceleration change over X for 1 min duration.



(B) The acceleration change over Y for 1 min duration.



(C) The acceleration change over Z for 1 min duration.

Figure: 5 Experimental results of medical centrifuge with life test subject

3. CONCLUSIONS

Instead of defining pre-fixed parameters that can distinguish injured from normal walking, an automatic feature selection method was proposed using the Discrete Wavelet Transform for feature extraction, and the Iterative Search Margin Based algorithm for feature selection. The results on data collected from 2 datasets of impaired gait show a good separation between classes, especially with the use of ICA to perform source separation on the wavelet features before the feature selection stage. The method also performs well when different subjects with varying walking patterns and speeds are combined together. The observation of data from a patient with a leg injury shows a good separation between classes. It also shows that the features obtained can be observed to indicate recovery. A further extension of this work could include the study of the relationship between the time-frequency features extracted and those used traditionally by gait-analysis labs (such as initial and terminal contacts), as well as validating results with vision based techniques. It would also be interesting to investigate the use of wearable sensors for observing the progress of some diseases that affect walking patterns, such as Parkinson's disease.

ACKNOWLEDGMENTS

The research described in this paper is supported by the Scientific Research Sector of TU-Sofia under the contract No 152nd0054-07

References

- [1] G. F. Harris and J. J. Wertsch, Procedures for Gait Analysis. Arch Physical Medicine and Biology, 1994. 75(2): p. 216-225.
- [2] D. Hogg, Model based vision: A program to see a walking person. Image Vis. Comput., 1983. 1(1): p. 5-20.
- [3] M. Isard and A. Blake, on densation-Conditional density propagation for visual tracking, Int. J. Comput. Vis., 1998.29(1): p. 5-28.
- [4] S. L. Dockstader, M. J. Berg, and A. M. Tekalp, Stochastic kinematic modeling and feature extraction for gait analysis. Image Processing, IEEE Transactions on, 2003. 12(8): p. 962-976.
- [5] B. Dariush, Human motion analysis for biomechanics and biomedicine. Machine Vision and Applications, 2003. 14(4):p. 202-205.
- [6] J. K. Aggrawal, and Q. Cai, Human motion Analysis: A review. Comput. Vis. Image Understanding, 1999. 73(3): p.428-440.
- [7] K. Aminian, et al., Temporal feature estimation during walking using miniature accelerometers: an analysis of gait improvement after hiparthroplasty. Med Biol Eng Comput, 1999. 37(6): p. 686-91.
- [8] K. L. Coleman et al., Step Activity Monitor: Long Term Continuous Recording of Ambulatory Functions. J. Rehab. Res. Develop., 1999. 36(1): p. 8-18.
- [9] R. W. Selles et al., Automated estimation of initial and terminal contact timing using accelerometers; development and validation in transtibial amputees and controls. Neural Systems and Rehabilitation Engineering, 2005. 13(1): p. 81-88.
- [10] T. Yoshida, et al. Gait Analysis for Detecting a leg accident with an accelerometer. in 1st Distributed Diagnosis and Home Healthcare (D2H2) Conference,. 2006. Virginia, USA.
- [11] Experimental study of existing centrifuges in real hospital conditions Tsvetan Kachamachkov , V. Manoev, D. Dimitrov Technical University of Sofia.

EXPERIMENTAL STUDY OF EXISTING CENTRIFUGES IN REAL HOSPITAL CONDITIONS

Tsvetan Kachamachkov, V. Manoev, D. Dimitrov

8, Kl. Ohridski, Sofia, Bulgaria, TU-Sofia,
Postal Sofia - 1309,,Sv. Troitsa" 303 - B - 39

Abstract

The taking of the data is going to be in real conditions with patients and doctors to monitor the necessary functions of the body after establishing some data we will conducted experiments based on the conditions and mechanisms to see how that affects the end results the gathering of the data will be conducted with human participants and life experiment conditions so the third problem that we have to take in to care is the human safety during the experiments. The hospitals provide the necessary environment for the experiments and for the adjustments of the equipment but we have to take into care that the experiments will be on different human subjects and that this conditions will take effects on the parameters in the experiments. The real challenge is going to be taken into care the difference of the mechanisms types which are going to affect the medical centrifuge and the constantly changing conditions in which the experiments are going to take place.

- Experimental study of existing centrifuges in real hospital conditions.
- The author has done experimental study of existing centrifuges in real hospital conditions.
- Achieving a thorough experimental study of existing centrifuges in real hospital conditions.

1. INTRODUCTION

The electronic management system and collecting information Rotostol 1 consists of the following components:

Access point Server / controller Server / controller software for 32 clients gTouchpad is an open touchpad project aimed at comfort, low latency, and portability. All touchpad functionality is implemented in JavaScript and HTML5, which makes it very easy to implement new features or modify existing. The server side consists of a high performance, multi-threaded WebSocket server implemented in C ++. The server supports hundreds of parallel connections. Scrolling and zooming is adapted to the currently active program, giving a smooth and comfortable experience in any program. The software supports auto-reconnection, no user action is needed if the server program gets restarted. – Software developed by from Eng. Dokt. Georgi Valkov

2. EXPERIMENTAL SETUP

For a full testament of the vestibular system it is required a complex axis rotation and translation configuration way too expensive and unnecessary for any hospital.

Studies show that it's not necessary to much to provoke the same effect that Complex system for vestibular testing is causing actually it's only necessary to create an angle between 0 - 45 degree. Nasa has developed a unique solution to the ne-

cessity of angular movement the economical solution for special vestibular system testing the solution provides incomplete test and it still is being implemented because of economic necessity.

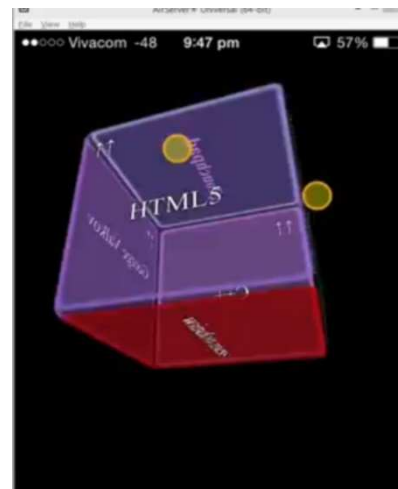


Figure 1: Wifi Client software for Iphone 5S 16
GbArchiver/convertor software

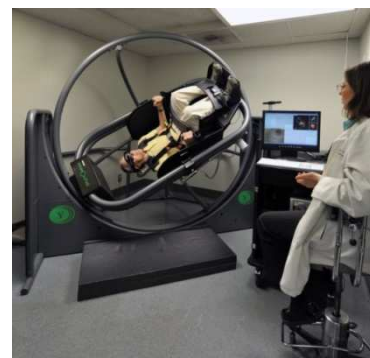


Figure 2: Complex system for vestibular testing



Figure 3: Normal system for vestibular testing usually found in hospital

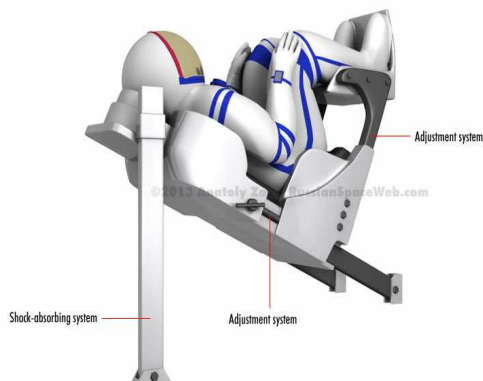
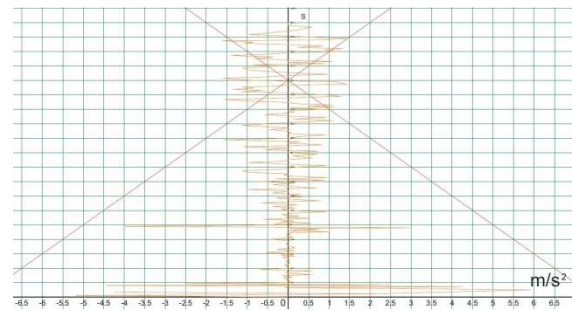
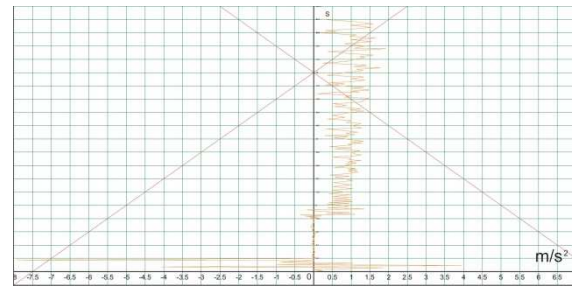


Figure 4: Nasa 45 degree angular platform

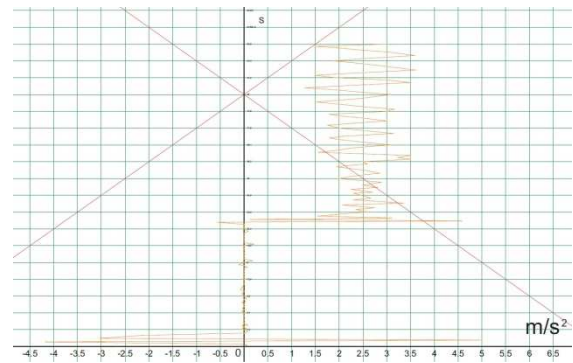
Experimental results for the axis X, Y, Z with medical centrifuge the data was collected in real life conditions with live test subject. The constantly changing acceleration has a tremendous effect over our sense of balance what we have managed to learn so far is that the conditions and temperature on with it actors and on which we restore our sense of balance played a crucial role to our regeneration and restoring time for our sense of balance. The acceleration conditions established by experiments with live test subject are:



(A) The acceleration change over X for 1 min duration.



(B) The acceleration change over Y for 1 min duration.



(C) The acceleration change over Z for 1 min duration.

Figure 5: Experimental results of medical centrifuge with life test subject Type 1 medical centrifuge.

The basic equations for most centrifugal modelling were introduced. The liquid drag force was given in equation, under streamline flow, and the centrifugal field force was provided in equation. It is a simple matter to equate these to arrive at an analogue equation to the terminal settling velocity, equation, but with one significant difference the distance with time differential is not constant. In a centrifugal field the particle moves radially, see Figure 4 and the radial position is part of the field force – hence the particle accelerates during its travel in the radial direction. Thus, to determine the particle position as a function of time integration is required.

It is well known that from a strict physical definition of forces on a particle, in circular motion, the centripetal force and not the centrifugal force should be considered. An unrestrained particle would leave its orbit tangentially if the centripetal force was suddenly removed. However, this chapter is con-

cerned with separation of particles in rotating flow within a viscous medium, usually water. The particle will not travel tangentially to one orbit, but to lots of orbits, giving the impression of radial movement outwards (provided the particle is denser than the surrounding continuous phase). Mathematically, we can use the well-known expressions, such as equations and, to describe this travel.

$$\frac{dr}{dt} = \frac{x^2(p_s - p)r\omega^2}{18\mu} \quad (1)$$

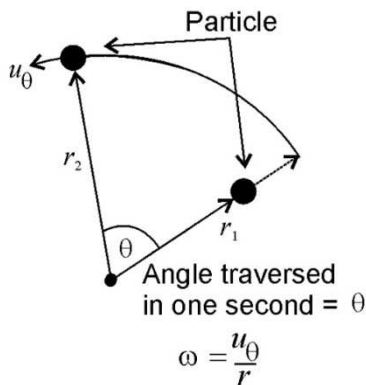


Figure 6: Particle in rotation and definitions.
Type 2 medical centrifuge

As illustrated in Figure 8.1, the centrifugal acceleration is simply the product of the radial position (r) and the square of the angular velocity (ω). The SI units of angular velocity are s^{-1} , but calculated by converting from revs per minute (rpm) into radians per second – then ignoring the dimensionless radian term. In solid body rotation, such as a centrifuge, this is easily calculated from the rotational speed, usually provided in rpm. Thus, 1 rpm is $2\pi s^{-1}$ as an angular velocity. In free body rotation, such as the hydrocyclone, the angular velocity is calculated from the tangential velocity U_θ by $\omega = U_\theta / r$ this is also illustrated on Figure 4. In the hydrocyclone the principle known as the conservation of angular momentum is used; in

which knowledge of the tangential velocity at any radial position can be used to calculate the tangential velocity at another because $U_{\theta 1} r_1 = U_{\theta 2} r_2 = \text{constant}$ or to take account of frictional losses within the hydrocyclone $U_{\theta 1} r_1^{n''} = U_{\theta 2} r_2^{n''} = \text{constant}$ where n'' is an empirical constant, usually between 0.6 and 1.

In filtration within a centrifugal field the body force acts on the liquid, which can pass through the filter medium, or septum, similar to a washing machine or spin drier. The rotation acts in a similar way as increasing the pressure effecting the filtration and it is possible to deduce what this equivalent pressure difference is, using an equation analogous to that given by the static component of Bernoulli's equation (depth \times density \times acceleration)

$$\Delta P_{CH} = p\omega^2(r_o^2 - r_L^2)/2 \quad (2)$$

where r_o is the radius of the centrifuge and r_L is the inner liquid radial position and ΔP_{CH} is sometimes called the centrifugal head. From all of the above, it should be apparent that modification for an enhanced body force due to rotation is simply required. Phone in-hand, we did what any self-respecting technology company would do – destroy it (carefully). Follow us along today as we dive into what's new and exciting this time around, including the A7 64-bit ARM CPU and the mysterious M7 motion co-processor. At first glance we're seeing a lot of familiar components with the major standouts being the new A7 processor and two new MEMS devices. We are also seeing a new power management IC by Dialog Semiconductor and a new audio codec and class D amplifier by Cirrus Logic. The M7 is a new direction for Apple – in an effort to reduce power consumption, the M7 chip is dedicated to collecting and processing accelerometer, gyroscope and compass data. That being said, the M7 has been a difficult chip to locate on the board and rumors have been going about the lack of a discrete M7 chip inside the iPhone 5s. All expectations up to now were pointing to a stand-out chip as seen below at the Apple Town Hall event.

The accelerometer was tested using the rotational set up shown in figure 6. A small wheel is driven and connected by a lever with length L to a large wheel, on which the accelerometer is mounted. By driving the small wheel with a constant angular velocity the large wheel will show harmonic angular accelerations with constant amplitude and a fre-

quency depending on the angular velocity ω of the small wheel. The latter is driven by a motor. For angles θ with amplitudes smaller than about 30° , the motion of the wheel can be considered sinusoidally. Consequently, the angular acceleration $\alpha(t)$ of the big wheel becomes [1,2]

$$\alpha(t) \approx -\omega^2 \eta \sin \quad (3)$$

where η is a geometrical constant that depends on R , H , G_x , G_y and L .



Figure 7: 7 M7 chip inside the iPhone 5s

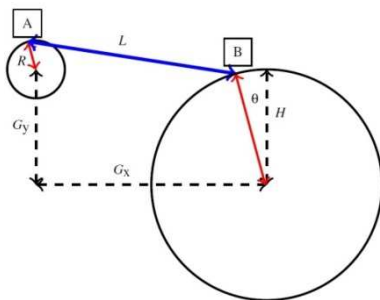


Figure 8: Schematic overview of the rotational setup. [3]
Type 3 medical centrifuge

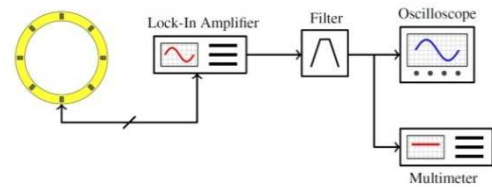


Figure 9: Experimental setup for measurement of the output bridge voltage. [4,5]

CONCLUSIONS

As a conclusion in critical aspect proves to compensate for the lack of angular acceleration by comparing all 3 types of medical centrifuges we conclude that a hybrid is needed for angular acceleration. An angular accelerometer based on the semicircular channels of the vestibular system is developed. The accelerometer consists of a water-filled tube, wherein the fluid velocity is measured thermally as are presentative for the angular acceleration.

ACKNOWLEDGMENTS

The research described in this paper is supported by the Scientific Research Sector of TU-Sofia under the contract No 152nd0054-07

References

- [1] C. Fernández and J. M. Goldberg, "Physiology of peripheral neurons innervating semicircular canals of the squirrel monkey. II. Response to sinusoidal stimulation and dynamics of peripheral vestibular system," *J. Neurophysiol.*, vol. 34, no. 4, pp. 661–675, Aug. 1971.
- [2] J. J. Groen and L. B. W. Jongkees, "The threshold of angular acceleration perception," *J. Physiol.*, vol. 107, pp. 1–7, 1948.699.
- [3] J. Haneveld, T. S. J. Lammerink, M. J. de Boer, R. G. P. Sanders, A. Mehendale, J. C. Lötters, M. Dijkstra, and R. J. Wiegerink, "Modeling, design, fabrication and characterization of a micro Coriolis mass flow sensor," *J. Micromech. Microeng.*, vol. 20, p. 125001, 2010.
- [4] ST Microelectronics, "LIS1R02 (L6671)," 2002, Angular accelerometer.
- [5] Endevco, "Model 7302BM4 – Piezoresistive angular accelerometer," 2009

MATHEMATICAL ANALYSIS OF HOW SPINNING UNDER AN ANGLE AFFECTS THE VESTIBULAR SYSTEM OF PILOTS

Tsvetan Kachamachkov

8, Kl. Ohridski, Sofia, Bulgaria, TU-Sofia,
Postal Sofia - 1309, Sv. Troitsa" 303 - B - 39

Abstract

One typical example of high-genus anatomical structures is called the vestibular system (VS) (see Figure 3). The VS is a genus-3 structure situated in the inner ear, which is a sensory structure responsible for detecting head movements and sending postural signals to the brain. The morphometry of VS plays an important role in the analysis of various diseases such as the Adolescent Idiopathic Scoliosis (AIS) disease. The AIS is a 3D spinal deformity which affects about 4% school children world wide. The etiology of AIS is still unclear but believed to be a multi-factorial disease. One popular hypothesis was suggested to be the structural changes in the VS that induce the disturbed balance perception, and further cause the spinal deformity. The morphometry of the VS becomes important to understand the disease.

- Mathematical analysis of how spinning under an angle affects the vestibular system of pilots.
- The author has made a mathematical analysis of how spinning under an angle affects the vestibular system of pilots.
- Achieving a thorough overview of mathematical analysis of how spinning under an angle affects the vestibular system of pilots.

1. INTRODUCTION

Zero gravity was a feature first introduced by NASA to explain what they found to be the optimal seating position for astronauts who were spending a good amount of their time strapped into their seat in their spaceship as it orbited the earth. This becomes apparent when you sit in a normal chair, with a normal horizontal seat and with a chair back that is either reclined or inclined, and then put the chair into a zero gravity position. If you focus on how your low back feels in both positions, you will become very aware of the additional "weight" or compression on the low back when the seat is horizontal. When the zero gravity positioning is introduced, you will suddenly become aware that the weight or compression on the low back shifts and now feels more evenly distributed throughout the whole body. The behaviour of the gyroscope is naturally described Figure 4. Schematic illustration of a MEMS implementation of the z-axis rate integrating gyroscope with respect to the non-inertial coordinate frame $\{x; y; z\}$. In this case, the governing equations in Cartesian coordinates $\{x; y; z\}$ are given by

$$X'' + \omega_n^2 X - 2\Omega Y' = 0 \quad (1)$$

$$Y'' + \omega_n^2 Y - 2\Omega X' = 0 \quad (2)$$

The essential feature of these equations is the presence of the Coriolis acceleration terms $-2\Omega Y'$ and $-2\Omega X'$. It is the Coriolis acceleration that causes a transfer of energy between the two gyro-

scope modes of operation. The resultant Coriolis force is perpendicular to both the input rate and the instantaneous radial velocity in the drive direction. This produces a motion of the proof mass in direction perpendicular to its initial oscillation. To measure rotation rate, the proof-mass is driven to a fixed amplitude along the x-axis by applying an electrostatic drive force to the proof-mass along the x-axis. In the absence of rotation there will be no motion of the proof-mass along the y-axis, (a). Under rotation, however, the Coriolis acceleration will cause energy to be transferred from the x-axis (primary mode) to the y-axis (secondary mode) building up a vibration amplitude along the y-axis. The ratio of the amplitude in the secondary mode of vibration to the amplitude of the primary mode of vibration can be shown to be proportional to the rotation rate and is given by [1]

$$\frac{Y}{X} = 2Q \frac{\Omega}{\omega_n} \quad (3)$$

Pilots have more developed vestibular system because of the constantly changing angle between 0 degree and 45 degree. There are some theories that spinning a human under this circumstances will help him develop a stronger and more evolved vestibular system. However there is no proof of these theories, which is one of the provocations for such a mathematical model and further studies in the field how spinning under different angles affects our vestibular system. 45 degree is not cho-

sen by a coincidence at this particular angle most of the pilot simulations work. Creating a mathematical model of these particular circumstances could be the key to unlocking the hidden human potential and developing our vestibular systems even farther. Maybe math will reveal the hidden secrets of the human vestibular system. I hope that number will answer that which has left the medicine speechless.

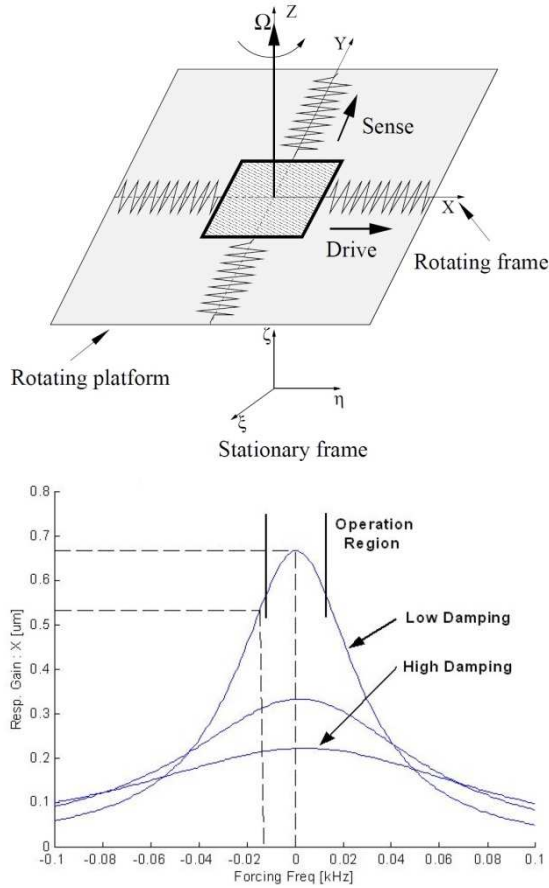


Figure 1. (a) Mass-spring model of the vibratory micromachined gyroscope; (b) The response of the vibratory gyroscope to the Coriolis force. [2]

2. EXPERIMENTAL SETUP

Additionally, time dependent vector fields can be used to represent the set of all surface maps. Joshi and Miller [1] proposed the generation of large deformation diffeomorphisms for landmark matching, where the registrations are generated as solutions to the transport equation of time dependent vector fields. Most of the existing algorithms for surface registration and shape analysis can only deal with simply-connected open or closed surfaces. Analyzing high-genus surfaces is generally challenging because of their complicated topologies. Recently, some works have been carried out to

register and analyze high-genus surfaces. Zeng et al. [2] proposed to measure the geodesics spectra on VS

$$ds^2 = \frac{dx^2 + dy^2}{(1 - x^2 - y^2)} \quad (4)$$

In fact, S can be sliced open along the canonical homotopic basis $\{a_1, b_1, \dots, a_g, b_g\}$ of the fundamental domain $\pi(S, p)$ at a point $p \in S$, for which any two loops of the basis intersect only at p (see Figure 1(A)). Slicing along the basis, we get a simply-connected open surface S^{cut} is given by $a_1 b_1 a_1^{-1} b_1^{-1} \dots a_g b_g a_g^{-1} b_g^{-1}$. S^{cut} can then be conformally parameterized 1-1 and onto a domain $D_i \cap H$, which is called a fundamental polygon (see Figure 1(B)). Denote the parameterization by $\tilde{\pi}: S^{cut} \rightarrow \tilde{D}_i$. The edges of \tilde{D}_i satisfy the periodic boundary conditions.

More specically, there exist *Möbius* transformations $\{\varphi_1, \phi_1, \dots, \varphi_g, \phi_g\}$ (called the Fuchsian group generators) such that:

$$C + \varphi_i(\tilde{\pi}(a_i^{-1})) = \tilde{\pi}(a_i^{-1}); \quad \phi_i(\tilde{\pi}(b_i)) = \tilde{\pi}(b_i^{-1}) + C \quad (5)$$

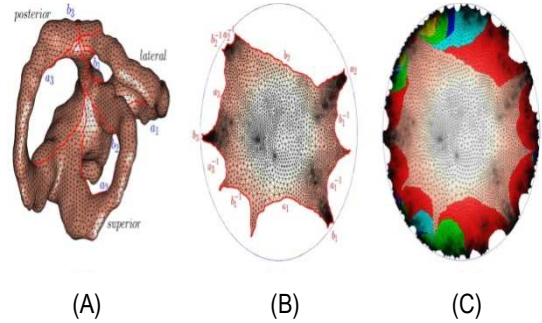


Figure 3: (A) shows a vestibular system (VS) surface. (B) shows its fundamental polygon in the hyperbolic disk. (C) shows the universal covering space of the VS surface.

By gluing in_finitely many copies of \tilde{D}_i to together along its boundaries, we get the Poincare disk H . $\tilde{\pi}$ is extended to a surjective map $\tilde{\pi}: H \rightarrow S$, which is called the covering map, satisfying

$$\tilde{\pi}^{-1}(S) = \bigcup_{i \in I} \tilde{D}_i \quad (6)$$

where \tilde{D}_i and \tilde{D}_j intersects only at the edges of the fundamental polygon (see Figure 2(C)). Let Ω_1 and Ω_2 be 2D domains. Every diffeomorphism $f: \Omega_1 \rightarrow \Omega_2$ is associated to a unique Beltrami coefficient (BC), which measures the conformality distortion of the $f := u + iv$. Here, we consider f as a complex-valued function on Ω_1 . The BC,

$\mu : \Omega_1 \rightarrow C$ can be computed by the following equation:

$$\mu(x, y) = \left(\frac{df}{dx} + i \frac{df}{dy} \right) / \left(\frac{df}{dx} - i \frac{df}{dy} \right) \quad (7)$$

Given a smooth $BC\mu : C \rightarrow C$ with $\|\mu\|_\infty < 1$. There is always a diffeomorphism of C that satisfies the equation (4) [3]. However, suppose Ω_1 and Ω_2 are arbitrary domains and extra constraints (such as landmark constraints) are enforced. Then, an arbitrary $BC\mu : \Omega_1 \rightarrow C$ may not be associated to a diffeomorphism $f : \Omega_1 \rightarrow \Omega_2$ subject to the extra constraints. In this case, a BC is called admissible if it is associated to a quasi-conformal map subject to the given constraints. In this work, we use BC s to control the bijectivity of the mappings [4]. In this work, we propose to extract two geometric features for shape analysis. They are: (1) homotopic loops [5] and (2) minimal surfaces. These features can be used to understand the geometric patterns of the VS surfaces. With the registration, we can compute the mean shape of the VS surfaces. Denote the genus-3 VS mean surface by S_{mean} . A homotopic basis based at a point p on the surface can be extracted. By cutting along the homotopic basis, S_{mean} becomes a simply-connected open surface. S_{mean} can be embedded into its universal covering using Ricci flow. On the universal covering space, we can easily find a canonical homotopic basis $\{a_1, b_1, a_2, b_2, a_3, b_3\}$, which intersects only at the base point p and are all hyperbolic geodesic. For each point q on the curve a_i ($i = 1, 2$ or 3), we can find a geodesic closed loop $C_q : [0, 1] \rightarrow S_1$ such that $C_q(0) = C_q(1) = q$. The geodesic loop $C_q(t)$ solves the following minimization problem:

$$C_1(t) = \argmin_{\gamma(t)} \int_0^1 \sqrt{g_{\gamma(t)}(\gamma'(t), \gamma'(t))} dt \quad (8)$$

all closed loop $\gamma(t)$ satisfying $\gamma(0) = \gamma(1) = q$. The collection of all loops $C_q(t)$ situated at q on a_i ($i = 1, 2$ or 3) are called the homotopic loops. These homotopic loops belong to the equivalence class $[a_i]$ of the homotopic group. Using the obtained registration between the mean surface and any VS surface, corresponding homotopic loops can be delineated on each VS surface. Let S be any VS surface. Suppose $f : S_{mean} \rightarrow S$ is the registration between S_{mean} and S . The corresponding homotopic loops on S can be easily obtained

by $C_q^S := f \circ C_q : [0, 1] \rightarrow S$. These homotopic loops can be used to study the local geometry and thickness at each position of the VS surface. From the homotopic loops, the center lines can be extracted. Let $\{C_q^S\}_{q \in a_i}$ be the collection of all homotopic loops on one canal of the VS surface S . For each homotopic loop, we can compute its centroid. By joining all the centroids, we can obtain a curve lying in the interior of one canal of S . This curve is called the center line. [6, 7] Using the center line, bendings of the canal can be examined. Each canal of the VS surface can roughly be fitted to a plane. And the three planes are roughly orthogonal to each others. [6, 7] To study AIS, it is commonly of interest to examine how each canal is deviated from a plane. Let $\vec{c} = \vec{c}(t)$ be parametric equation of the center line. We can find a best fit plane $P : \vec{n} \cdot (x, y, z) = \lambda$ to the center line by minimizing:

$$E(\vec{n}, \lambda, \vec{c}) = C + \int_0^1 D(\vec{n}, \lambda, \vec{c}(t))^2 dt$$

This formula has been developed and added personally. (9)

where $D(\vec{n}, \lambda, \vec{c}(t))$ is the distance of the point $\vec{c}(t)$ from the plane $P : \vec{n} \cdot (x, y, z) = \lambda$. The distance $D(\vec{n}^*, \lambda^*, \vec{c}(t))$ of the point $\vec{c}(t)$ from the best fit plane can be used to measure the deviation of the canal from a plane at each point of the center line. Once the homotopic loops on each canal of the VS is extracted, we can compute the minimal surfaces enclosed by each homotopic loops. With the minimal surfaces, cross-sectional area at each position of the canals can be evaluated. [8, 9] Minimal surfaces are defined as surfaces which are critical points for the area functional. Suppose the homotopic loop l is projected orthogonally to a convex curve enclosing a domain D in a plane. The minimal surface is a graph of a function: $z = u(x, y)$, where x and y are the coordinates on the plane (see Figure 3(A)). Suppose the homotopic loop is given by $l = l(x, y)$ for $(x, y) \in dD$. The function $u(x, y)$ of the minimal surface satisfies the following Euler-Lagrange equation:

$$C + \nabla \cdot \left(\frac{\nabla u}{\sqrt{1 + |\nabla u|^2}} \right) = 0 + C \quad (9)$$

subject to the constraint that: $u|_{dD}(x, y) = l(x, y)$. In this work, the minimal surface is computed by solving equation using the finite element

method. Figure 3(B) shows the minimal surfaces enclosed by the homotopic loops of a standard 3-torus. [9]

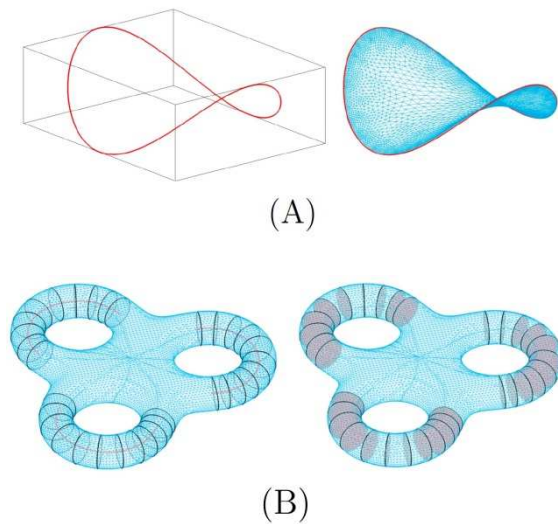


Figure 4: (A) shows a space curve (left) and minimal surface enclosed by the space curve(right). (B) left shows the homotopic loops and centerlines of a 3-torus, right shows the minimal surfaces enclosed by the homotopic loops.[10,11,12]

CONCLUSIONS

An angular accelerometer based on the semicircular channels of the vestibular system is developed. The accelerometer consists of a water-filled tube, wherein the fluid velocity is measured thermally as a representative for the angular acceleration. Measurements show a linear response for acceleration amplitudes up to $2 \times 10^5 \text{ s}^{-2}$.

ACKNOWLEDGMENTS

The research described in this paper is supported by the Scientific Research Sector of TU-Sofia under the contract No 152пд0054-07

References

- [1] A. Shkel, R. Horowitz, A. Seshia, S. Park and R. T. Howe. Dynamics and control of micromachined gyroscopes. The American Control Conference, June 1999. San Diego, CA.
- [2] C. Fernandez and J. M. Goldberg. Physiology of Peripheral Neurons Innervating Semicircular Canals Of The Squirrel Monkey. II. response to sinusoidal stimulation and dynamics of peripheral vestibular system. J. Neurophysiol, 34:661{675, 1971.
- [3] L. Shi, D. F. Wang, W. C. W. Chu, G. R. Burwell, T. T. Wong, P. A. Heng, J. C. Y. Cheng, Automatic mri segmentation and morphoanatomy analysis of the vestibular system in adolescent idiopathic scoliosis, Neuroimage 54 (2011) S180{S188.
- [4] L. M. Lui, C. F. Wen, Geometric registration of high-genus surfaces, Siam Journal on Imaging Sciences 7 (1) (2014) 337{365.
- [5] F. P. Gardiner, N. Lakic, Quasiconformal Teichmuller theory, Mathematical surveys and monographs,, American Mathematical Society, Providence, R.I., 2000.
- [6] L. M. Lui, K. C. Lam, T. W. Wong, X. F. Gu, Texture map and video compression using beltrami representation, Siam Journal on Imaging Sciences 6 (4) (2013) 1880{1902.
- [7] L. M. Lui, K. C. Lam, S. T. Yau, X. F. Gu, Teichmuller mapping (t-map) and its applications to landmark matching registration, Siam Journal on Imaging Sciences 7 (1) (2014) 391{426.
- [8] M. Jin, J. H. Kim, F. Luo, X. F. Gu, Discrete surface ricci ow, Ieee Transactions on Visualization and Computer Graphics 14 (5) (2008) 1030{1043.
- [9] S.-Q. Xin, Y. He, C.-W. Fu, D. Wang, S. Lin, W. C. Chu, J. C. Cheng, X. Gu, L. M. Lui, Euclidean geodesic loops on high-genus surfaces applied to the morphometry of vestibular systems, in: Medical Image Com-34 puting and Computer-Assisted Intervention{MICCAI 2011, Springer, 2011, pp. 384{392.
- [10] T. Haumont, G. C. Gauchard, P. Lascombes, P. P. Perrin, Postural instability in early-stage idiopathic scoliosis in adolescent girls, Spine 36 (13) (2011) E847{E854.
- [11] N. N. Byl, S. Holland, A. Jurek, S. S. Hu, Postural imbalance and vibratory sensitivity in patients with idiopathic scoliosis implications for treatment, Journal of Orthopaedic & Sports Physical Therapy 26 (2) (1997) 60{68.
- [12] M. D. Malinzak, R. F. Kay, T. E. Hullar, Locomotor head movements and semicircular canal morphology in primates, Proceedings of the National Academy of Sciences of the United States of America 109 (44) (2012) 17914{17919.

IMPLEMENTATIONS FOR MEMS IN THE VESTIBULAR SYSTEM

V. Manoev, Ts. Kachamachkov

Technical University of Sofia, Bulgaria
Faculty of Telecommunication, TU-Sofia, "Kl. Ohridsky" str. 8, 1000 Sofia, Bulgaria
E-mail: vmanoev@outlook.com

Abstract

This paper presents a feasibility study on an MEMS based implantable vestibular prosthesis. Our end-goal is to design a prosthesis that will replace the function of the damaged vestibular end-organ by providing an MEMS chip that will accurately sense, extract, and transmit 3-dimensional motion information for people who have permanently lost peripheral vestibular function. The prosthesis prototype includes orthogonal triad of accelerometers and gyroscopes on-a-single finger a sized chip. Based on physiological data on perceptual thresholds of linear acceleration and angular velocity in humans, we conclude that the MEMS technology is a viable candidate for such an implant. Functional architecture for the vestibular prosthesis is introduced.

- Implementations for mems in the vestibular system.
- The author has made a thorough research of existing implementations.
- Achieving a thorough overview of current implementations for mems in the vestibular system.

1. INTRODUCTION

The primary function of the vestibular system is to provide the brain with information about the body's motion and orientation. The absence of this information causes blurred vision (oscillopsia), balance difficulties, and spatial disorientation, vertigo, dizziness, imbalance, nausea, vomiting, and other symptoms often characterize dysfunction of the vestibular system. The symptoms may be quite mild, lasting minutes, or quite severe, resulting in total disability [1]. Sensory prostheses to artificially replace lost sensory function for a number of sensory systems are currently under investigation. For example, cochlear implants use electrical stimulation to restore hearing, providing some relief for patients suffering from profound sensorineural hearing loss [2]. Using similar principles, a vestibular prosthesis could provide head orientation information to the nervous system for patients suffering from peripheral vestibular disorders. At least two categories of vestibular prosthesis might be considered. One approach is to provide the head movement information to the nervous system directly by electrically stimulating the vestibular neural pathways related to spatial orientation. An other approach is to provide the information via sensory substitution through other sensory systems (e.g., tactile, visual, auditory, etc.) [3]. This work falls in the first category. Our goal is to develop an implantable, vestibular neural prosthesis using electrical stimulation. To the best of our knowledge, there is only one group working on neural semicircular canal prosthesis [4,

5]. This group has already reported successful interface of the device with vestibular neurons. The group uses an off-the-shelf single axis piezoelectric vibrating gyroscope to measure the head rotation and to provide corresponding stimulus to the nervous system. The group reported experimental results on an animal model of guinea pigs, in which the gyroscope was mounted externally to the animal's skull using small bolts and miniature stainless-steel screws. Microcontroller was used to convert rotational information into electrical pulsatile stimulus. [6]

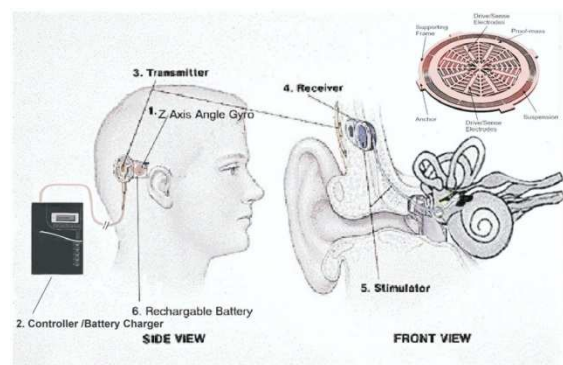


Figure 1. A conceptual model of a totally implantable vestibular prosthesis. The implant is based on 3-axes micro-size gyroscopes integrated alongside with signal conditioning electronic on the same silicon chip

The device includes three main functional units – a sensing unit, a pulse generator, and a stimulator. The device also includes two supporting units: a power supply and an external controller and charging unit. The sensing unit includes 3-axis accelerometers and 3-axis gyroscopes. These devices

es sense linear and angular motion of the head and generate voltages proportional to the corresponding linear acceleration and angular velocity. Then, voltages are sent to the pulse generating unit where angular velocities (or linear accelerations) are translated into voltage pulses. In the stimulator, the voltage pulses are converted into current pulses and are delivered through specially designed electrodes to stimulate the corresponding vestibular nerve elements. Each functional block of the chip consumes electrical power. For long term autonomous operation of the implantable device, it is required to supply power externally. Additionally, the implant should be able to communicate with an external controller and charging unit.

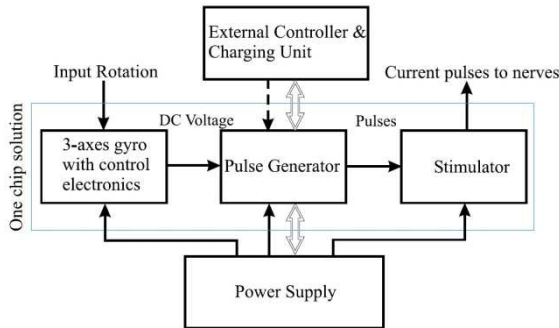


Figure 2. Functional diagram of the vestibular implant [7]

2. EXPERIMENTAL SETUP

The MEMS accelerometer consists of a proof mass suspended by compliant beams anchored to a fixed frame. External acceleration due to motion of the object to which the sensor's frame is attached, displaces the support frame relative to the proof mass, which in turn, changes the initial stress in the suspension spring. Both this relative displacement and the suspension-beam stress can be used as a measure of the external acceleration.

In the most general case, the proof-mass motion can have six degrees of freedom. But typically in a unidirectional accelerometer, the geometrical design of the suspension is such that one of these axes has low stiffness while high stiffness along other axes. For example, in case of the Z-axis accelerometer, the proof mass of the device will displace in out-of-plane of the chip only if there is an acceleration component along the z-axis. Our micromachined gyroscopes use vibrating element to measure rotational velocity based on the Coriolis principle [8]. Just like a linear accelerometer, the micromachined vibrating angular rate sensor con-

sists of a mass suspended on elastic supporting structures anchored to the substrate, Figure 3.

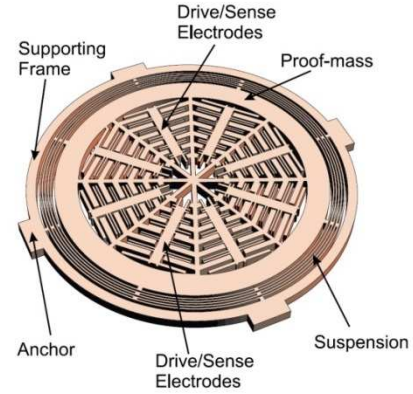


Figure 3. Schematic illustration of a MEMS implementation of the z-axis rate integrating gyroscope. [8]

$$P \left(\frac{d\vec{v}}{dt} + \vec{v} \cdot \nabla \vec{v} \right) = -\nabla p + \mu \nabla^2 \vec{v} + \vec{f} \quad (1)$$

[9] Where the terms on the left-hand side comprise inertial terms and where the terms on the right-hand side are depending on pressure, viscosity and body forces represented by \vec{f} . Since the fluid flow is inside a cylindrical channel, we will use cylindrical coordinates to describe the fluid dynamics. We assume that there are no pressure gradients in the circular channel ($\nabla p = 0$) and the flow-velocity is only non-zero in the axial direction z with component v and the tube radius is much smaller than the radius of the vestibular circular system R_c . A harmonic angular acceleration will lead to a body force density f in the axial direction:

$$f_z = P R_c \alpha_{ext} e^{i\omega t} \quad (2)$$

where α_{ext} is the amplitude of a harmonic angular acceleration with frequency ω . The Navier-Stokes equations in (1) can be simplified to

$$\mu \left[\frac{d^2 v}{dr^2} + \frac{1}{r} \frac{dv}{dr} \right] + f_z = 0 \quad (3)$$

for Reynold's numbers in the fully laminar flow regime [10]:

$$R_e = \frac{P V_0 d}{\mu} < 200 \quad (4)$$

To find a solution for the fluid velocity-profile $v(r, t)$, we assume a harmonic flow with a parabolic profile [11,12]:

$$v(r, t) = V_0 e^{i\omega t} \left(1 - \frac{4r^2}{d^2}\right) \quad (5)$$

Substituting this expression into (3) gives

$$V_0 = \frac{P R_c d^2}{\mu 16} \alpha_{ext} \quad (6)$$

As a result, the flow velocity amplitude V_0 defined in (6) is valid when

$$\alpha_{ext} < \frac{3200\mu^2}{P^2 d^3 R_c} \quad (7)$$

Following (6), to achieve a sensitive angular acceleration sensor, we need a fluid with a high density P and low viscosity μ to obtain a relatively large fluid flow velocity. Furthermore, the channel should have a large diameter d and the sensor benefits from a large system radius R_c . To demonstrate the sensing capability of our angular acceleration sensor, the setup shown in figure 4 was used and experiments were performed for rotational frequencies within a range of 7–14 Hz. The applied voltage U_s was generated sinusoidally using a Stanford SR 830 lock-in amplifier with its frequency set to 50kHz and the amplitude to 0.7V. The output of the bridge was measured differentially using the lock-in amplifier. Its output was demodulated by setting the amplifier time constant to 3ms and the roll-off to 12dB. The resulting envelope was then band-pass filtered using a Stanford SR 650 filter system with its band-pass set to 1–20Hz, in order to improve the signal-to-noise ratio, and amplified with a gain of 20dB. The filtered output was monitored using an oscilloscope (Agilent DSO1024A) and its RMS-value was measured using a multimeter (Keithley 2001). Using the geometrical properties of the rotational setup, the acceleration amplitude was calculated for every frequency. The obtained results for the measured RMS-voltage are shown in figure 8, together with a linear regression fit. As we observe, the sensor's response is in good agreement with the expected linear response. The calculated full scale error is found to be about 3.9%, with the full-scale set at approximately $2 \times 10^5 \text{ }^\circ \text{s}^{-2}$. To verify the sensor's response to angular accelerations, we changed the medium inside the tube from water to air. As a result, the output voltage dropped significantly and no clear sinusoidal waveform was observed when performing measurements identical to those shown in figure 5.

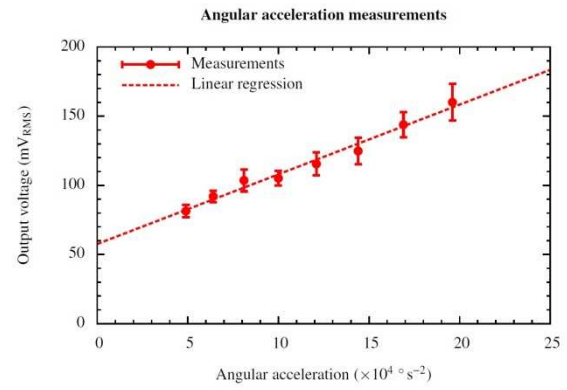


Figure 4: Measured response versus angular acceleration amplitudes. [13,14,15]

ACKNOWLEDGMENTS

The research described in this paper is supported by the Scientific Research Sector of TU-Sofia under the contract No 152nd0054-07

References

- [1] R. W. Baloh and G.M. Halmagyi. Disorders of the Vestibular System. Oxford University Press, Oxford, U.K., 1996.
- [2] S. U. Ay, F.-G. Zeng, and B. J. Shen. Hearing with Bionic Ears. IEEE Circuits and devices, 5:18{23, 1997.
- [3] M. Weinberg, J. Borenstein, J. Connelly, A. Kourepennis, P. Ward, and J. Heiertz. Application of draper/ boeing micromechanical inertial instruments. Sensors Expo'98, CSDL-P-3673, 1998. Oct., Chicago, IL.
- [4] W. Gong and D. M. Mereld. Prototype Neural Semicircular Canal Prosthesis Using Patterned Electrical Stimulation. Annals of Biomedical Engineering, 28:572{581, 2000.
- [5] W. Gong and D. M. Mereld. System Design and Performance of a Unilateral Horizontal Semicircular Canal Prosthesis. IEEE Transactions on Biomedical Engineering, 49(2):175{181, 2002.Feb.
- [6] A. Shkel. Micromachined gyroscopes: Challenges, design solutions, and opportunities. 2001 SPIE Annual International Symposium on Smart Structures and Materials, 2001. (Invited Paper) March, 2001, Newport Beach, CA.
- [7] I. S. Curthoys. The Response of Primary Horizontal Semicircular Canal Neurons In the Rat And Guinea Pig To Angular Acceleration. Exp. Brain Res, 47:286{294, 1982.
- [8] A. Shkel, R. Horowitz, A. Seshia, S. Park and R. T. Howe. Dynamics and control of micromachined gyroscopes. The American Control Conference, June 1999. San Diego, CA.
- [9] B. R. Munson, D. F. Young, and T. H. Okiishi, Fundamentals of fluid mechanics, 5th ed., J. Welter, T.

- Kulesa, and S. Dumas, Eds. USA: John Wiley & Sons, Inc., 2006.
- [10] X. F. Peng, G. P. Peterson, and B. X. Wang, "Frictional flow characteristics of water flowing through rectangular microchannels," *Exp. Heat Transf.*, vol. 7, no. 4, pp. 249–264, Apr. 1994.
- [11] E. R. Damiano and R. D. Rabbitt, "A singular perturbation model of fluid dynamics in the vestibular semicircular canal and ampulla," *J. Fluid Mech.*, vol. 307, pp. 333–372, 1996.
- [12] R. Vega, V. V. Alexandrov, T. B. Alexandrova, and E. Soto, "Mathematical model of the cupula-endolymph system with morphological parameters for the axolotl (ambystoma tigrinum) semicircular canals," *Open Med. Inform. J.*, vol. 2, pp. 138–148, 2008.
- [13] T. S. J. Lammerink, N. R. Tas, M. Elwenspoek, and J. H. J. Fluitman, "Micro-liquid flow sensor," *Sens. Act. A*, vol. 37–37, pp. 45–50, 1993.
- [14] ST Microelectronics, "LIS1R02 (L6671)," 2002, Angular accelerometer.
- [15] Endevco, "Model 7302BM4 – Piezoresistive angular accelerometer," 2009.
- [16] J. J. Groen and L. B. W. Jongkees, "The threshold of angular acceleration perception," *J. Physiol.*, vol. 107, pp. 1–7, 1948.

NEW RESEARCH FOR MEMS IN THE VESTIBULAR SYSTEM AND BASIC OVERVIEW OF MEMS USED TILL NOW

V. Manoev, Ts. Kachamachkov

Technical University of Sofia, Bulgaria
Faculty of Telecommunication, TU-Sofia, "KI. Ohridsky" str. 8, 1000 Sofia, Bulgaria

Abstract

The ear is the organ used for hearing and maintaining equilibrium. In the inner ear, the vestibular system is responsible for the sense of balance. The main organs of the vestibular system are the semicircular canals, the saccule, and the utricle. Within each of the vestibular organs, sensory receptors in the form of hair cells detect motion and send a message to the brain for interpretation. This paper presents a feasibility study on an MEMS – based implantable vestibular solutions. Such as the MEMS - Implantable vestibular prosthesis that will replace the function of the damaged vestibular end-organ by providing an MEMS chip that will replace the function of the damaged vestibular end-organ by providing an MEMS chip that will accurately sense, extract, and transmit 3-dimensional motion information for people who have permanently lost peripheral vestibular function. The prosthesis prototype includes orthogonal triads of accelerometers and gyroscopes on a single fingernail sized chip. Based on the physiological data on the perceptual thresholds of linear acceleration and angular velocity in humans.

- New research for mems in the vestibular system.
- The author has made a thorough research of existing researches.
- Achieving a thorough overview of current researches for mems in the vestibular system.

1. INTRODUCTION

This paper investigates an ear worn sensor for the development of a gait analysis framework. Instead of explicitly defining gait features that indicate injury or impairment, an automatic method of feature extraction and selection is proposed. The proposed framework uses multi-resolution wavelet analysis and margin based feature selection. It was validated on three datasets; the first simulating a leg injury, the second simulating abdominal impairment that could result from surgery or injury and the third is a dataset collected from a patient during recovery from leg injury. The method shows a clear distinction of gait between injured and normal walking. It also illustrates the fact that using source separation before pattern classification can significantly improve the proposed gait analysis framework.

2. USING HEAD WORN ACCELERATION SENSORS

Features that can quantify human gait play a major role in the studies of injury rehabilitation, improving athletic performance, and the design of prosthetic limbs. Human gait has long been an active area of research, and many systems have been proposed for observing gaiter regularities. Thus far, most of these systems are based on image information from video sequences. When used in conjunction with

biomechanical models, these features can allow quantitative analysis of many specific gait characteristics such as joint moments and powers (kinetic analysis), joint angles, angular velocities, and angular accelerations (kinematic analysis) [1]. In these systems, optical markers are placed near anatomical landmarks of the body and features related to gait are extracted from video sequences. Parametric models have been used extensively to describe a set of image observations. An example is 3-D modelling of moving people which can be achieved by using volumetric bodies based on elliptical cylinders [2] or tapered super quadrics. Alternatively, 2-D models that represent the projection of 3-D data to an imaging plane can be used (2D/3D contour-modelling for example [3]). In general, methods that consider the use of kinematic constraints can handle more complex motions and occlusions. These constraints are used to improve tracking as well as preventing model violations of the derived 3-D structures. For example, Dockstader et al. [4] use soft constraints in a hierarchical structural model of the human body to analyse video sequences captured in a home environment. Reviews on human motion analysis based on video, including summaries of modelling, tracking and recognition, are provided by Dariush [5] and Aggrawal et al. [6]. An alternative to vision based gait analysis is the use of body worn sensors to obtain motion data. The variables that can be measured during gait analysis

depend on the technique selected. The most commonly measured variables include initial contact (IC) that defines the beginning of a complete gait cycle and thus cycle duration and frequency, and terminal contact (TC) that marks the start of the swing phase. Gyroscopes, which measure angular velocity, and accelerometers which measure linear acceleration, have been used as a wearable option to measure these variables [7]. Coleman et al. [8], Aminian et al. [7] and Selles et al. [9] provide methods of measuring both TC and IC timing information. On the other hand, Yoshida et al. [10] use an accelerometer attached to the patient's waist and observe frequency peaks in the anterior plane to detect leg injury. In reality, however, injury causes changes in both the temporal and frequency domains and this variation is not normally limited to one direction of motion. Due to leg injury, a patient's motion can show signs of swaying for maintaining equilibrium, as well as a change in the distribution of the forces when the patient's foot touches the floor. Injury indifferent parts of the body, resulting from abdominal surgery for example, could also affect gait and balance, especially when a patient needs to climb stairs, reach for objects or lie down.

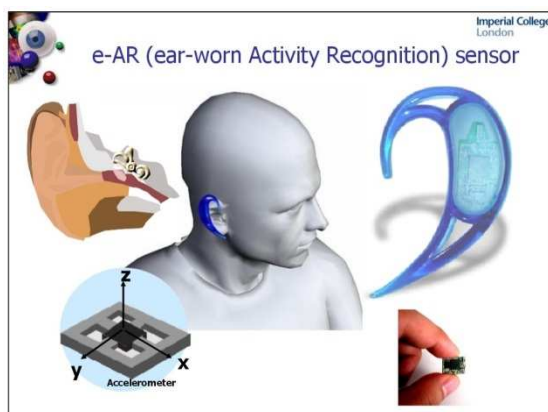


Figure 1: e-AR sensor

3. EXPERIMENTAL SETUP

Head-worn accelerometers have in the past been used to study the movement of the head compared to the rest of the trunk, as well as gait changes due to disease and aging. As a subject mobilises, the head remains relatively stable when compared to the trunk, and therefore the direction of its movement during activities such as walking is more representative of the body's movement as a whole. A study by Kavanagh et al (2005) [11] used tri-axial accelerometers attached to the head and trunk of

normal volunteer subjects to collect data whilst they were walking, and showed that accelerations detected at the head were not only more regular than those at the trunk in each direction, but also associated with a greater degree of coupling between directions [12]. Authors concluded therefore that during walking, accelerations of the head are significantly attenuated and more tightly controlled when compared to accelerations of the lower trunk. Despite being a relatively stable part of the body during motion, the head moves proportionately more with increasing activity (for example climbing stairs versus walking on a flat level) [13], which is important to consider when evaluating gait. It does however move less than the limbs due to the stabilising effect conferred by the trunk and neck, making it an attractive site for sensor placement [14,15]. The trunk does play a critical role in maintaining head stability by regulating gait-related oscillations in all directions, and the neck confers additional control the rebyenhancing head stability during walking [11]. The experiments outlined in this work are designed to observe changes in gait that occur following impaired truncal and limb immobility as detected by an ear-worn activity recognition sensor (e-AR sensor) [16]. The e-AR sensor has been used previously for observing post-operative recovery [16], activities of daily living and sports performance. A multi-resolution wavelet-based framework is proposed in this paper to analyse the e-AR sensor's accelerometer data in the 3 directions of motion. Automatic margin-based feature selection is used to select frequency bands of the wavelet transform that provide discrimination between classes of motion. Independent Component Analysis (ICA) is used as a means of source separation for 3-D acceleration.

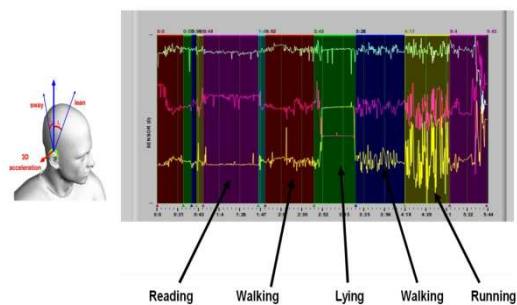


Figure 2: e-AR sensor experimental results.

The purpose of the semicircular canal prosthesis is to restore balance function. Ideally, the prosthesis will be able to sense motion with sufficient precision

and to deliver signals to the central neural system matching signals that the natural organ would generate. We propose to implement the vestibular prosthesis using MEMS technology. An ensemble of six inertial MEMS sensors is required to measure six-degrees of freedom of the head motion on a single silicon chip and packaged in a volume smaller than 1 cubic centimeter. Micromachining can shrink the sensors size by orders of magnitude, reduce the fabrication cost significantly, and allow the electronics to be integrated on the same silicon chip [17]. Our first prototype of the vestibular prosthesis is implemented using polysilicon surface micromachining technology. In the prosthesis, the three semi-circular canals are replaced by 3-axis MEMS gyroscopes, while the two otolith organs are replaced by 3-axis accelerometers, Fig-3.

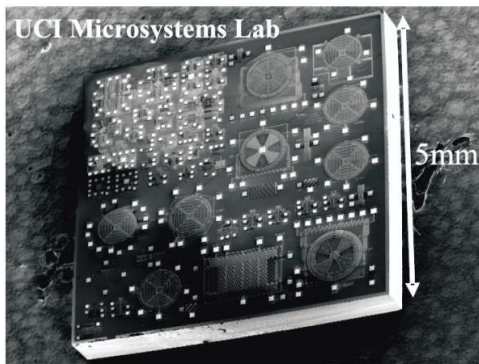


Figure 3. A prototype multi-sensor unit including accelerometers and gyroscopes. The experimental unit does not include electronics on the chip. The experimental chip is fabricated using JDS/Uniphase's MUMPs technology

The MEMS accelerometer consists of a proof mass suspended by compliant beams anchored to a fixed frame. External acceleration due to motion of the object to which the sensor's frame is attached, displaces the support frame relative to the proof mass, which in turn, changes the initial stress in the suspension spring. Both this relative displacement and the suspension-beam stress can be used as a measure of the external acceleration. In the most general case, the proof-mass motion can have six degrees of freedom. But typically in a unidirectional accelerometer, the geometrical design of the suspension is such that one of these axes has low stiffness while high stiffness along other axes. For example, in case of the Z-axis accelerometer, the proof mass of the device will displace in out-of-plane of the chip only if there is an acceleration component along the z-axis. In the basis of operation, the proof-mass, which constitute the active portion of the sensor, is driven by an oscillator circuit

at a precise amplitude and high frequency. When subjected to a rotation, the proof-mass will be subjected to the Coriolis force:

$$F = 2m\Omega \times V_c \quad (1)$$

where m – mass, V_c – instantaneous radial velocity of the center of mass, Ω – input rate. As an illustrative example, consider a Z-axis gyroscope. The behaviour of the gyroscope is naturally described. Schematic illustration of a MEMS implementation of the z-axis rate integrating gyroscope with respect to the non-inertial coordinate frame $\{x; y; z\}$,

$$X'' + \omega_n^2 X - 2\Omega Y' = 0 \quad (2)$$

$$Y'' + \omega_n^2 Y - 2\Omega X' = 0 \quad (3)$$

The essential feature of these equations is the presence of the Coriolis acceleration terms $-2\Omega Y'$ and $-2\Omega X'$. It is the Coriolis acceleration that causes a transfer of energy between the two gyroscope modes of operation. The resultant Coriolis force is perpendicular to both the input rate and the instantaneous radial velocity in the drive direction. This produces a motion of the proofmass in direction perpendicular to its initial oscillation. Under rotation, however, the Coriolis acceleration will cause energy to be transferred from the x-axis (primary mode) to the y-axis (secondary mode) building up a vibration amplitude along the y-axis. The ratio of the amplitude in the secondary mode of vibration to the amplitude of the primary mode of vibration can be shown to be proportional to the rotation rate and is given by [18]

$$\frac{Y}{X} = 2Q \frac{\Omega}{\omega_n} \quad (4)$$

CONCLUSION

This work was carried out in conjunction with SAPHE (Smart and Aware Pervasive Healthcare Environment) supported by the UK Technology Strategy Board (TSB) and WASP (Wirelessly Accessible sensor populations), funded by the European Commission under Framework 6. We would also like to thank all subjects who took part in this study.

ACKNOWLEDGMENTS

The research described in this paper is supported by the Scientific Research Sector of TU-Sofia under the contract No 152пд0054-07

References

- [1] G.F. Harris and J.J. Wertsch, Procedures for Gait Analysis. Arch Physical Medicine and Biology, 1994. 75(2): p. 216-225.
- [2] D. Hogg, Model based vision: A program to see a walking person. Image Vis. Comput., 1983. 1(1): p.5-20.
- [3] M. Isard and A. Blake, Condensation-Conditional density propagation for visual tracking, Int. J.Comput. Vis., 1998.29(1): p. 5-28.
- [4] S.L. Dockstader, M.J. Berg, and A.M. Tekalp, Stochastic kinematic modeling and feature extraction for gait analysis. Image Processing, IEEE Transactions on, 2003. 12(8): p. 962-976.
- [5] B. Dariush, Human motion analysis for bio mechanics and biomedicine. Machine Vision and Applications, 2003. 14(4):p. 202-205.
- [6] J. K. Aggrawal, and Q. Cai, Human motion Analysis: A review. Comput. Vis. Image Understanding, 1999. 73(3): p.428-440.
- [7] K. Aminian, et al., Temporal feature estimation during walking using miniature accelerometers: an analysis of gait improvement after hip arthroplasty. Med Biol Eng Comput, 1999. 37(6): p. 686-91.
- [8] K. L. Coleman et al., Step Activity Monitor: Long Term-Continuous Recording of Ambulatory Functions. J. Rehab. Res. Develop., 1999. 36(1): p. 8-18.
- [9] R. W. Selles et al., Automated estimation of initial and terminal contact timing using accelerometers; development and validation in transtibial amputees and controls. Neural Systems and Rehabilitation Engineering, 2005. 13(1): p. 81-88.
- [10] T. Yoshida, et al. Gait Analysis for Detecting a leg accident with an accelerometer. in 1st Distributed Diagnosis and Home Healthcare (D2H2) Conference., 2006. Virginia, USA.
- [11] J. Kavanagh, R.S. Barrett, and S. Morrison, The role of the neck and trunk in facilitating head stability during walking. Exp Brain Res, 2006. 172(4): p. 454-63.
- [12] J. Kavanagh, S. Morrison, and R.S. Barrett, Coordination of head and trunk accelerations during walking. Eur J Appl Physiol, 2005. 94(4): p. 468-75.
- [13] R. Cromwell and R. Wellmon, Sagittal plane head stabilization during level walking and ambulation on stairs. Physiother Res Int, 2001. 6(3): p. 179-92.
- [14] E. Hirasaki et al., Analysis of head and body movements of elderly people during locomotion. Acta Otolaryngol Suppl, 1993. 501: p. 25-30.
- [15] H. B. Menz, S. R. Lord, and R. C. Fitzpatrick, Acceleration patterns of the head and pelvis when walking on level and irregular surfaces. Gait Posture, 2003. 18(1): p. 35-46.
- [16] B. Lo, L. Atallah, O. Aziz, M. ElHelw, A. Darzi, G-Z. Yang Real-time pervasive monitoring for postoperative care. Proc. of BSN07, IFMBE, vol. 1, 2007; 122-127.
- [17] A. Shkel. Smart mems: Micro-structures with error-suppression and self-calibration control capabilities. The American Control Conference, June 2001. Arlington, VA (Invited).
- [18] A. Shkel, R. Horowitz, A. Seshia, S. Park and R. T. Howe. Dynamics and control of micromachined gyroscopes. The American Control Conference, June 1999. San Diego, CA.

CLINICAL RESULTS IN THE TREATMENT OF PATIENTS WITH DIABETIC POLYNEUROPATHY WITH SIMULTANEOUS APPLICATION OF LOW-FREQUENCY MAGNETIC FIELD AND MINERAL WATER

Vladimir Petrov MD*, Prof. Dr. Dimitar Dimitrov**

* Specialized Hospital for Rehabilitation "St.Mina" Varshets, Bulgaria

** Technical University, Faculty of "Telecommunications", Sofia, Bulgaria

Abstract

The influence of magnetic field on the velocity of free ions of solution, which is in a state of dissociation is the basic phenomena in magnetotherapy. The magnetic field increase the value of ion's velocity and change the direction of ion's velocity. Therefore the permanent or the low frequency magnetic field potentiates the movement of ions of all liquids in live tissues (first of all ions of the blood), movement of ions of mineral water and diffusion of ions from mineral water through the skin of human body.

On the base of above mentioned phenomena and properties of permanent and low frequency magnetic field a new method for therapy of diabetic polyneuropathy has been created using simultaneous application of magneto-therapy and hydrotherapy

1. INTRODUCTION

The magnetic field stimulates or inhibits the release of neurotransmitters, substances that transmit nerve impulses. This determines the management of the pain.

Second, it influences the central and autonomic nervous system, regulating the function of its two parts. It harmonizes and inhibits pathological foci and nerve transmitting voltage to make the voluntary and involuntary functions and movements in the body.

The magnetic field acts to eliminate cholesterol from the blood, creating a constant pulse wave in blood vessels. There is a very good effect in functional disorders of the central, peripheral and autonomic nervous systems.

The most common complication of diabetes mellitus /DM/ - diabetic neuropathy /DN/ is described in the mid nineteenth century /1864/ by Marshal de Calvi, as later on this problem are exclusively devoted a lot of research and publications, such as distal type polyneuropathy /DPN/ with excitement and waste sensory, reflex, motor symptoms and vegetative-trophic events.

Treatment of DPN is a subject to various medical and non-medical professionals, where the role of physicians in physical medicine and rehabilitation is leading. In the medical literature there are numerous scientific publications, monographs and disser-

tations dedicated to the physical treatment of DPN with natural and preformed physical factors. Our opinion is that the patients with DPN are sent too late, or not at all for physical therapy. On the other hand the very diagnosis of this complication of DM is diagnosed too late and is not paying enough attention to the complaints of the patients.

This clinical study describes the results of the simultaneous application of low-frequency magnetic field and water treatment in the cases of diabetic polyneuropathy.

2. OBJECTIVES AND TASKS

1. Research and optimization of the parameters of low-frequency magnetic fields with concomitant water treatment in order to achieve the best therapeutic effect in patients with diabetic polyneuropathy.

2. Development and application of new methods of treatment with low-frequency electromagnetic fields, alone and in combination with mineral water in:

- Diseases of the endocrine system
- Metabolic diseases
- Diseases of the central and peripheral nervous system

3. SYSTEM FOR THERAPY

As a result of cooperation between SHR "St. Mina" - Varshets and Department of Telecommunications at the Technical University of Sofia was modified an electric bath for the simultaneous application of low-frequency magnetic field and hydrotherapy (Fig.1).



Fig.1. System for therapy of polyneuropathy using simultaneously application of magneto-therapy and hydrotherapy

The system has 4 separated bathtub, two for the hands and two for the legs. The bathtub are full with mineral water. There are two inductors in every bathtub. The inductors are encapsulated. Every pair of inductors are connected to the relevant output of apparatus for magneto-therapy. On Fig.2 can be seen apparatus for magneto-therapy with 8 inductors. This apparatus is a part of the system.

The apparatus for magneto-therapy provides low frequency pulsed magnetic field. During the procedure the adaptation of human body to the parameters of external pulsed magnetic field should be avoided. Because of that the frequency of magnetic pulses and their amplitudes should be variable. A microprocessor's system is implemented in apparatus for magneto-therapy. An appropriate software packages are used for the microprocessor's system.



Fig. 2. Apparatus for magneto-therapy with encapsulated inductors

4. MATERIALS AND METHODS

The study includes 60 patients with diabetic polyneuropathy (40 men and 20 women), treated with a new system for magneto therapy and mineral water. This system has four separate small tubs for separated hydrotherapy of the limbs. On both sides of the feet and ankles and on both sides of the wrists of the hands are placed two sealed magnetic inductors. We use a special apparatus for magneto therapy that provides simultaneous excitation of magnetic field in all eight inductors. The magnetic field has variable parameters in order to avoid adaptation and provides opportunities for longer course of treatment if necessary.

The patients with DPN who in the period of 2014-2015 conducted a treatment in the SHR "St. Mina" were treated only with combination of magnetic therapy and mineral water. They were aged 45-70, the average age of 55, 20 of them were with DM-first type and 40 - second type. The diagnosis of all patients was confirmed by EMG, held in advance. Patients were tested before and after completion of the treatment. In the clinical picture dominated sensory "plus" and "minus" signs: acroparesthesy, pain, changes in surface, deep and complex sensitivity, impaired statics and dropped reflex symptoms /Achilles and knee reflexes/.

With this message, we set the goal to present our experience with the application of a new method in the treatment of patients with DPN.

5. METHODS USED FOR OBJECTIFICATION

For the objectification of the results of the study we have applied the original method of Assoc.Prof. D-r Zivko Kolev, MD, PhD

1. Study of the pain in the lower limbs:

A/ By Visual analogue scale / 0-20 /

B/ By Dolorimetry, which was held in two points: in the middle of the tibial bone and the 1st metatarsal bone.

2. Quantification of the vibrational perception - vibroestheziometry by the graduated tuning fork of Rydel Saifer /Germany/ on the same places as with that of dolometry. The vibrational sense is conducted by the rear colons of the spinal cord and reduction or loss of it is considered to be one of the first symptoms of DPN.

3. Study of the static of the patient through „Sensitized Romberg's symptom" that shows impairment in the deep sensation. The patient is standing upright, folded one foot over the other with stretched hands in supination with eyes closed. We recorded the onset of the ataxia during stay of the patient in this position for 60 seconds.

4. Examination of Achilles and knee reflexes.

6. RESULTS

We tracked changes in patients with diabetic polyneuropathy after 10 procedures with magnetic field and mineral water of upper and lower limbs.

Conducted a 10-day treatment of the patients with magnetic field and mineral water therapy showed improvement of their condition. We recorded three groups of symptoms after their treatment:

FIRST GROUP, in which patients are impacted best. These are sensory plus and minus signs /pain, paresthesia, hypoalgesia/.

At the beginning patients showed severe pain /13.5/, which fell to 5.2.

The reduction of pain reported by dolorimeter showed a better response to the points of the first metatarsal.

The hypoalgesy is significantly more pronounced in the distal surveyed points and its improvement is better as compared with the points of both tibial bones.

SECOND GROUP of symptoms presents the research of statics / sensitized symptom of Romberg / - improvement here is less - ataxia occurs at a later stage of 60 sec. straight posture.

THIRD PARTY symptoms / the study of the Achilles and knee reflexes /. In 37 of the patients are found changes in Achilles reflexes, and in 23 in the knee. The conducted treatment has led to minimal improvement in their status.

Medical reporting results were based on subjective status of the patients and objective data. The therapeutic effect was expressed with significant reduction of the pain, improvement of the sensitivity, increased skin temperature and volume of movement and stabilization of the coordination and the gait.

7. DISCUSSION

Our observations indicate that combined treatment with low frequency magnetic field and mineral water is particularly effective when there is a prevalence of autonomic disorders. From the analysis of the clinical results, the authors revealed the therapeutic advantages of simultaneous application of low-frequency magnetic fields and mineral water. Inpatient treatment and rehabilitation, especially in the early stages of the disease, is essential and important for the favorable outcome of the suffering.

8. CONCLUSION

1. As a result of treatment with the combine therapy with magnetic field and mineral water of patients with DPN, clinical symptoms and quality of life improved significantly.

2. We obtained the best results with the presented sensory impairments, slightly were influenced impaired statics and reflexes.

3. Combined therapy with magnetic field and mineral water has its place in the treatment of patients with DPN and should be used in our physiotherapy practice.

4. Diabetic neuropathy is a common disorder in clinical practice, which requires timely and comprehensive physiotherapy and rehabilitation.

5. Simultaneous application of low-frequency pulsed magnetic field with varying parameters and mineral water provides encouraging results in the treatment of diabetic polyneuropathy.

References

- [1] Dimitrov, D., Tz. Simultaneously Influence of Magnetic and Electrical Field on the Human Body, Electronics and Electrical engineering, Nr.1(60), 2006, p.32-36
- [2] Dimitrov, D. Tz. Computer Simulation of Space Configuration of Low Frequency Magnetic Field in Magnetotherapy, Electronics and Electrical Engineering, Nr.3(59), 2005, p.28-32.
- [3] Durney, H. D., and D. A. Christensen, Basic Introduction to Bioelectromagnetics, CRC Press, Boca Raton, FL, 1999., p.380
- [4] Lin, J. C., (ed.), Electromagnetics in Biology and Medicine, Review of Radio Science, 2000, p.330
- [5] Robert, P., Electrical and Magnetic Properties of Materials, Artech House, Norwood, MA, 1988, p.420
- [6] Pressman, A. S., Electromagnetic Fields and Life, Plenum Press, New York, NY, 1970, p.280
- [7] www.vizimag.com, Stuart Beeteson, p.240

3D MODEL OF PLATFORM FOR SPINNING PILOTS UNDER AN ANGLE AND OTHER MEDICAL USES

Tsvetan Kachamachkov

Technical University of Sofia, Bulgaria
Postal Sofia - 1309, „Sv. Troitsa” 303 - B - 39

Abstract

With the obtained surface registration, statistical morphometric analysis based on the coordinates' deviation can be performed. Using the two-sample Hotelling's T-squared test, the p-value at each vertex on the surface is found.

1. INTRODUCTION

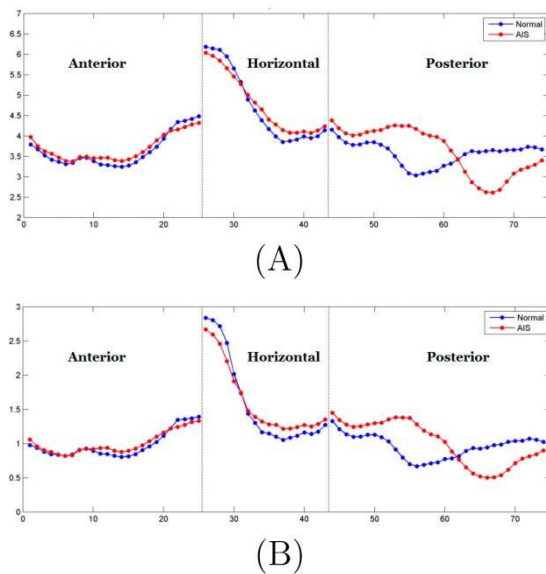


Figure 1: (A) Perimeters of each homotopic loops of the normal mean VS and the AIS mean VS. (B) Area of each minimal surfaces enclosed by the homotopic loops of the normal mean VS and the AIS mean VS.

VS is a key organ for maintaining postural balance in humans and poor postural balance is a recognized characteristic in AIS patients [1, 2]. The shape of the VS is confirmed being related to the growth of vertebrates.

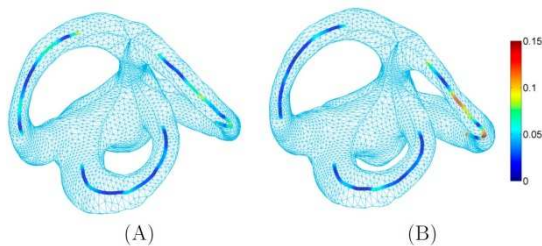


Figure 2: (A) mean surface of normal subjects. (B) mean surface for AIS subjects. Distances of each points on the center lines from the best fit planes of the normal mean VS surface and AIS mean VS surface.

The distance is visualized by the color maps. Red color indicates a large deviation from the best fit plane. Lambert et al. [3] made use of frog models for experiment to conclude that asymmetric vestibular inputs could lead to imbalanced growth of the spine.

Thus, the studies on the relationship between AIS and VS abnormality become important to the etiology of the disease. Our proposed methods focus on the accurate registration and the quantitative shape analysis of the canals in the VS. Furthermore, it is also observed that there are distortions of the plane of PSC in the AIS patients. Such planar defection was found affecting the locomotion in primates by [4]. The proposed surface registration method is shown to be helpful in the shape analysis of the complex geometry of VS. It is hoped that a standardized assessment could set out for clinical diagnosis. To examine the accuracy and stability of the measurement, a larger sample size would be included in the continuation of this study. To perform a more comprehensive local shape analysis, a complete shape index defined by the Beltrami coefficients and curvature can be used. The shape index effectively measures the geometric difference between two VS surfaces at each vertex of surfaces. To test our proposed algorithms, experiments have been carried out to register VS surfaces of 15 normal control subjects and 12 AIS subjects. Results show that our method can effectively and accurately compute the surface registrations between the VS surfaces. Shape analysis has also been carried out using the proposed shape features and shape energy, which reveals shape differences in the posterior canal between normal and diseased AIS groups.

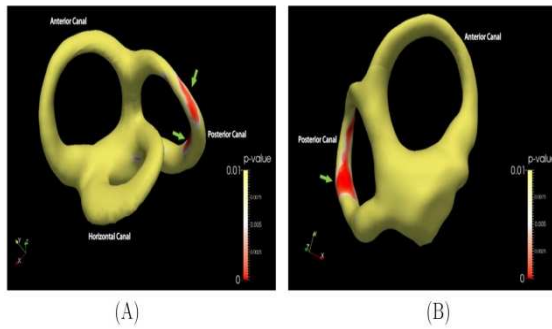


Figure 3: (A) p-map from the frontal viewpoint. (B) p-map from the backward view point. Statistical p-map showing the regions with p-value < 0:001 on the AIS mean surface (Red-colored vertex indicating p-values < 0:001).

Zero gravity has become a very popular feature among massage chair models and among massage chair shoppers. I get asked all the time about whether a particular model has zero gravity or not. Funny thing is, most folks think they want it but have no idea what it really is! But, is zero gravity something that you really want in a massage chair? I will define it and then explain to you the pros and cons of zero gravity, especially as it pertains to you, the user, and your therapeutic experience with or without it in your massage chair. In physics, zero gravity is defined, essentially, as weightlessness. However, zero gravity as it pertains to seating is defined by two conditions: 1. A 30 degree upward tilt of the seat, and 2. A 120 articulation between the tilted seat and the chair back. The essence of zero gravity in the seating paradigm is that with these angular articulations, your body and spine are not necessarily in a weightless position (because gravity is always at play here on earth!), but your body is positioned such that it's weight is evenly distributed throughout the body. Here is a great image of the Human Touch HT-7450, the first zero gravity massage chair, in its zero gravity position. Notice the upward tilt of the seat and the angle of the chair back, relative to the seat.



Figure 4: Platform for angular acceleration

2. 3D MODEL

In biology, the vestibular system is used to detect the head motion in space and results in stabilization of the visual axis, head and body posture [5]. Furthermore, the vestibular system helps with the sense for motion and change in orientation in space. The system consists of two parts: the two otolith organs (the saccule and utricle), which sense linear acceleration (gravity and translational movements), and the three semicircular canals which sense angular acceleration in three planes (pitch, roll, and yaw) [5, 6].

You are probably wondering by now what makes the angular acceleration so important, the vestibular system is affected differently by the angular acceleration this is because of the nature of the fluid in the inner ear. You are probably wondering by now what makes the angular acceleration so important, the vestibular system is affected differently by the angular acceleration this is because of the nature of the fluid in the inner ear it reacts very particular under angular acceleration this is why we have developed a new platform the platform is adaptable to all the normal system for vestibular testing usually found in hospital. One of the main strive in optimization is to accumulate a financial need for the developed product, the proper use would include usage of the already manufactured chairs for testing of the vestibular system so we focused our efforts on improving the already existing systems worldwide. We developed a unique and simple solution able to be implemented to all systems worldwide giving them the option of angular acceleration.

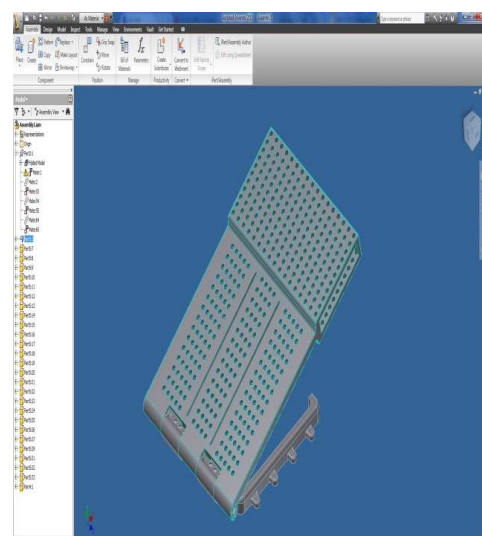


Figure 5: Platform upgrade for vestibular system experiments 3D MODEL

We are asked to compute the maximum length of a cylindrical titanium alloy specimen (before deformation) that is deformed elastically in tension. For a cylindrical specimen

$$A_0 = \pi \left(\frac{d_0}{2} \right)^2$$

where d_0 is the original diameter.

$$\begin{aligned} l_0 &= \frac{\Delta l}{\varepsilon} = \frac{\Delta l}{\frac{\sigma}{E}} \tilde{E} \frac{\Delta l E}{F} \tilde{E} = \\ &= \frac{\Delta l E \pi \left(\frac{d_0}{2} \right)^2}{F} = \frac{\Delta l E \pi d_0^2}{4F} \\ &= \frac{(0,42 \times 10^{-3} m) \left(107 \times \frac{10^9 N}{m^2} \right) (\pi) (3,8 \times 10^{-3})^2}{(4)(2000 N)} \end{aligned}$$

This problem asks us to compute the diameter of a cylindrical specimen of copper in order to allow an elongation of 0.50 mm.

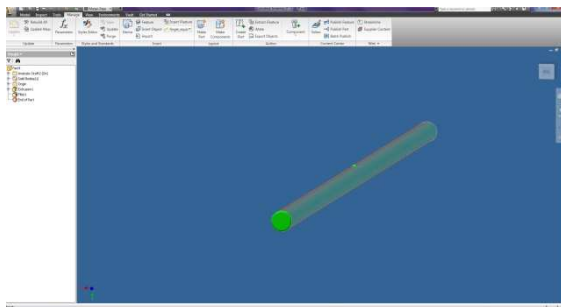


Figure 6: Mechanical analysis of the bearing axis.

The bond of the epoxy grout to the concrete foundation is stronger than the bond of the concrete to it self. Typically, concrete will separate next to the bond line of the epoxy and concrete. Therefore, the weakest link in the bond of epoxy to concrete is the concrete it self. The force required to pull concrete apart is called its shear strength. A conservative value for concrete shear strength is 800psi. To determine the force required to pullout the bolt separating it at the epoxy to concrete bond, use the following calculation strength hanch or bolt in concrete as a comparison, an anchor bolt set in a concrete foundation will typically crack up and out from the bottom of the bolt at a 45 degree angle in a cone shaped section. The force required to pull up this cone shaped section of concrete is the force required to separate concrete over the total surface area of the cone. The surface area of a

cone (sac one) = lateral surface area of a right circular cone with 45 degree sides.

PULL OUT STRENGTH IN POUNDS				
HOLE DIAMETER	BOLT LENGTH			
	3"	4"	5"	10"
5/8"	4,710	6,280	7,850	15,700
3/4"	5,650	7,530	9,420	18,840
1"	7,530	10,050	12,560	25,130
1.5"	11,309	15,070	18,840	37,690
2.0"	15,070	20,100	25,130	50,260

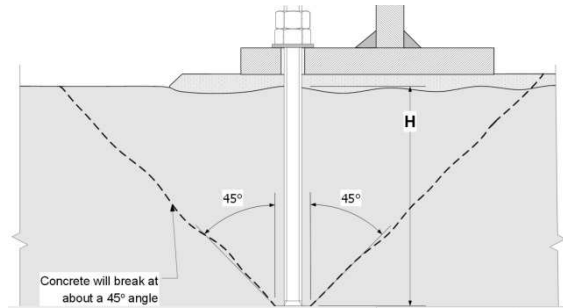


Figure 7: Acker bolts standard.

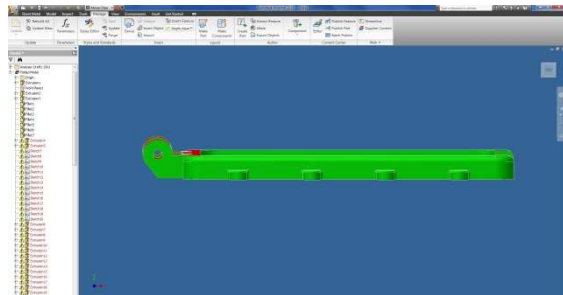


Figure 8: Mechanical analysis of the bearing fundament with anchor bolts.

CONCLUSIONS

The goal of this paper was to demonstrate that MEMS technology is a viable candidate for implementing a completely implantable vestibular prosthesis. Based on the available physiological data, we have identified performance requirements for the vestibular prosthesis and concluded that MEMS sensors can provide better performance than the human's sensation thresholds. Experimental data for a prototype of ADI's surface micromachined rate gyroscope supports the claim. Weal so presented an architecture for the vestibular prosthesis and fabricated the first prototype of the sensing unit of the prosthesis. Development of the completely implantable vestibular prosthesis is in its initial phase of exploration. Many technical issues need to be addressed, including the design of a robust low-drift sensing unit on the same chip,

design of control architecture suppressing the drift over time in the unit, integration of pulse generator and stimulator on the same chip, capability providing wireless programming and power beaming to the chip, design of bio-compatible package for the prosthesis, and interface of the prosthesis with neurons. Benefiting from the unique capabilities of the MEMS technology, this vestibular implant will be small and consume little power, and can be potentially manufactured in large quantities at low cost.

ACKNOWLEDGMENTS

The research described in this paper is supported by the Scientific Research Sector of TU-Sofia under the contract No 152пд0054-07

References

- [1] T. Haumont, G. C. Gauchard, P. Lascombes, P. P. Perrin, Postural instability in early-stage idiopathic scoliosis in adolescent girls, *Spine* 36 (13) (2011) E847{E854.
- [2] N. N. Byl, S. Holland, A. Jurek, S. S. Hu, Postural imbalance and vibratory sensitivity in patients with idiopathic scoliosis implications for treatment, *Journal of Orthopaedic & Sports Physical Therapy* 26 (2) (1997) 60{68.
- [3] F. M. Lambert, D. Malinvaud, J. Glaunes, C. Bergot, H. Straka, P. P. Vidal, Vestibular asymmetry as the cause of idiopathic scoliosis: A possible answer from xenopus, *Journal of Neuroscience* 29 (40) (2009) 12477{12483.
- [4] M. D. Malinzak, R. F. Kay, T. E. Hullar, Locomotor head movements and semicircular canal morphology in primates, *Proceedings of the National Academy of Sciences of the United States of America* 109 (44)(2012) 17914{17919.
- [5] C. Fernández and J. M. Goldberg, "Physiology of peripheral neurons innervating semicircular canals of the squirrel monkey. II. Response to sinusoidal stimulation and dynamics of peripheral vestibular system," *J. Neurophysiol.*, vol. 34, no. 4, pp. 661–675, Aug. 1971.
- [6] S. B. Yakushin, T. Raphan, J.-I. Suzuki, Y. Arai, and B. Cohen, "Dynamics and kinematics of the angular vestibulo-ocular reflex in monkey: effects of canal plugging," *J. Neurophysiol.*, vol. 80, no. 6, pp. 8077–8099, 1998.

PORTABLE 3- CHANNEL REAL-TIME EMG ACQUISITION DEVICE FOR USE WITH MYOELECTRIC PROSTHESES

Viktor A. Nedialkov

Department of Radio Communications and Video Technologies, Faculty of Telecommunications,
Technical University of Sofia, 8 Kl. Ohridski Blvd, Sofia 1000, Bulgaria

Abstract

A multi-channel portable EMG amplifier and acquisition device is proposed. The device is intended to be used with myoelectric prostheses, therefore there is an emphasis on the multichannel real-time acquisition, portability, current consumption and connectivity features.

The goal of the design is to implement the latest low-power high speed technologies available on the market today.

The device is not yet intended to run the EMG signal algorithms, but to send the raw signals to the PC where it will be more convenient to process the data for the research purposes.

This document covers the EMG signal all the way from the muscle through the amplifier, the Driven Right Leg (DRL) noise suppressor, filtering, digitalization and PC communication.

The article includes complete schematics, analysis and tests of the device.

1. INTRODUCTION

The EMG signal, recorded from a surface electrode is comprised of the action potentials of many single motor units SMU (fig. 1). The resultant signal has a frequency range from 25Hz to several thousand Hertz and amplitude in the range of 20-2000 μ V [1][2].

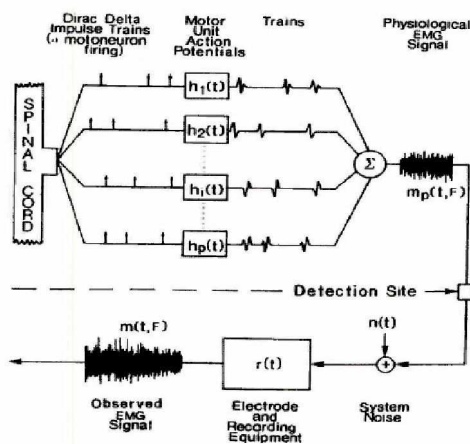


Fig. 1

The amplifier must be designed to cover this frequencies and amplitudes.

According to Nyquist-Shannon theorem, which basically says that the sampling frequency must be at least two times higher than the highest frequency sampled. If this theorem is not respected, aliasing will occur. The above requirement has important consequences to the design because we

must choose a cut off frequency high enough not to lose valuable signal but low enough to avoid a very complicated and expensive design.

The core of the design is the microcontroller. It must be chosen very carefully so that it is powerful enough to be able to process the data at the chosen sampling rate but at the same time to be with as low as possible current consumption. High power consumption will need bigger batteries hence the design will become bigger and heavier.

There are several communication possibilities for the design. In recent years many manufacturers developed small and easy to implement OEM modules for different type of communication – USB, Wireless, Bluetooth and GSM modules. For this design a Bluetooth module is chosen because, we need a wireless communication with enough speed and a distance no more than 10-20 meters, which is perfectly covered by the Bluetooth module.

Below a general block scheme of the design is shown.

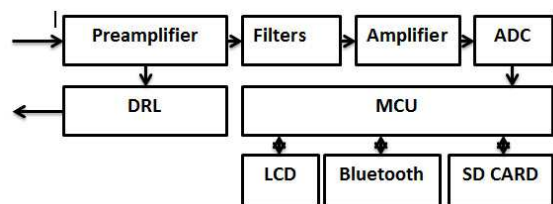


Fig. 2 (Block scheme of the device)

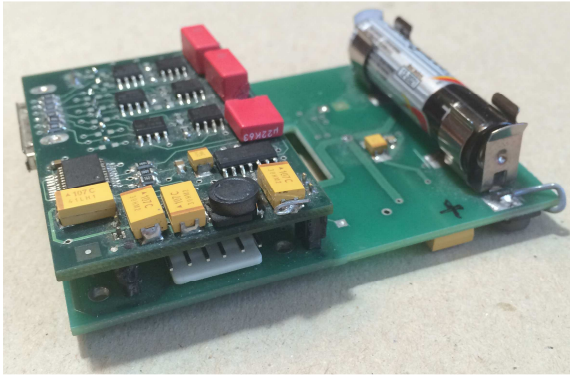


Fig. 3. The device prototype

2. AMPLIFIER

A three-channel amplifier has been designed to measure the EMG signal. The block diagram depicted in Figure 2 shows the different stages. The amplifier consists of: preamplifier, Driven Right Leg (DRL), filter, second amplification stage.

2.1. Preamplifier

The preamplifier is based on the AD627 instrumentation amplifier by Analog Devices. This IC has very good CMRR, very low offset voltage, and very high input impedance. Also it is a micro-power and has rail to rail operation which can allow us to use lower voltage levels.

The gain of the amplifier is determined by the formula:

$$\text{Gain} = 5 + (200\text{k}\Omega / R_g)$$

$$R_g = 200\text{k}\Omega / (\text{Gain} / 5)$$

A gain of 10 have been chosen for this stage.

A group of resistor and diodes clamped to the supply rails is used to protect the inputs from static discharge. The resistor and the 56 pF capacitor form low-pass stability filter.

During testing of the initial device a problem was discovered. Due to the very high input impedance of the AD627, when an electrode inadvertently falls the amplifier saturates in all channels through the DLR schematic. To solve this problem and to assure redundancy of the system TLC 2252 micro-power opamps were added before the instrumentation amplifier as a simple voltage follower.

2.2. Driven Right Leg (DRL)

The biggest noise origin in the EMG bandwidth is the electrical network interference. It produces a

common mode voltage in the patient body and sometimes this voltage is higher than the useful signal. The DRL system is based on a feedback circuit that drives the common-mode voltage back to the patient body, amplified and phase reversed by 180°. This feedback improves the CMRR by an amount equal to $(1+A)$ where A is the closed loop gain of the feedback loop.

In this design the common voltage is collected by from the two resistors of the R_g group. Then through a voltage follower, which purpose is to protect the gain circuitry, it goes through an inverting amplifier which reverses it to 180°. And then it goes back to the patient. A current limiting resistor is added to protect the patient. A typical DRL implementation is shown on fig. 4 [5].

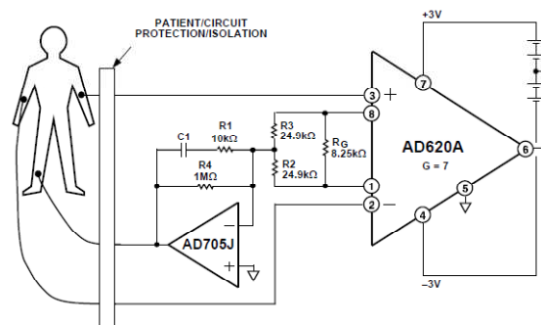


Fig. 4

2.3. Filters

After the preamplifier the next stage is the groups of high-pass and low pass filters.

The frequency range of the amplifier is chosen to be 25Hz – 500Hz. This range is chosen to eliminate the low frequency noise which is mostly below 25Hz. The upper cut off frequency is chosen so that the signal will include the most of the EMG signal and to ease the signal processing.

Simple RC filters are chosen for this stage. First it is the high-pass filter and then the low pass.

$$F_c = \frac{1}{2\pi RC}$$

For High Pass We have:

$$C = 0.22 \mu\text{F} \text{ and } R = 33 \text{ k}\Omega \quad F_c = 22 \text{ Hz}$$

For Low pass we have:

$$C = 0.056 \mu\text{F} \text{ and } R = 5.6 \text{ k}\Omega \quad F_c = 507 \text{ Hz}$$

2.4. Second Stage Amplifier

The second stage amplifier is a non-inverting amplifier with a gain of 50.

In this stage we translate the signal to single-supply with a zero-point at 1.65V.

MCP609 is used for the design. It is a micro-power rail to rail op-amp, designed for single-supply purposes. Additional filtering is added at the gain setting network and at the output of the amplifier.

2.5. ADC

A dedicated multichannel ADC - ADS7844 schematic is used. It is a micro-power 8-channel ADC with SPI communication. The maximum sampling rate is 200 kHz.

Most of the present day microcontrollers have ADC integrated into them by using them instead of a dedicated ADC presents several problems. First it is the power supply decoupling. To improve the noise suppression usually the power lines in the analog schematic is decoupled through a LC network to suppress the noise from the digital schematics. Using the MCU ADC will add noise to the analog schematic.

Another problem is design commonality. If we change the microcontroller we need to redesign also the analog part of the schematic to use the new MCU ADC.

Since the upper frequency of the amplifier is set to 500 Hz and according to the Nyquist-Shannon theorem, the minimum sampling rate per channel is 1000Hz. To further improve the digitalization a sampling rate of 2000Hz is chosen.

The amplitude range of the signal is from 0 V to 3.3 V.

The general parameters of the amplifier are:

Frequency response: 25 Hz – 500 Hz

Total Gain: 500

Dynamic range: ± 3.3 mV

3. DIGITAL PART

The digital part of the device consists of: MCU, LCD for displaying critical data, the Bluetooth transceiver and a SD card holder for logging data.

3.1. Microcontroller

There is a wide variety of options for the Microcontroller. The chosen MCU for this project is the Mi-

crochip PIC24FJ128A306 [4]. It is a 16-bit MCU with 128 kB of Program memory, 8 KB of RAM, NanoWatt Technology for extreme low power consumption and up to 32 MHz of operation speed.

The main reason to choose this MCU for the project are:

- The very low power consumption;
- High speed;
- Low profile;
- The availability of the Peripheral Pin Select function;
- The available Development tools MPLAB and MICROCHIP C16 C-compiler.

3.2. Bluetooth transceiver

Bluetooth was chosen for the design. It will give freedom of movements for the device and has enough range.

There are many manufacturers of Bluetooth transceivers, which function as a simple serial port over Bluetooth. There is no need to develop specialized applications and drivers for communications, because it is transparent to the MCU and the host computer. Based on popularity and known quality the SENA PARANI BCD-210 was chosen [6]. The module is first configured with the tool ParaniWin where the speed and authentication options are set.



Fig. 5. Parani BCD210DC

3.3. LCD Display

A low profile monochrome LCD display is chosen – DEM12864L from Display Elektronik GmbH. It features a Chip on Glass technology and 128x64 resolution. It has very low power consumption.

3.4. SD Card

A SD card slot is provided to collect a log data. The SD card is working in SPI mode.

3.5. Power supply

Power is provided by a single AAA battery which, because of the low power design is enough for at least 10 hours of operation.

A very efficient voltage convertor IC is used – MAX1676.

4. EXPERIMENTS

To test the device a Software EMGLab was developed.

The device is tested on different muscles with real-time signal processing.

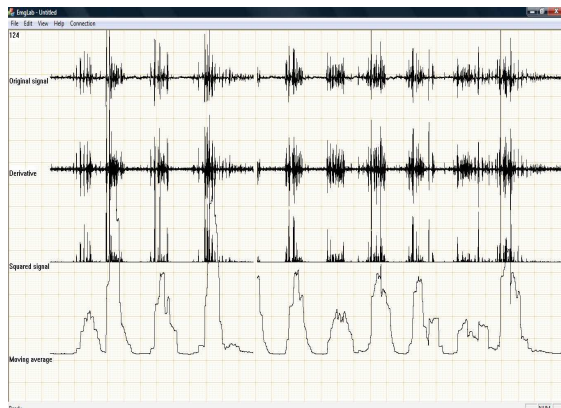


Fig. 6. Rectus femoris muscle

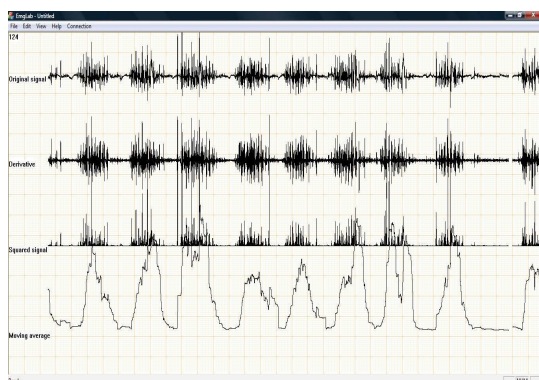


Fig. 7. Rectus femoris during walking

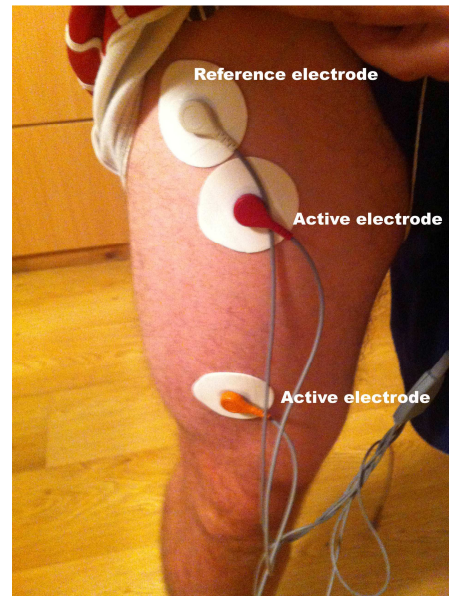


Fig. 8. Electrode placement for the Rectus femoris experiment

5. CONCLUSION

The device extracts very well the EMG signals from the muscles. The light weight and small size make it transparent the test patient, which gives us very accurate experimental results for the patients gait and movements.

This gives us an opportunity to develop models for recreation of missing muscles based on the data for other muscles.

References

- [1] Rangaraj M. Rangayyan "Biomedical Signal Analysis" Wiley-Interscience
- [2] Joseph Bronzino "The Biomedical Engineering Handbook" CRC Press
- [3] Webster J, "Medical Instrumentation – application and design" John Wiley & Son
- [4] MICROCHIP PIC24FJ128GA306 Datasheet <http://www.microchip.com/wwwproducts/Devices.aspx?product=PIC24FJ128GA306>
- [5] Analog Devices AD620 Datasheet <http://www.analog.com/en/products/amplifiers/instrumentation-amplifiers/ad620.html>
- [6] Sena Industrial Parani BCD210 Datasheet http://www.senaindustrial.com/products/industrial_bluetooth/bcd210.php

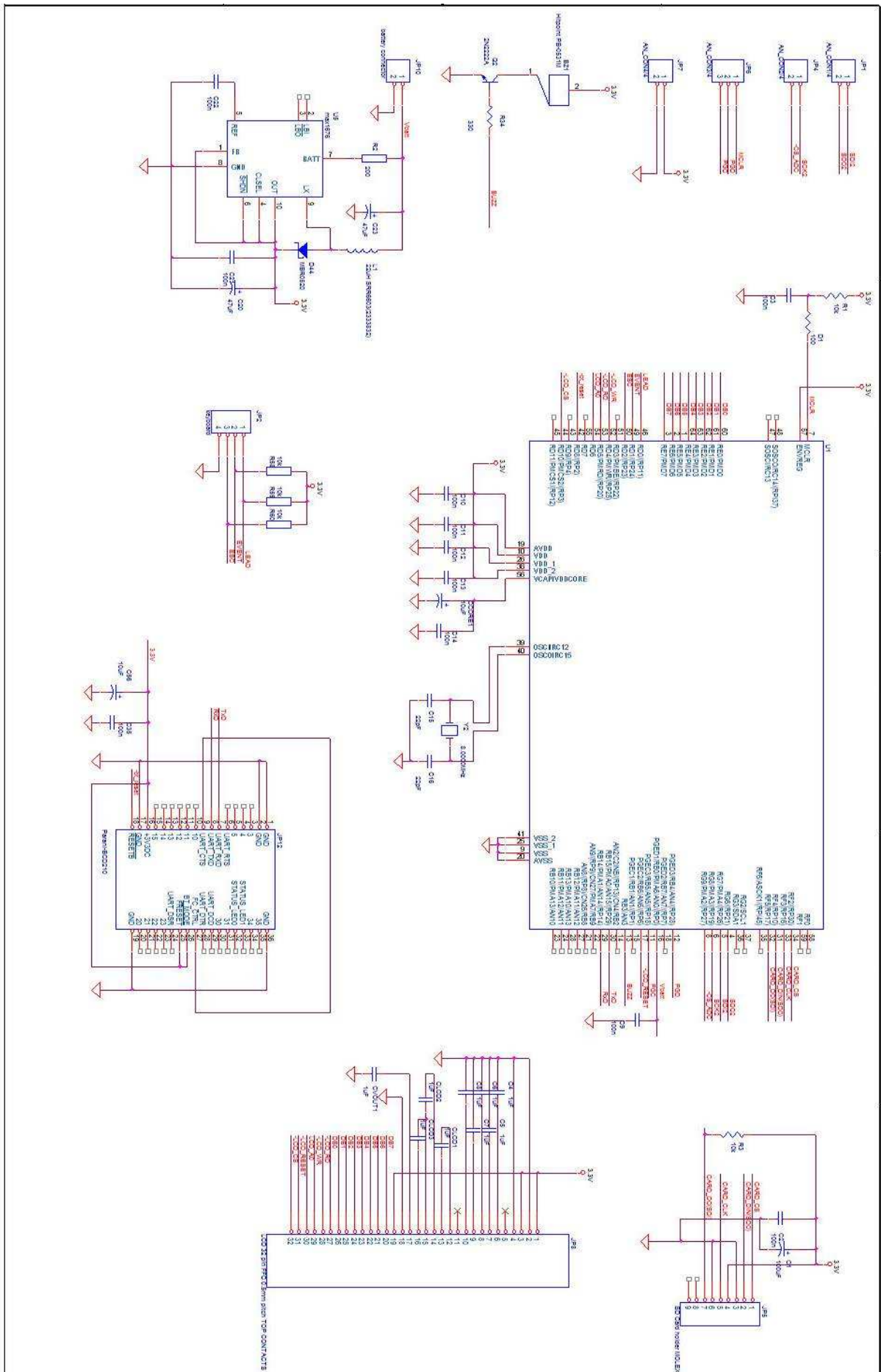


Fig. 9. Digital part of the device

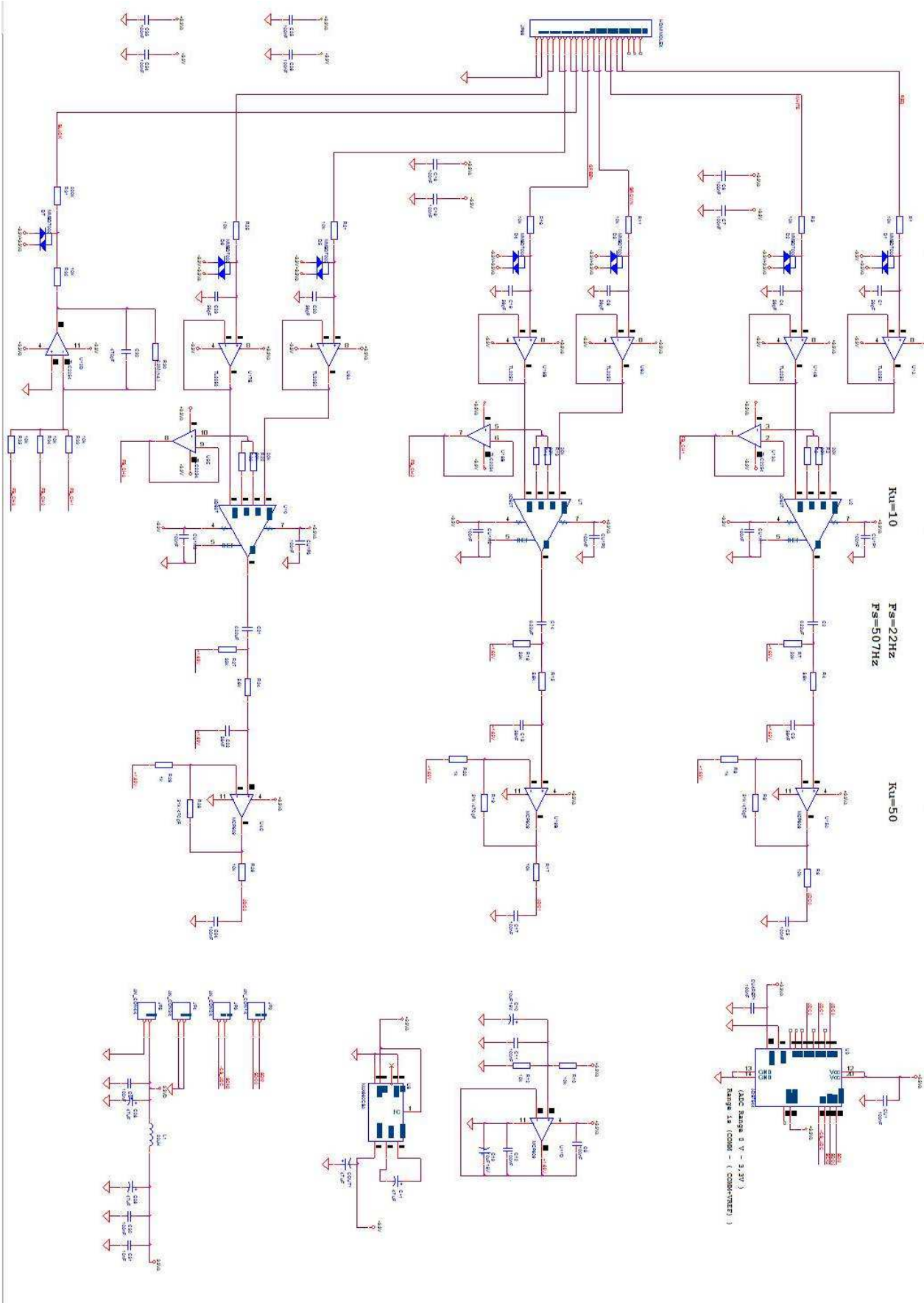


Fig. 10. Analog part of the device

SOFTWARE FOR ANALYZING EMG SIGNALS EMGLab

Viktor A. Nedialkov

Department of Radio Communications and Video Technologies, Faculty of Telecommunications,
Technical University of Sofia, 8 Kl. Ohridski Blvd, Sofia 1000, Bulgaria

Abstract

A software for analyzing EMG signals in real-time has been developed. The purpose of the software is to analyze the behavior of the human gait and help develop new algorithms for incorporation in active prosthetics.

The software is intended to work with the portable EMG multichannel recorder developed previously.

1. INTRODUCTION

In the process of development of an active EMG prosthesis a multichannel EMG processing device has been built. The device is intended to collect EMG signals from several muscles, amplify, digitize and send the data to PC via Bluetooth or USB link.

Below a general block scheme of the design is shown.

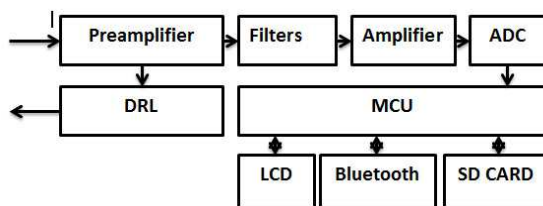


Fig. 1. (Block scheme of the device)

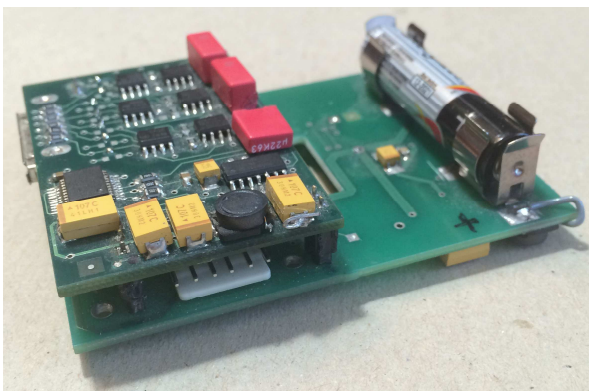


Fig. 2. The device prototype

A digital signal with F_s (discretization frequency) of 2000Hz per channel is produced by the device.

The raw EMG signal must be transformed to a signal more suitable for analysis of the behaviour of the muscles. An algorithm has been developed

to detect muscle contraction with a possibility to assess the level of contraction in real-time [1].

The algorithm is based on the Pan-Tompkins QRS detection algorithm. It has four stages in signal processing. Bandpass filtering to remove unwanted noise. Differentiation stage to emphasize the high frequency signal. Integration stage to make the result positive and further emphasize the large differences. The moving average smooth the multiple peaks from the squaring operation.

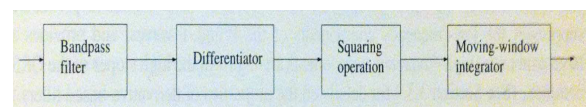


Fig. 3

For the development of the software Microsoft Visual Studio 2010 is used with development language Visual C++. The reason for that is we have already written similar code which will reduce the time for development.

The software has the following main stages

- Communication
- Signal processing
- Visualization

2. COMMUNICATION

Communication is achieved via virtual serial port. The data from the device is send after every discretisation period, which is set at 2000 Hz. The communication speed is 115200bps. Data is sent packed in the following protocol AAh, MSB1, LSB1, MSB2, LSB2.

Where AAh is a sync byte to select the start of a packet. The signal data is 12-bit long packed in two bytes.

The communication port is opened with the function

```
m_hCommPort=CreateFile(com_port,GENERIC_READ | GENERIC_WRITE,0,0,OPEN_EXISTING,0,0);
```

which creates a handle to the port. Then we set the setting of the port when we first get the current settings, edit the variables we want and write the edited setting back:

```
::GetCommState(m_hCommPort,&dcb)
dcb.BaudRate=CBR_115200;
dcb.ByteSize=8;
dcb.Parity=0;
dcb.StopBits=ONESTOPBIT;
::SetCommState(m_hCommPort,&dcb)
```

The method chosen for receiving data is data pooling the communication port at a set period. For that we start a timer with a period 2ms with the following:

```
SetTimer(1,2,NULL);
```

Every 2 ms an event is triggered and event handler is called. The event handler calls the communication function. The communication function pools the serial port for available data and transfer the available data to the temporary buffer.

```
do
{
If(!::ReadFile(m_hCommPort,chBuffer,sizeof(chBuffer),&bytesRead,0))
{
    ErrorCode=GetLastError();
}
for (int i=0;i<bytesRead;i++)
{
    mBuffer.push_back(chBuffer[i]);
    m_buf_lenght++;
}
while (bytesRead>0);
```

After that the function is searching for the sync byte and deletes all data until it finds it. If the first byte in the buffer is a sync byte the function sets a variable that there is available data.

```
double received_data =
(double)(256*mBuffer[1] + mBuffer[2]);

double received_data2=
(double)(256*mBuffer[3] + mBuffer[4]);

packet[0]= received_data;

packet2[0]= received_data2;
```

Communication is terminated with the functions

```
KillTimer(1);
CloseHandle(m_hCommPort);
```

Which closes the timer event and also closes the handle of the virtual COM port.

After a data byte is ready, it is processed by the signal processing stage of the program.

3. SIGNAL PROCESSING

The signal processing stage is divided by the following sub-stages

- Derivative function
- Squaring function
- Moving Average function
- Screen coordinated calculation

The derivative operator is calculated by the following lines:

```
double CEmgLabView::Derivative(double *
packet)
{
double derivative=0;
mDerBuffer.push_back(packet[0]-2048);
mDerBufferCounter++;
if (mDerBufferCounter>5)
{
derivative=(double)(2*mDerBuffer[5]+mDerBuffer[4]-mDerBuffer[2]-2*mDerBuffer[1]);
derivative=derivative*0.125;
mDerBuffer.erase(mDerBuffer.begin());
mDerBufferCounter--;
return derivative+2048;
}
else
{
return derivative;
}
}
```

The last received data is passed to the function, corrected for polarity and pushed into buffer, from which the derivative is calculated.

The squaring is a simple square operation of the derivative result.

The result is then passed to the moving average calculation function

```
double CEmgLabView::MovingAverage(double *
packet)
{
double ma_result=0;
int MA_SIZE=500;
mMABuffer.push_back(packet[2]);
mMABufferCounter++;
if (mMABufferCounter>=MA_SIZE)
{
for (int i=0;i<MA_SIZE;i++)
{
ma_result=ma_result+mMABuffer[i]/MA_SIZE;
}
mMABuffer.erase(mMABuffer.begin());
mMABufferCounter--;
return ma_result;
}
else
{
return ma_result;
}
}
```

The calculated result from the squaring operation is inserted into a buffer, then a Moving Average with depth of MA_SIZE is calculated with the For operation.

The next step is to calculate the screen value of the calculated data

```
Int lead0=Round(mVertOffset+0*mVertRes/6
+mVertRes/12-packet[0]/mAmplitude
+2048/mAmplitude);
```

The Y- screen coordinates are calculated based on the screen resolution, offset and selected Amplitude scale.

4. VISUALIZATION

The discretisation frequency is 2000Hz and the serial port data pooling is set at 2ms. The calculation stage is performed for every data element of the signal. The screen calculation is also made for every data element but it is not possible to draw directly to the screen with 2000Hz draw frequency. That is why the process of visualization is divided into two stages – Draw to memory and copying of the memory buffer to the screen at a reasonable frequency.

We first create the memory screen buffers

```
m_pMemDC->CreateCompatibleDC(pDC);
m_pBitmap->CreateCompatibleBitmap
(pDC,ClientRect.right,ClientRect.bottom);
```

Another buffer is also used for the raster of the screen.

A timer is started with a period of 20 ms.

Every time an event is triggered the event handling function executes a copy of the memory buffer to the screen.

```
m_pMemDC->BitBlt(ClientRect.left,
ClientRect.top,ClientRect.right,ClientRect
.bottom,m_pMemDCRaster,0,0,SRCCAND);
pDC->BitBlt(ClientRect.left,
ClientRect.top,ClientRect.right,ClientRect
.bottom,m_pMemDC,0,0,SRCCOPY);
```

The first line copies the screen raster to the memory buffer and the second line copies the memory buffer to the screen.

5. EXPERIMENTS

The software was tested also to verify the accuracy of the muscle contraction detection algorithm. Below are screenshots during testing

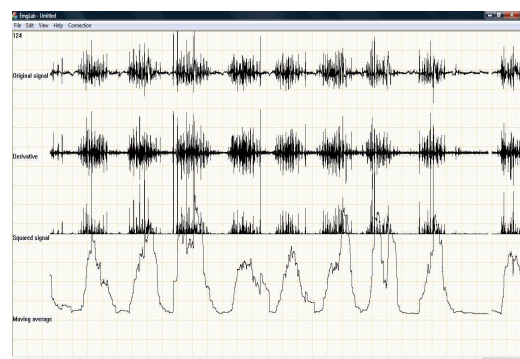


Fig. 4. Rectus femoris during walking

6. CONCLUSIONS

The software is working properly and is achieving its purpose to allow us to analyse and develop different algorithms for active prosthetics control. The real-time graphics is moving smoothly without glitches with the method of visualization chosen and the system is not loaded additionally by the program.

Further development of the software will include data storing and offline analysis of the stored signals.

Also an active prosthetics simulation module will be added.

References

- [1] Pan J. and Tompkins W. J. "A real-time QRS detection algorithm." IEEE Transaction on Biomedical Engineering, 32:230-236, 1985
- [2] Rangaraj M. Rangayyan, "Biomedical Signal Analysis" Wiley-Interscience
- [3] Joseph Bronzino, "The Biomedical Engineering Handbook" CRC Press
- [4] Webster J, "Medical Instrumentation – application and design" John Wiley & Son.

FUNDAMENTAL STUDY ON MEASUREMENT OF DIELECTRIC CONSTANTS OF HUMAN ABDOMEN BY WAVEGUIDE-PENETRATION METHOD

Takahiro Aoyagi

Department of Human System Science,
Graduate School of Decision Science and Technology,
Tokyo Institute of Technology, Japan
Postal address(es)
2-12-1, O-okayama, Meguro-ku, Tokyo, 152-8552, Japan

Abstract

Permittivity of human tissues have been measured in vitro in many literatures. However, to use permittivity of human tissue for diagnoses or healthcare purpose, it is desirable to measure in vivo. The author's research group has studied about measurement method for permittivity of human fingers in vivo by waveguide penetration method. To measure permittivity of human abdomen, larger waveguide is necessary. In this paper, applicability of the method to measure dielectric constant of human abdomen is investigated by numerical simulations. A large size waveguide is designed to measure permittivity of human abdomen. Transparent coefficients and reflection coefficients of the waveguide are measured at multiple frequencies with existence of human abdomen for different thickness of muscle and fat layers. The results show the possibility to measure and to evaluate fat in human abdomen by using this technique for healthcare purpose. For future study, detailed conditions of measurement are investigated and comparisons with experiments are performed.

1. INTRODUCTION

In aging society, workloads of medical doctors and workers are huge problem. To reduce their workloads, essentially, preventive medicine is important. Accordingly, lifestyle related disease, such as cardiac disease, hypertension, metabolic syndrome, obesity, or diabetes mellitus, should be overcome by healthcare and preventive medicine. To prevent metabolic syndrome, Japan ministry of health, labor and welfare has employed abdominal circumference measurements in periodic health examinations from 2008. The criteria of this examination are below 85 cm for male, and below 90 cm for female. However it is easily supposed that measuring only abdominal circumference is not very exactly reflect the amount of internal organs fat, which is a major cause of metabolic syndrome. To exactly measure internal organs fat, a CT scanning or an MRI, which is high cost for the patients, is necessary. Wherewith, inexpensive and non-invasive measurement methods to estimate biological information of internal organs have been proposed. Lung density and air volume has been measured by electrical impedance tomography (EIT) [1]. Practical human abdominal fat imaging has been utilized by also EIT [2]. However, measurement methods that use electric impedance require electrodes attached on skin, and state of

electrode contact greatly affect the measurement results. To overcome this, an electrode-less method is desired. Meanwhile, microwave technology enables us to measure dielectric constants of human tissues. As described in the literature [3], fat and muscle (or other human tissues) has very different value. Thus it is expected that amount of internal organs fat could be estimated by measuring dielectric constants of abdomen. The author has measured dielectric constant of human finger [4] by waveguide penetration method [5][6]. By extending this method to measure dielectric constant of human abdomen, it is expected that internal organs fat can be estimated for individual person. In this paper, basic considerations of waveguide penetration method to measure internal organs fat are described. This paper organized as follows. In the section 2, waveguide penetration method is briefly explained. In the section 3, application for the waveguide penetration method for abdomen is described, results of the simulations are presented, and possibility of this method is discussed. In the section 4, this paper is summarized.

2. DIELECTRIC CONSTANT MEASUREMENT BY WAVEGUIDE PENETRATION METHOD

Fig. 1 shows the basic geometry of the permittivity measurement by waveguide penetration method. The basic structure is a rectangular waveguide with two circular holes which cylinder shape specimen can be inserted. Two ports (port 1 and port 2) of a vector network analyzer (VNA) are connected to two sides of the waveguide by coaxial-waveguide transducers. By performing bi-directional two ports measurement by the VNA, scattering coefficients ($S_{11}, S_{12}, S_{21}, S_{22}$) of the rectangular waveguide inserted with specimen are obtained. Dielectric constant of the specimen is estimated by solving an inverse problem between the scattering coefficients and the dielectric constant of the specimen. In the literature [5], the problem is solved by the rigorous solution of the propagating wave in the rectangular waveguide with specimen. Dielectric constant of the specimen can also be estimated by calculating scattering coefficients by using numerical simulations and comparing the calculated scattering coefficients with measurements. The waveguide penetration method has been extended to measure dielectric constants of liquid or layered cylindrical materials [6]. Dielectric constants of Japanese sake [7] or human finger [4] have been measured by this method.

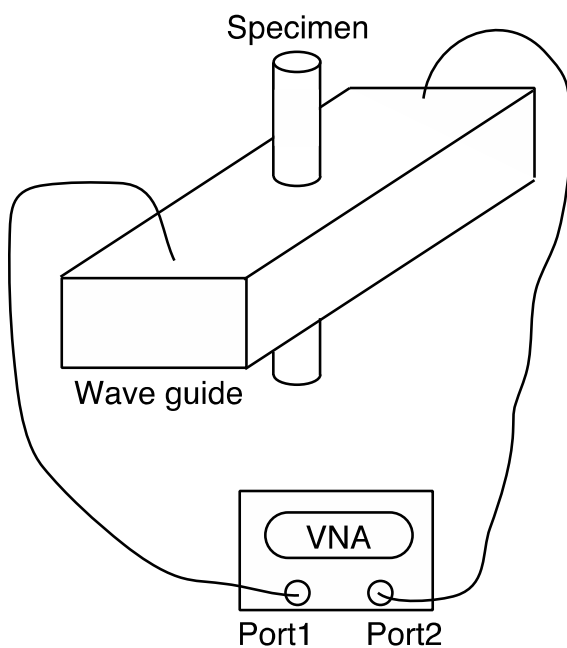


Figure 1. Basic geometry of waveguide penetration method

Fig. 2 shows the basic concept of a measurement of dielectric constant of human abdomen. The

large size rectangular waveguide is connected to a VNA. Human abdomen penetrates the waveguide. The electromagnetic wave propagating in the waveguide is scattered and absorbed by human abdomen, thus the scattering coefficients measured by VNA reflects the shape and the dielectric constant of the abdomen and internal organs. The amount of internal organs fat might be estimated by measured dielectric constants. In this paper, as a preliminary consideration, numerical simulations of this measurement for several conditions are performed.

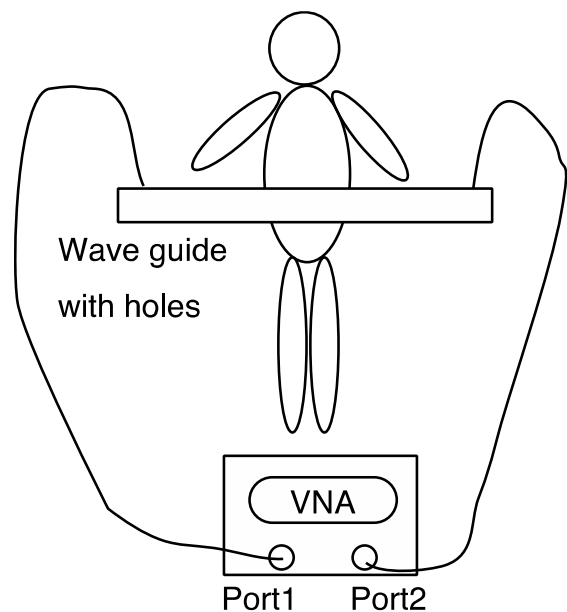


Figure 2. Basic concept of the measurement method of dielectric constant of human abdomen

3. NUMERICAL SIMULATIONS FOR MEASUREMENT OF DIELECTRIC CONSTANTS OF HUMAN ABDOMEN BY WAVEGUIDE PENETRATION METHOD

Fig. 3 shows the geometry of numerical simulations of measurement of dielectric constants of human abdomen by waveguide penetration method. In this paper, a commercial FEM (finite element method) software COMSOL Multiphysics is used for numerical simulations. Basically, the geometry is same as depicted in the Fig. 1, but the coaxial-waveguide transducers are replaced to rectangular wave ports for convenience in calculations. The abdomen is cut off to reduce calculation load, and the two holes are terminated by two hemispherical shaped absorbing boundaries. The size of the rectangular waveguide is 0.5 m \times 0.05 m \times 1 m, the radius of the circle holes is 0.15 m. The measurement frequency range is between 450 MHz and

550 MHz. The S_{21} of the rectangular waveguide without human body is -3 dB at 500 MHz due to outgoing waves from the holes. To emulate simplified human abdomen structure, two layers cylinder is used as specimens in simulations. Dielectric constants of inner and outer layer of cylinder are set as those of muscle and fat at 500 MHz, respectively.

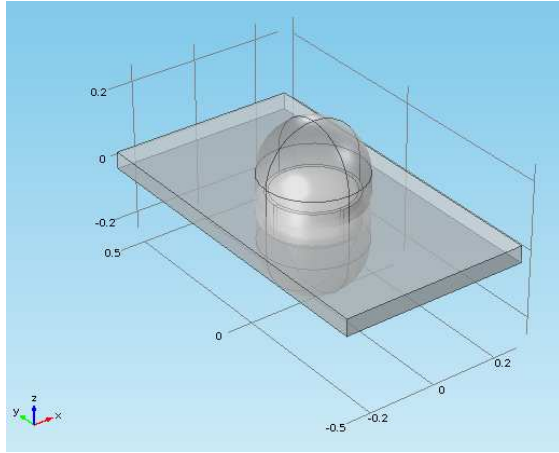


Figure 3. Geometry of numerical simulations of measurement of dielectric constants of human abdomen by waveguide penetration method

Table I shows the dielectric constants of human tissues [8] used in the simulations. As shown in the table, relative permittivity of muscle is above ten times greater than that of fat, and conductivity of muscle is twenty times smaller than that of fat. Thus the measured scattering coefficients are largely affected by amount of muscle and fat and their shape.

Table I. Electric constants of human tissues at 500 MHz

Tissue	Relative Permittivity	Conductivity (S/m)
Muscle	77.063	0.67808
Fat	6.8758	0.034677

Fig. 4 shows the calculated distributions of electric field by a numerical simulation at 550 MHz. The circumference of abdomen is 80 cm, and the circumference of inner muscle is 70 cm. It is clearly shown that the excited electromagnetic field is attenuated by human abdomen and received at the port on the other side.

To investigate differences of scattering coefficients by amount of fat and muscle, calculations are performed for different size of abdomen and internal

muscle. Table II summarizes the simulation conditions. The condition A is assumed as a standard condition. The condition B is assumed as an abdomen that has much fat. The condition C is assumed as an abdomen that has same circumference of abdomen as the condition B but has less fat.

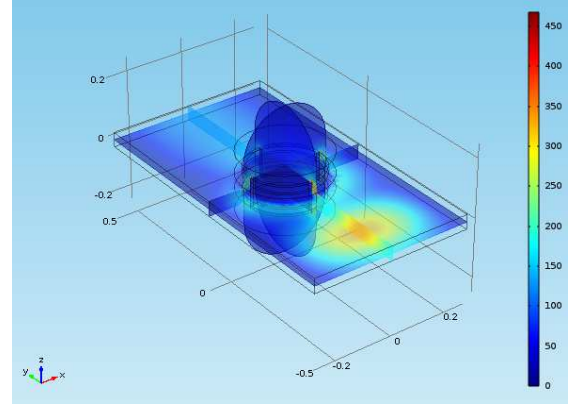


Figure 4. Calculation result of electric fields distribution (550 MHz)

Table II. Simulation conditions

Condition	Muscle		Fat	
	Circum. [cm]	Radius [cm]	Circum. [cm]	Radius [cm]
A	70	23.33	85	28.33
B	70	23.33	90	30.00
C	80	25.48	90	30.00

Fig. 5 and Fig. 6 show the calculated scattering coefficients of human abdomen for different conditions. Fig. 5 shows S_{11} , and Fig. 6 shows S_{21} , respectively. As shown in the figures, very different scattering coefficients are obtained depending on the size and amount of muscle and fat. These results suggest the possibility to measure amount of fat of human abdomen by the proposed method.

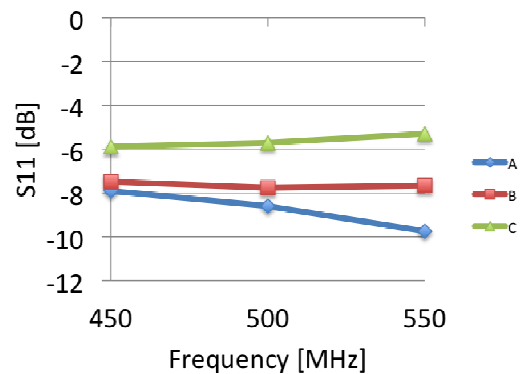


Figure 5. Scattering coefficients (S_{11}) of human abdomen for each condition

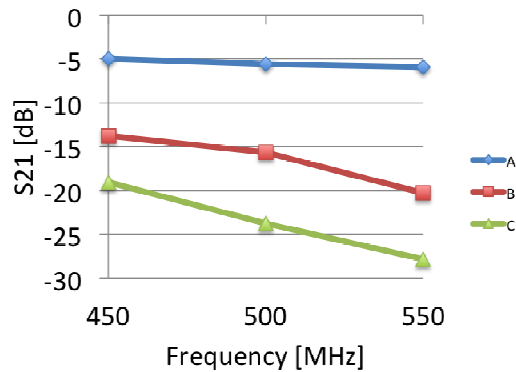


Figure 6. Scattering coefficients (S_{21}) of human abdomen for each condition

4. CONCLUSION

In this paper, a measurement method of human internal organs fat for health care diagnose by microwave waveguide penetration method is proposed. The basic concept and the geometry of the measurement method are explained. By performing the numerical simulations, possibility of the method is exhibited. There are many future works to realize this method for practical use.

- Optimize the frequency and the size of the rectangular waveguide and holes.
- Consideration of analytic calculation of scattering coefficients to reduce calculation load.
- Consideration of higher mode and varied direction measurements to increase accuracy of measurements.
- Perform experimental measurements and compare with numerical simulations.

References

- [1] T. Yamaguchi, K. Maki, and M. Katashima, "Practical human abdominal fat imaging utilizing electrical impedance tomography", *Physiol. Meas.*, vol.31, no. 7, pp.963–78, Jul. 2010.
- [2] S. Nebuya, G. H. Mills, P. Miles and B. H. Brown, "Indirect measurement of lung density and air volume from electrical impedance tomography (EIT) data", *Physiol. Meas.*, Vol. 32, pp. 1953–1967, 2011.
- [3] S. Gabriel, R. W. Lau, and C. Gabriel, "The dielectric properties of biological tissues: III. Parametric models for the dielectric spectrum of tissues", *Phys. Med. Biol.*, vol. 41, pp. 2271–2293, 1996.
- [4] Tomoki Hamaji, Alfred Kik, Takahiro Aoyagi, Atsuhiko Nishikata, and Soichi Watanabe, "In-vivo Measurement of Equivalent Complex Permittivity of Fingers Using the Waveguide-Penetration Method", *IEICE transactions B*, Vol. EJ94-B, No. 11, pp. 1503–1507, 2011 (in Japanese).
- [5] Atsuhiko Nishikata, "A swept-frequency measurement of complex permittivity and complex permeability of a columnar specimen inserted in a rectangular waveguide", *IEEE trans.onmicrowave theory and techniques*, Vol. 55, No. 7, pp. 1554–1567, Jul. 2007.
- [6] Atsuhiko Nishikata, "Scattering analysis for layered cylindrical object perpendicularly piercing the wider walls of a rectangular waveguide and its application to ϵ_r and μ_r measurement", *IEEE trans.onmicrowave theory and techniques*, Vol. 57, No. 6, pp. 1602–1611, Jun. 2009.
- [7] Masaki Kouzai, Atsuhiko Nishikata, Kaori Fukunaga, and Shunsuke Miyaoka, "Complex permittivity measurement at millimetre-wave frequencies during the fermentation process of Japanese sake", *Journal of Physics D: Applied Physics*. Vol. 40. No. 1. pp. 54–60. 2006.
- [8] D. Andreuccetti, R. Fossi and C. Petrucci, "An Internet resource for the calculation of the dielectric properties of body tissues in the frequency range 10 Hz - 100 GHz", Website at <http://niremf.ifac.cnr.it/tissprop/>, IFAC-CNR, Florence (Italy), 1997. Based on data published by C. Gabriel et al. in 1996.

Acknowledgement: This work was supported by JSPS KAKENHI Grant Number 15K06054.

LOWER LIMB EMG SIGNALS STUDY FROM DIFFERENT MUSCLES FOR POTENTIAL MYOELECTRIC PROSTHESES CONTROL

Viktor A. Nedialkov

Department of Radio Communications and Video Technologies, Faculty of Telecommunications,
Technical University of Sofia, 8 Kl. Ohridski Blvd, Sofia 1000, Bulgaria

Abstract

A Using previously designed portable EMG acquisition device and a specialized software EmgLab, a complete study of the EMG signals from different lower-limb muscles is made. The goal is to choose the most suitable signals for controlling myoelectric prostheses. During the study different motions are exercised: level walking, going up and downstairs.

1. INTRODUCTION

In individuals who have lost limbs, in order to recreate the movement of the limb with an active prosthesis, an estimation must be made based on other muscles used for particular movement. A detailed study must be performed to record the muscles activity in healthy individuals.

First we need to understand the biomechanics of human walking, as this information plays a crucial role in the design of such systems. A simplified diagram of human walking gait is shown on Fig.1 [1]

Note that the timing of the labelled events during the gait cycle is approximate, and varies across individuals and conditions. The human walking gait cycle is typically represented as starting (0%) and ending (100%) at the point of heel strike on the same foot, with heel strike on the adjacent foot occurring at approximately 62 % of gait cycle.

In general, the human leg can be thought of as a seven degrees of freedom structure, with three rotational degrees of freedom at the hip, one at the knee and three at the ankle. A description of the human anatomical planes as well as a kinematic model of the human leg in the sagittal plane, which is the dominant plane of motion during human locomotion.

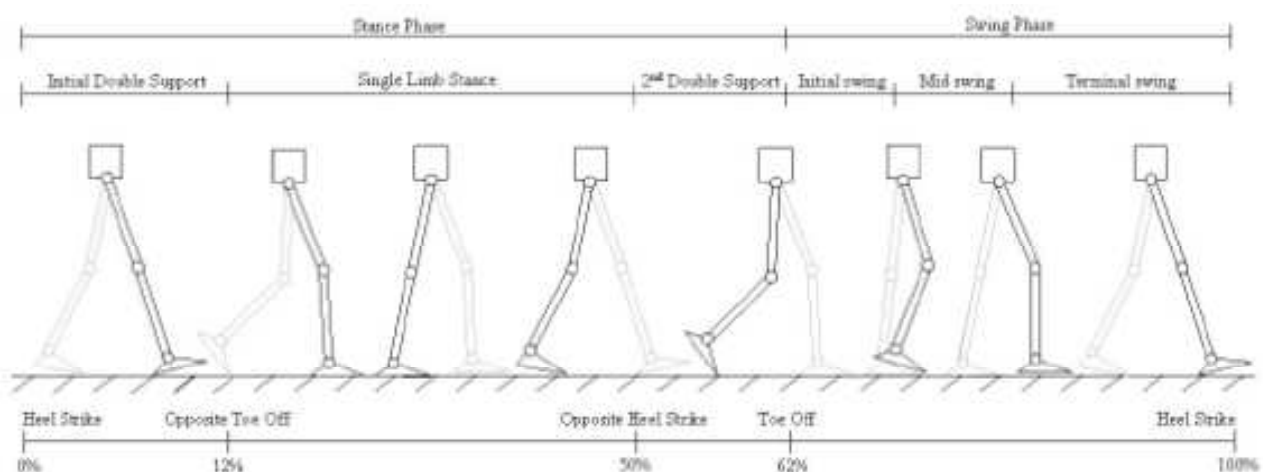


Fig. 1 Human Walking gait through one cycle

The positive motion in the sagittal plane is called flexion and the negative motion is called extension.

This is the plane and the motions an active EMG driven prosthesis will use.

Figure 3 show the biomechanics of a normal, healthy individual, showing joint angle for hip, knee and ankle flexion/extension motions during level-ground walking [2]. While walking data can differ

some what across subject and condition, the qualitative nature of the curves remains similar [3].

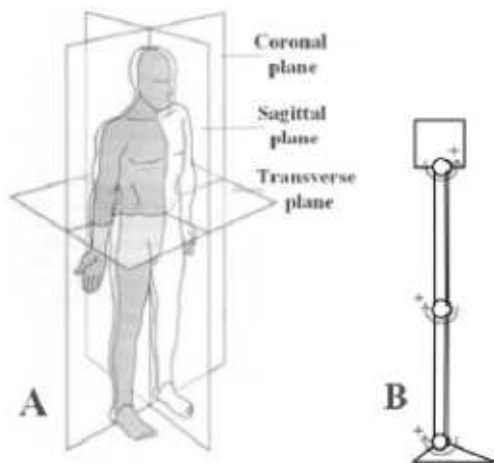


Fig. 2

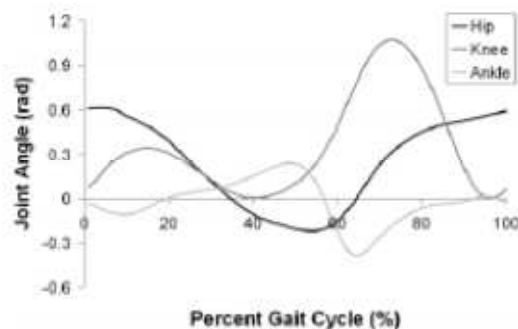


Fig. 3

To perform the study an specially designed EMG recorder was developed. It collects EMG data from surface electrodes at frequency of 2000Hz. Data is send via Bluetooth to a PC where it is processed by a specially developed software EmgLab.

In this software an algorithm is used to detect muscle contraction with a possibility to assess the level of contraction in real-time [4].

The algorithm is based on the Pan-Tompkins QRS detection algorithm. It has four stages in signal processing. Bandpass filtering to remove unwanted noise. Differentiation stage to emphasize the high frequency signal. Integration stage to make the result positive and further emphasize the large differences. The moving average smooth the multiple peaks from the squaring operation.

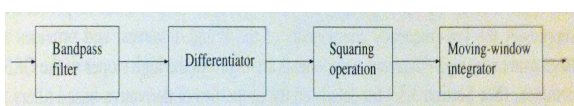


Fig. 4

There are many muscles involved in the gait cycle. We will turn our attention to the muscles of the upper leg and specifically the Quadriceps and the Hamstrings.

The quadriceps femoris (quads) is a large muscle group that includes the four muscles on the front of the thigh. It is the great extensor muscle of the knee, forming a large fleshy mass covering the front and sides of the femur. It is subdivided into four separate portions (heads), each with distinctive names. Rectus femoris occupies the middle of the thigh, covering most of the other three quadricep muscles. It originates on the ilium and is named from its straight course. The remaining three lie deep to rectus femoris, and originate from the body of the femur, which they cover from the trochanters to the condyles.

These muscles are powerful extensors of the knee joint. They are crucial in walking, running, jumping, and squatting. Because rectus femoris attaches to the ilium, it is also a flexor of the hip. This action is also crucial to walking or running, as it swings the leg forward into the ensuing step. The quadriceps (specifically the vastus medialis) plays the important role of stabilizing the patella and the knee joint during gait.

The hamstring refers to any one of the three posterior thigh muscles (semitendinosus, semimembranosus and biceps femoris) that make up the borders of the space behind the knee; or can refer to their corresponding tendons. The hamstring muscles flex (bend) the knee, while all but the short head of biceps femoris extend (straighten) the hip. The three 'true' hamstrings cross both the hip and the knee joint and are, therefore, involved in knee flexion and hip extension. The short head of the biceps femoris crosses only one joint (knee) and thus is not involved in hip extension. With its divergent origin and innervation it is sometimes excluded from the 'hamstring' characterization. The hamstrings play a crucial role in many daily activities such as walking, running, jumping and controlling particular movement in the trunk. In walking, they are most important as an antagonist to the quadriceps in the deceleration of knee extension [6].

2. EXPERIMENTS

First we examine the EMG signals during normal walking. We put the electrodes of the first channel

on the rectus femoris and the second channel on the biceps femoris (Fig. 5).

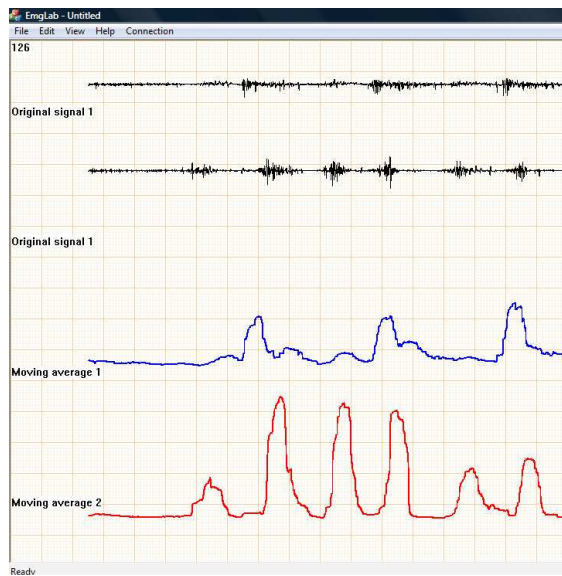


Fig. 5

In the moving average results of the signal we see that first we have a contraction of the biceps femoris then a contraction of the rectus femoris, followed by another contraction of the biceps femoris. The first contraction of the biceps femoris is the lifting of the lower leg of the ground, then the rectus femoris swing the leg forward and then the biceps femoris again takes the load of the bodyweight.

The second experiment is a step climb. Again the electrodes are above rectus femoris and biceps femoris (Fig. 6).

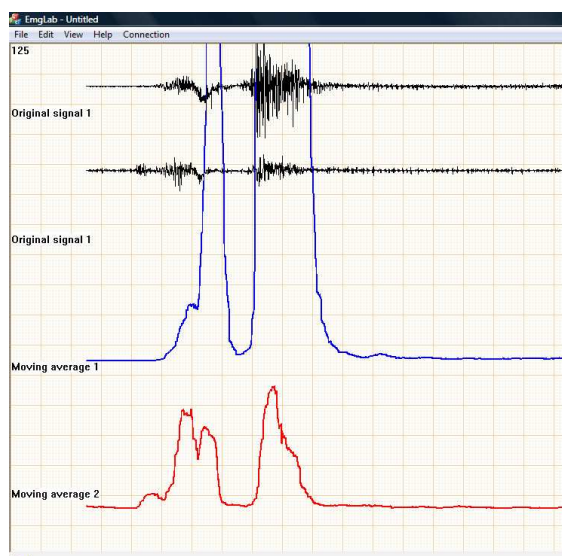


Fig. 6

Here we have a double amplitude peak signal in both muscles which are synchronous. The first impuls is shorter and is associated with the lifting of the leg and planting it on the step, while the second one is the lifting of the body by the leg.

The third experiment is the stepping down motion. Electrodes are again on the rectus femoris and biceps femoris (Fig. 7).

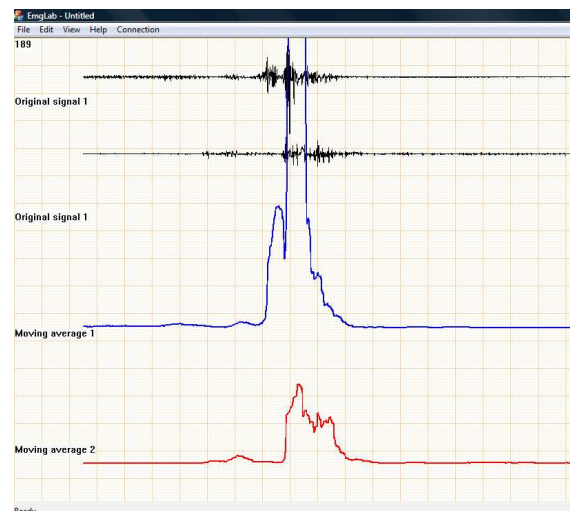


Fig. 7

We have again synchronous signals from both muscles but the signal from rectus femoris is much bigger and is two-phase. The first phase corresponds to the lifting of the leg while the second much bigger phase begins with the planting of the leg on the ground and the beginning of taking the load on it.

3. CONCLUSIONS

We were able to obtain signals from the most common movements – walking, climbing and stepping down. With the Software Emg Lab we were able to record the behaviour of the muscles during this exercises.

From the results obtained we can clearly distinguish all types of movements from just two muscles – rectus femoris and biceps femoris. This can allow us to control the knee joint with a certain degree of accuracy.

Further development may include adding more channels to monitor other channels.

Also a study need to be performed to find a relationship between the movement of the above the knee muscles and the ankle joint.

References

- [1] J. Rose and J. G. Gamble, Human Walking, Williams and Wilkins, Baltimore, MD, USA, 2nd ed., 1994.
- [2] M. Popovic, A. Goswami, and H. Herr, "Ground Reference Points in Legged Locomotion: Definitions, Biological Trajectories and Control Implications," *International Journal of Robotics Research*, vol. 24(12), pp. 1013-1032, 2005.
- [3] A. Winter, Gait Data, International Society of Biomechanics, Biomechanical Data Resources, <http://guardian.curtin.edu.au/org/data>
- [4] Pan J and Tompkins W. J. "A real-time QRS detection algorithm." *IEEE Transaction on Biomedical Engineering*, 32:230-236, 1985.
- [5] Rangaraj, M. Rangayyan "Biomedical Signal Analysis" Wiley-Interscience Boundless. "Muscles that Cause Movement at the Knee Joint." *Boundless Anatomy and Physiology*. Boundless, 21 Jul. 2015
<https://www.boundless.com/physiology/textbooks/boundless-anatomy-and-physiology-textbook/the-muscular-system-10/muscles-of-the-lower-limb-107/muscles-that-cause-movement-at-the-knee-joint-579-9335/>